A Hybrid Numerical Simulation Approach for Turbulent Flows over Building-Like Obstacles

by

Kun-Jung Hsieh

A thesis
presented to the University of Waterloo
in fulfillment of the
thesis requirement for the degree of
Doctor of Philosophy
in
Mechanical Engineering

Waterloo, Ontario, Canada, 2008

I hereby declare that I am the sole author of this thesis. This is a true copy of the thesis, including any required final revisions, as accepted by my examiners.

I understand that my thesis may be made electronically available to the public.

Abstract

Computational fluid dynamics (CFD) has been widely applied to simulate turbulent flows in an urban environment. The two basic methodologies in CFD that have been applied here are a Reynolds-averaged Navier-Stokes (RANS) modeling and a large-eddy simulation (LES). The nature of the flow in a built-up urban area consisting of an arbitrary aggregation of buildings is dominated by unsteady large-scale turbulent structures. Recognizing that RANS is unable to correctly capture these turbulent structures while LES is associated with high computational costs, a hybrid RANS/LES methodology that combines the computational efficiency of RANS with the predictive accuracy of LES can be a promising simulation approach for the application to urban flows.

In the non-zonal approach of hybrid RANS/LES methodology, a single generalized turbulence model is used in the entire computational domain. This model can function as a RANS turbulence closure model or as a LES subgrid scale model, depending on the local grid resolution or flow properties. A variant of non-zonal approaches, referred as partially resolved numerical simulation (PRNS) in this study, obtains the generalized turbulence model from the rescaling of a conventional RANS model through the incorporation of a resolution control function (F_R). The resolution control function F_R is used to characterize the degree of modeling required to represent the unresolved scales of motion.

A new generalized functional form for F_R in PRNS is proposed in this thesis. The predictive performance of PRNS is compared with unsteady RANS (URANS) and LES computations, for a plane channel flow, and for fully-developed and developing flows over a matrix of cubes resembling a group of buildings. It is demonstrated that PRNS behaves similarly to LES, in terms of the predictions of the mean flow and turbulence, but outperforms URANS in general. This indicates PRNS is a promising approach for the simulation of complex turbulent flows in an urban environment.

Acknowledgements

I would like to express my gratitude to my co-supervisors, Drs. Fue-Sang Lien and Eugene Yee, for their invaluable advice and guidance.

I would like to recognize the financial support of this research by Chemical Biological Radiological Nuclear Research and Technology Initiative (CRTI) program under project number CRTI-02-0093RD and the Ontario Graduate Scholarship.

Many thanks to my family for their love and support.

Table of Contents

List of Figures

Nomenclature

Roman Letters

$C_{\varepsilon 1}$, $C_{\varepsilon 2}$	closure coefficients in the ε-equation
C_κ	closure coefficient in the formula of F_R
C_μ	closure coefficient in the formula of ν_t
C_s	closure coefficient for the Smagorinsky model
$E(\kappa)$	energy spectrum
F_R	resolution control function
H	cube height
k	turbulence kinetic energy
l_c	cutoff length scale
l_i	integral length scale
l_K	Kolmogorov length scale
p	pressure
Pi	geometric pitch
P_k	turbulence production term in the k-equation
$R(\Delta t)$	autocorrelation function evaluated for time lag Δt
Re	Reynolds number
S_{ij}	strain-rate tensor
S_ϕ	source term of ϕ
t	time
T	averaging time interval
T_L	integral time scale
u, v, w	velocity components in the x-, y-, and z-directions, respectively

u_i'	turbulent velocity fluctuation in the *i*-th direction
u_τ	friction velocity
$\overline{u_i'u_j'}$	Reynolds stresses
U_b	bulk velocity
U_r	reference velocity
x, y, z	Cartesian coordinates

Greek Symbols

β	pressure gradient across one geometric unit cell
δ	channel half height
δ_{ij}	Kronecker's delta
$\overline{\Delta}$	spatial filter width or grid spacing
Δt	time step
Δ_T	temporal filter width
$\Delta x, \Delta y, \Delta z$	grid spacing in the three coordinate directions at a local grid cell
ε	dissipation rate of k
Γ_ϕ	diffusivity coefficient of ϕ
κ	wave number
κ_c	cutoff wave number
κ_i	wave number corresponds to the integral scale of turbulence
κ_K	wave number corresponds to the Kolmogorov scale of turbulence
κ_v	von Karman constant
ν	kinematic viscosity of the fluid
ν_t	eddy viscosity
ϕ	flow variable
ρ	density of the fluid
σ_i	target standard deviation of u_i'
σ_k	closure coefficient in the k-equation
σ_ε	closure coefficient in the ε-equation
τ_{ij}	turbulent stress tensor
τ_w	wall shear stress

Subscripts

e, w, n, s	east-, west-, north-, and south-face of a control volume, respectively
i, j, k	Cartesian tensor indices
P, E, W, N, S	control volume indices

Other Symbols

$\bar{\cdot}$	filtered quantity
$\langle\cdot\rangle$	time-averaged quantity

Acronyms

CDS	Central Differencing Scheme
CFD	Computational Fluid Dynamics
CV	Control Volume
DES	Detached Eddy Simulation
DNS	Direct Numerical Simulation
ERCOFTAC	European Research Community on Flow, Turbulence and Combustion
FSM	Flow Simulation Methodology
LES	Large Eddy Simulation
LNS	Limited Numerical Scales
PRNS	Partially Resolved Numerical Simulation
RANS	Reynolds-Averaged Navier-Stokes
SIMPLE	Semi-Implicit Method for Pressure-Linked Equations
SGS	Subgrid Scale
STREAM	Simulation of Turbulent Reynolds-averaged Equations for All Mach numbers
TVD	Total Variation Diminishing
URANS	Unsteady RANS
UMIST	Upstream Monotonic Interpolation for Scalar Transport
VLES	Very Large Eddy Simulation

Chapter 1

Introduction

1.1 Motivation

Owing to increasing urbanization and concern of an accidental or deliberate release of a hazardous material in an urban (built-up) environment, the understanding of the wind flow and pollutant dispersion in an urban area is gaining importance. The main approaches to study the wind flow and contaminant transport in an urban environment include field measurements, laboratory experiments, and numerical simulations using computational fluid dynamics (CFD). Field and laboratory experiments can provide valuable information on flow characteristics and pollutant distributions by measurements and flow visualization, but the cost to conduct these experiments is expensive. With the rapid development of numerical methods and advancements in computer technology, CFD has been widely used to study urban flow and dispersion. The common methodologies in CFD include direct numerical simulation (DNS), large eddy simulation (LES), and Reynolds-averaged Navier-Stokes (RANS) simulation. Each simulation approach has its own advantages and weaknesses.

DNS resolves all the scales of motion from the energetic large scales to the dissipative small scales directly, without requiring any modeling. In consequence, of the three methodologies for CFD cited above, DNS is expected to provide the most accurate predictions of the flow. However, the associated computational cost of DNS is extremely high. Ferziger and Peric (2002) reported that the number of grid points required to simulate a three-dimensional turbulent flow in DNS is proportional to $\mathrm{Re}_L^{9/4}$, where Re_L is the Reynolds number based on the integral scales of the flow. Because the transport equations in DNS necessarily requires a time-stepping for the local tendency term and the time step is related to the grid size, the total computational cost for DNS actually scales as Re_L^3. This rapid

increase of computational effort with Re_L prohibits the application of DNS to high Reynolds number flows.

The RANS approach corresponds to the opposite end of the computational complexity spectrum. In this approach, only the time- (or ensemble-) averaged flow properties are resolved with all other scales of motion being modeled. The computational cost of RANS is independent of the Reynolds number, except for wall-bounded flows where the number of grid points required in the near-wall region is proportional to $\ln(Re_L)$ [Pope, 2000]. Because of its computational efficiency, RANS is the most commonly used CFD methodology for the simulation of turbulent flows encountered in industrial and engineering applications. However, the RANS approach can perform poorly in the prediction of the features in complex flows (e.g., bluff body flows) which tend to be dominated by coherent large-eddy structures. Because most turbulence models used in RANS are empirically tuned to optimize their performance in simple and thin shear flows where the mean pressure gradient and mean streamline curvature are small, RANS is generally unable to capture correctly the geometry-dependent large eddies in many complex flows.

The basic idea of LES is to resolve only the large-scale motions in a turbulent flow and model the small-scale (unresolved) motions. The latter scales of motion are expected to be more universal and, hence, easier to model as a consequence. In principle, LES is expected to be more accurate than RANS because the large-scale motions are explicitly resolved. Unfortunately, the application of LES to wall-bounded flows, particularly at high Reynolds numbers, is severely restricted owing to the grid resolution requirements for LES to resolve the viscous small-scale motions near the wall. Chapman (1979) estimated that the number of grid points needed for LES to resolve these near-wall small-scale motions is approximately proportional to $Re_L^{1.8}$.

In order to reduce the significant computational cost of near-wall resolved LES, while improving on predictive accuracy of RANS over a broad range of turbulent flows, an alternative that has been proposed is the use of a hybrid RANS/LES methodology. The concept underlying this methodology is to combine the computational efficiency of RANS for modeling the flow in the near-wall regions, with the predictive accuracy of LES for simulating the large-scale turbulent flow structures in regions away from the walls (or, any other solid surfaces).

A built-up (urban) environment consists of an arbitrary aggregation of buildings and other obstacles. The interaction of the flow with these rough elements makes the flow structures in an urban area very

complex. The flow phenomena can include impingement, recirculation, separation and reattachment. These complex urban geometries can result in large spatial variations in turbulence length and time scales that can impose severe restrictions on both the time step and grid resolution required in a numerical simulation. Therefore, most numerical investigations of urban flows are focused on modeling the flow and dispersion in a street canyon (the basic geometric unit of an urban canopy) or an array of obstacles with simple geometry. These simplified geometric configurations are ideal for fundamental studies of the physical processes (e.g., exchanges of momentum, heat and mass) that occur around the buildings and the flow within and above them.

RANS approaches have been widely used to study factors that affect the flow patterns and pollutant transport in a street canyon, including the building-height-to-street-width ratio (e.g., Hunter et al., 1992; Baik and Kim, 1999), wind direction (e.g., Kim and Baik, 2004), and thermal effect (e.g., Sini et al., 1996; Kim and Baik, 1999). However, many of RANS studies were performed on a two-dimensional street canyon (i.e., the length of the street in the spanwise direction was assumed infinitely long), for which the turbulent transport in the spanwise direction is not important. Several LES studies (e.g., Liu and Barth, 2002; Walton and Cheng, 2002; Liu et al., 2004) have been applied to study flow and dispersion in a more realistic three-dimensional street canyon. In these LES computations, periodic conditions for the flow field were applied in both the streamwise and spanwise directions of the canyon. As a result, the flow was essentially fully-developed (viz., reached streamwise equilibrium) within the street canyon in these LES studies.

In comparison to the street canyon flow, developing flow over an array of obstacles better resembles the urban flow in a more realistic setting (e.g., real cityscape). However, the associated computational cost to simulate a developing flow over an obstacle array is significantly greater than that for a fully-developed flow in a street canyon. Most numerical studies for a developing flow over a group of obstacles were performed using RANS (e.g., Lien and Yee, 2004; Hsieh et al., 2007a; Santiago et al., 2007) due to its relatively low computational cost. In contrast, only a few LES studies of the developing flow in an obstacle array were conducted (e.g., Hanna et al., 2002; Shi et al., 2008) owing to the high computational cost.

The complex nature of flow in a built-up area is dominated by unsteady large-scale turbulent structures. The recognition, that RANS is unable to accurately capture these flow structures and that LES is computationally expensive, provides the motivation for the investigation of a hybrid

RANS/LES simulation approach. It is hoped that this approach can be used to predict the complex turbulent flow in an urban environment, with a reasonable computational efficiency.

1.2 Hybrid Numerical Simulation Approaches

Hybrid RANS/LES is a relatively new flow simulation methodology, and generally it can be classified into two major categories: namely, zonal and non-zonal approaches. In the zonal approach, the computational domain is divided into distinct RANS and LES zones, in which conventional eddy-viscosity-type RANS and subgrid scale (SGS) turbulence models are used in the RANS and LES zones, respectively. For example, Davidson and Peng (2003) used a two-equation k-ω turbulence model (where k and ω denote the turbulence kinetic energy and specific dissipation rate with dimension of inverse time, respectively) in the RANS zone and a one-equation k-l SGS model (where l denotes a turbulence length scale) in the LES zone. Alternatively, Tucker and Davidson (2004) adopted one-equation k-l RANS and SGS models in the RANS and LES regions, respectively. Other variants of RANS/SGS turbulence models applied in the RANS/LES zones have also been investigated (e.g., Hamba, 2003; Temmerman et al., 2005; Larsson et al., 2007).

The RANS and LES solutions are coupled through the interface between these two zones, where information on the flow is exchanged (two-way interaction). The interface location that separates the two zones can be explicitly specified by a given wall-normal distance (e.g., Davidson and Peng, 2003; Temmerman et al., 2005) or dynamically determined based on the RANS and LES turbulence length scales (Tucker and Davidson, 2004). In the latter approach, the location is chosen as the minimum of the RANS length scale (an integral length scale) and the LES length scale (a grid spacing).

Owing to the different averaging procedures used in the RANS (statistical averaging) and LES (spatial filtering) regions, which give considerably different spectral properties in the RANS and LES solutions, there is an incompatibility of the flow properties around the modeling interface in the zonal approach. A good example of the effect of this incompatibility on the prediction of the flow can be found in the simulation of a plane channel flow, where a non-physical buffer layer appears in the vicinity of the modeling interface between the RANS and LES regions. While the resolved RANS and LES turbulence are comparable at the interface, the RANS model provides a much larger modeled turbulence than LES. This yields a larger total (resolved plus modeled) turbulence in the RANS zone than in the LES region, and can result in unphysical discontinuities in the flow quantities (e.g., velocities or eddy viscosities) across the interface. For example, both Davidson and Peng (2003)

and Hamba (2003) observed a kink in the mean streamwise velocity profile around the modeling interface in the simulation of a plane channel flow, in spite of the fact that these investigators used different turbulence closures in the RANS regions. This suggests that the observed kink in the mean velocity profile is independent of the turbulence closure scheme adopted for the simulation. Several strategies have been proposed to circumvent the velocity shift problem. Temmerman et al. (2005) damped the modeled RANS turbulence in the vicinity of interface to reduce the total turbulence in the RANS zone. Another remedy is to introduce forcing to increase the resolved turbulence around the interface. The forcing can be obtained either from a stochastic backscatter model (Piomelli et al., 2003), or from turbulent fluctuations obtained from synthetic turbulence (Batten et al., 2004; Davidson and Billson, 2006) or extracted from a reference DNS or LES database of a fully-developed channel flow (Davidson and Dahlstrom, 2005; Larsson et al., 2007).

In the non-zonal approach, a single generalized turbulence model is used in the entire computational domain. This approach offers a unified simulation framework that spans the continuous spectrum of flow modeling/simulation schemes from RANS to LES (and even DNS). In these schemes, the generalized turbulence model can function as a RANS turbulence closure model or as a LES SGS model, depending on the local grid resolution or flow properties. From a theoretical point of view, the unified modeling approach can be achieved in principle by applying a temporal filter to the Navier-Stokes equations in the manner suggested by Liu and Shih (2006). The "width" of this temporal filter defines explicitly which scales of the turbulent flow motion are resolved. Depending on the width of the temporal filter (or, equivalently, cutoff frequency) imposed on the Navier-Stokes equations, the velocities obtained from the simulation can be interpreted as a statistical average as in RANS, as partially resolved large-scale velocity fluctuations as in LES, or as fully resolved (instantaneous) velocity fluctuations as in DNS. Since there is no zonal interface in this approach, the flow properties across the entire computational domain are continuous everywhere.

A well-known example of the non-zonal approach is the detached-eddy simulation (DES) introduced by Spalart et al. (1997). In the original DES formulation, the one-equation Spalart-Allmaras (SA) model (Spalart and Allmaras, 1994) for the turbulent viscosity was used. Here, the SA model (which was designed originally for aerodynamic flows) is utilized in such a way that it behaves as a SGS model when the model length scale switches from the use of a wall-normal distance (RANS length scale) to a grid spacing (LES length scale). In general, DES can be formulated with any RANS model, simply by modifying the turbulence length scale used in the RANS model. For example, Strelets (2001) modified the length scale used in the modeling of the viscous dissipation term of the *k*-

equation to give a DES based on the k-ω turbulence model. Successful applications of DES to various massively separated flows (e.g., airfoil at high angles of attack and flow over a circular cylinder) were reported by Strelets (2001) and Squires et al. (2002). However, when Nikitin et al. (2000) and Piomelli et al. (2003) used DES (based on the SA model) to simulate plane channel flow, they found that DES produced a non-physical buffer layer, similar to that observed in the zonal approach, but there was no kink in the mean streamwise velocity profile in these DES results.

In another type of non-zonal approach, a generalized turbulence model is obtained by rescaling a conventional RANS model through the introduction of a resolution control function F_R. Since RANS and LES have the same form of averaged or filtered transport equations, the unknown turbulent stress tensor τ_{ij} in the filtered momentum equation can be modeled as $\tau_{ij} = F_R \tau_{ij}^{RANS}$, where τ_{ij}^{RANS} is the modeled Reynolds stress tensor available from a RANS model. The role of F_R is to characterize the degree of modeling required to represent the unresolved scales of turbulent flow motion. A constraint on F_R is that its value must be confined to lie in the range between zero and one. The generalized turbulence model behaves as a RANS model when $F_R \to 1$, in the sense that all scales of motion of the turbulence are modeled in this case. Alternatively, when $F_R \to 0$, the generalized turbulence model vanishes and the simulation behaves as DNS in the sense that all scales of the turbulent flow motion are resolved explicitly. In between these two limits, the generalized turbulence model behaves as a LES-type subscale stress model in the sense that only the scales of turbulent flow motion smaller than the filter width are modeled. This approach was first introduced by Speziale (1998a), and has been modified and generalized in the form of the flow simulation methodology (FSM) advocated by Fasel et al. (2002), the limited numerical scales (LNS) approach proposed by Batten et al. (2004), and the partially resolved numerical simulation (PRNS) scheme introduced by Liu and Shih (2006). The main difference between these strategies lies in the different formulations for F_R. In this thesis, the acronym PRNS introduced by Liu and Shih (2006) will be used to refer these similar strategies.

While any RANS model can be used in PRNS, a more sophisticated RANS model is usually required to better predict τ_{ij} in complex turbulent flows. For example, Speziale (1998a) used an explicit algebraic stress model to study a flat-plate boundary layer at zero pressure gradient and a transonic flow over a swept wing, whereas Batten et al. (2004) adopted a non-linear k-ε turbulence model (where ε is the dissipation rate of k) to investigate a plane channel flow. Similarly, Hsieh et al. (2007b) and Lien et al. (2008) used the standard k-ε turbulence model in their PRNS studies. Hsieh et al. (2007b) compared their PRNS results to the corresponding unsteady RANS (URANS) results for a

fully-developed flow over a wall-mounted matrix of cubes, and showed that PRNS generally outperformed URANS in terms of its predictive accuracy for the mean velocities and Reynolds stresses. Lien et al. (2008) also demonstrated better performance of PRNS over URANS for the prediction of the mean wind-speed and wind-direction in an urban environment.

1.3 Study Objective

A new generalized functional form for F_R in PRNS is proposed in this thesis. The main objective of this study is to validate and assess the predictive performance of this proposed functional form in PRNS over a variety of turbulent flows pertinent to flows in an urban environment. The numerical predictions of PRNS for these flows will also be compared to those of URANS and LES, in order to evaluate the capability and accuracy of PRNS against other (more conventional) simulation approaches.

Three benchmark test cases are considered in this thesis. The first two cases are fully-developed wall-bounded turbulent flows; namely, plane channel flow (attached flow) and flow over a wall-mounted matrix of cubes in a plane channel (separated flow). These fully-developed flows are useful for the validation of PRNS, because streamwise and spanwise periodic conditions can be applied in the numerical computation, eliminating the need to specify appropriate inflow, outflow and lateral boundary conditions for the problem. The third case is a developing flow over a matrix of cubes, which mimics the flow in an urban area.

1.4 Thesis Outline

Chapter 2 introduces the governing equations and the associated turbulence models used in the present research. The formulation of the newly proposed F_R in PRNS and its implementation in the k-ε model framework are also included in this chapter. Chapter 3 presents the numerical method and the boundary conditions used in the test problems investigated in this thesis. Chapters 4 to 6 describe the numerical results of PRNS, in comparison to other numerical predictions (i.e., URANS and LES predictions) and experimental measurements, in a plane channel flow (Chapter 4), a fully-developed flow over a matrix of cubes (Chapter 5), and a developing flow over a matrix of cubes (Chapter 6). Chapter 7 highlights the main findings and provides suggestions for future work.

Chapter 2

Mathematical Formulation

The motion of fluid flow is governed by the Navier-Stokes equations. In order to reduce the computational cost associated with the numerical simulation of turbulent flows that have a wide range of scales of motion, a filter (or averaging operator) can be applied to the Navier-Stokes equations so that only the scales of interest are resolved. The turbulence closure problem arises as a result of the filtering procedure which gives rise to undetermined subscale turbulent stresses. These turbulent stresses (which cannot be explicitly resolved) must be modeled in order to close the filtered momentum equation. The description of filtering procedure and turbulence closure models commonly used in RANS, LES and PRNS are presented in this chapter.

2.1 Governing Equations of Fluid Motion

The governing equations of mass and momentum for an incompressible and neutrally-stratified flow in a Newtonian fluid can be written in Cartesian tensor notation as

$$\frac{\partial u_j}{\partial x_j} = 0\,, \tag{2.1}$$

$$\frac{\partial u_i}{\partial t} + \frac{\partial}{\partial x_j}\left(u_j u_i\right) = -\frac{1}{\rho}\frac{\partial p}{\partial x_i} + \frac{\partial}{\partial x_j}\left[\nu\left(\frac{\partial u_i}{\partial x_j} + \frac{\partial u_j}{\partial x_i}\right)\right], \tag{2.2}$$

where u_i is the instantaneous velocity component in the x_i-direction; t is the time; p is the pressure; and, ρ and ν are the density and kinematic viscosity of the fluid, respectively. In this thesis, i = 1, 2,

and 3 represents the streamwise x, vertical (wall-normal) y, and spanwise z directions; $x_i = (x, y, z)$ and $u_i = (u, v, w)$.

When a filtering (or averaging) operator is applied to an instantaneous flow variable ϕ, the variable can be decomposed as

$$\phi = \overline{\phi} + \phi' , \tag{2.3}$$

where $\overline{\phi}$ is the filtered (or averaged) component of ϕ that can be directly resolved, and ϕ' is the departure of $\overline{\phi}$ from ϕ. Assuming that the filtering and differentiation operations commute, the Navier-Stokes equations after filtering become

$$\frac{\partial \overline{u}_j}{\partial x_j} = 0 , \tag{2.4}$$

$$\frac{\partial \overline{u}_i}{\partial t} + \frac{\partial}{\partial x_j}\overline{u}_j\overline{u}_i = -\frac{1}{\rho}\frac{\partial \overline{p}}{\partial x_i} + \frac{\partial}{\partial x_j}\left(2\nu\overline{S}_{ij} - \tau_{ij}\right), \tag{2.5}$$

where $\overline{S}_{ij} = \left(\partial\overline{u}_i/\partial x_j + \partial\overline{u}_j/\partial x_i\right)/2$ is the filtered strain-rate tensor. The turbulent stress tensor τ_{ij} is introduced due to the filtering procedure, resulting in more unknowns than there are equations. This is known as the turbulence closure problem. From a theoretical point of view, the specific filter applied to the Navier-Stokes equations defines the physical properties of the filtered flow variables. From a numerical simulation point of view, the model used for the turbulent stress tensor represents the effects of the unresolved scales of motion on the large-scale (filtered) momentum flux.

2.2 Reynolds-Averaged Navier-Stokes Simulation

The idea of Reynolds averaging is to decompose an instantaneous flow field into time- (or ensemble-) averaged mean velocity and fluctuating velocity fields. Accordingly, in the RANS approach only the mean flow properties are computed, whereas all scales of turbulent fluctuations are modeled. For statistically steady flows, ϕ in the RANS approach is averaged in time as

$$\overline{\phi}(x_i) = \lim_{T\to\infty} \frac{1}{T} \int_{t}^{t+T} \phi(x_i, t')\, dt', \tag{2.6}$$

where T is the averaging time interval which must be larger than the largest time scale of the fluctuations. For unsteady flows, ϕ in the unsteady RANS (URANS) approach is considered as ensemble average defined as

$$\overline{\phi}(x_i, t) = \lim_{N\to\infty} \frac{1}{N} \sum_{n=1}^{N} \phi_n(x_i, t), \tag{2.7}$$

where N is the number of flow realizations.

The turbulent stresses required for the closure of the Reynolds-averaged momentum equation, known as the Reynolds stresses ($\overline{u_i' u_j'}$), represent the mean momentum fluxes induced by the turbulence. The classical approach to model this term is to adopt the eddy viscosity concept originally proposed by Boussinesq (1877), which assumes a linear constitutive relationship between the turbulent stresses and mean strain-rate tensors:

$$\tau_{ij}^{RANS} \equiv \overline{u_i' u_j'} = \frac{2}{3} k \delta_{ij} - 2\nu_t \overline{S}_{ij}, \tag{2.8}$$

where u_i' is the turbulent fluctuating velocities, $k \equiv \overline{u_i' u_i'}/2$ is the (total) turbulence kinetic energy, δ_{ij} is the Kronecker delta, and ν_t is the eddy viscosity. Analogous to the effect of molecular viscosity in the molecular transport of momentum, the eddy viscosity characterizes the effect of turbulent eddies on the transfer and mixing of momentum. Based on dimensional analysis, the eddy viscosity can be estimated from a product of length scale (L_t) and velocity scale (V_t) of turbulent eddies as

$$\nu_t \sim L_t V_t. \tag{2.9}$$

There are three types of eddy viscosity models in general; namely, zero-equation, one-equation and two-equation models. The first two approaches rely on the prescription (or algebraic specification) of a turbulence length scale, which is generally difficult to define in complex flows such as separated flows.

The most widely used turbulence closure for RANS is the two-equation k-ε model, where ε is the dissipation rate of k. Within the framework of the k-ε model, the turbulent length and velocity scales are estimated as

$$L_t \sim k^{2/3}/\varepsilon \,,\; V_t \sim k^{1/2} \,, \tag{2.10}$$

so the eddy viscosity is determined as

$$\nu_t = C_\mu \frac{k^2}{\varepsilon} \,, \tag{2.11}$$

where C_μ is a closure constant. The transport equations for k and ε in the standard (high-Re) k-ε model are given by

$$\frac{\partial k}{\partial t} + \frac{\partial}{\partial x_j}\overline{u}_j k = \frac{\partial}{\partial x_j}\left(\frac{\nu_t}{\sigma_k}\frac{\partial k}{\partial x_j}\right) + P_k - \varepsilon \,, \tag{2.12}$$

$$\frac{\partial \varepsilon}{\partial t} + \frac{\partial}{\partial x_j}\overline{u}_j \varepsilon = \frac{\partial}{\partial x_j}\left(\frac{\nu_t}{\sigma_\varepsilon}\frac{\partial \varepsilon}{\partial x_j}\right) + \frac{\varepsilon}{k}\left(C_{\varepsilon 1}P_k - C_{\varepsilon 2}\varepsilon\right), \tag{2.13}$$

where $P_k \equiv -\tau_{ij}^{RANS}\,\partial\overline{u}_i/\partial x_j = 2\nu_t \overline{S}_{ij}\overline{S}_{ij}$ is the (modeled) production of turbulence kinetic energy. The closure coefficients in the standard k-ε model are given by (Launder and Spalding, 1974)

$$C_\mu = 0.09 \,,\; \sigma_k = 1.0 \,,\; \sigma_\varepsilon = 1.3 \,,\; C_{\varepsilon 1} = 1.44 \,,\; C_{\varepsilon 2} = 1.92 \,, \tag{2.14}$$

where these coefficients have been determined by a comprehensive data fitting over a wide range of canonical turbulent flows. For example, the production of turbulence energy in a simple turbulent shear flow is $P_k = -\overline{u'v'}\,\partial\overline{u}/\partial y$, where $\partial\overline{u}/\partial y$ is the mean velocity shear. Substituting $\overline{u'v'} = -\nu_t\,\partial\overline{u}/\partial y$ and $\nu_t = C_\mu k^2/\varepsilon$ into P_k and rearranging, yields

$$\left(\frac{\overline{u'v'}}{k}\right)^2 = C_\mu \frac{P_k}{\varepsilon}. \tag{2.15}$$

Experimental measurements in many different shear flows showed that $\left|\overline{u'v'}\right|/k \approx 0.3$ in equilibrium regions where $P_k/\varepsilon \approx 1$ (Townsend, 1980). This leads to the value of $C_\mu = 0.09$ that is widely used in the various k-ε model variants. The standard k-ε model will be used for the URANS calculations in this thesis.

2.3 Large Eddy Simulation

The concept of LES is to resolve the large scales of motion in a turbulent flow that are geometry dependent, and to model the small scales of motion which are expected to be more universal. The equation of motion for the filtered velocity field computed in LES can be obtained by applying a low-pass spatial filter to the Navier-Stokes equations, which results in the separation of the large and small scales of motion. A spatially-filtered large-scale flow variable is defined as

$$\overline{\phi}(x_i,t) = \int G(x_i - x_i', \overline{\Delta})\phi(x_i',t)dx_i', \tag{2.16}$$

where the integration is applied over the entire flow domain, and $G(x_i - x_i', \overline{\Delta})$ is the filter kernel with filter width $\overline{\Delta}$. If a top-hat spatial filter is used, Eq. (2.16) becomes

$$\overline{\phi}(x_i,t) = \frac{1}{\overline{\Delta}} \int_{x_i-\overline{\Delta}/2}^{x_i+\overline{\Delta}/2} \phi(x_i',t)\, dx_i'. \tag{2.17}$$

In most practical applications of LES performed using a finite-volume discretization method, an implicit filter (i.e., volume averaging) is applied in which the spatial filter width $\overline{\Delta}$ is related to the grid spacing used in the discretization of the computational flow domain. A common filter width is taken as $\overline{\Delta} = (\Delta x \Delta y \Delta z)^{1/3}$, where Δx, Δy and Δz are the grid spacings in the three coordinate directions at a local grid cell. Physical scales of motion that are larger than $\overline{\Delta}$ can be explicitly resolved.

The turbulent stresses required for the closure of the spatially-filtered momentum equation, referred to as the residual or subgrid scale (SGS) stresses, represent the SGS momentum fluxes caused by the small (unresolved) scales. The most popular SGS model is the Smagorinsky model (Smagorinsky, 1963), which is a zero-equation eddy viscosity model based on a simple mixing length concept. In this model, the SGS stresses are modeled as

$$\tau_{ij}^{SGS} \equiv \overline{u_i u_j} - \overline{u}_i \overline{u}_j = \frac{1}{3}\tau_{kk}^{SGS}\delta_{ij} - 2\nu_t^{SGS}\overline{S}_{ij}\,, \tag{2.18}$$

where the SGS eddy viscosity is given by

$$\nu_t^{SGS} = \left(C_s\overline{\Delta}\right)^2\sqrt{2\overline{S}_{ij}\overline{S}_{ij}}\,. \tag{2.19}$$

The model constant C_s usually assumes a value between 0.1 and 0.2, depending on the particular flow (Sagaut, 2006). Deardorff (1970) suggested C_s = 0.1 for plane channel flows, and this value is also commonly adopted for bluff body flows (e.g., Rodi, 1997; Cheng et al., 2003; Xie and Castro, 2006). One weakness of the Smagorinsky model is that ad-hoc adjustments of C_s are required in different types of turbulent flow or in the region near solid boundaries. To overcome this problem, Germano et al. (1991) proposed a dynamic procedure which dynamically computes C_s at every grid point in space and at every time step. However, the dynamic procedure may result in large negative values for C_s over long time interval or over extended regions of the flow domain, and this can lead to numerical instability or even divergence in the flow simulation (Sagaut, 2006). In this thesis, the Smagorinsky model with C_s = 0.1 will be employed for the LES calculations.

2.4 Partially Resolved Numerical Simulation

PRNS represents a form of hybrid RANS/LES approach that spans the continuous spectrum of flow simulation schemes from RANS to LES (and DNS as a special case). From a theoretical point of view, this can be achieved by applying a temporal filter to the Navier-Stokes equations as suggested by Liu and Shih (2006). A temporally-filtered large-scale flow variable is defined as

$$\overline{\phi}\left(x_i,t\right) = \int G\left(t-t',\Delta_T\right)\phi\left(x_i,t'\right)dt'\,, \tag{2.20}$$

where $G(t-t',\Delta_T)$ is the filter kernel with filter width Δ_T. If a top-hat temporal filter is used, Eq. (2.20) becomes

$$\overline{\phi}(x_i,t)=\frac{1}{\Delta_T}\int_{t-\Delta_T/2}^{t+\Delta_T/2}\phi(x_i,t')dt'. \tag{2.21}$$

It can be seen that $\overline{\phi}$ reduces to a Reynolds-averaged (or, equivalently time-averaged) flow quantity as $\Delta_T \to \infty$, and $\overline{\phi}$ is an instantaneous flow quantity as $\Delta_T \to 0$. For a finite Δ_T, $\overline{\phi}$ corresponds to a filtered flow quantity.

It should be noted that the temporal- and spatial-filtering operations are intimately linked. Let l_c be the cutoff length of a spatial filter. The corresponding cutoff wave number for this spatial filter is $\kappa_c = 2\pi/l_c$. Let $E(\kappa)$ denote the spectral energy density of the velocity fluctuations. The kinetic energy of the velocity fluctuations associated with those eddies of size given by the cutoff length scale $l_c = 2\pi/\kappa_c$ is $\kappa_c E(\kappa_c)$, and this cutoff length scale is associated with a cutoff velocity scale given by $v_c = \sqrt{\kappa_c E(\kappa_c)}$. In view of this, the cutoff time scale t_c for a temporal filter must be related to the cutoff length scale l_c for a spatial filter as $t_c = l_c/v_c$. When an implicit filter is used in PRNS, Δ_T is related to the time step Δt used in the simulation, and this time step must be appropriately selected so as to be consistent with the grid spacing $\overline{\Delta}$.

The turbulent stresses required for the closure of the temporally-filtered momentum equation, referred to as the subscale stresses, are modeled as

$$\tau_{ij}^{PRNS} \equiv \overline{u_i u_j} - \overline{u}_i \overline{u}_j = F_R \tau_{ij}^{RANS}, \tag{2.22}$$

where F_R is a resolution control function whose value lies between zero and one. Depending on the physical resolution requirements, PRNS can behave as RANS when $F_R \to 1$ or as DNS when $F_R \to 0$. Between these two limits, PRNS behaves as some form of LES (either very large eddy simulation (VLES) using relatively coarse grids or near-wall resolved LES using very fine grids). While PRNS is capable of bridging the gap between RANS, LES and DNS, it is mainly aimed at VLES for high Reynolds number turbulent flows (Speziale, 1998a; Liu and Shih, 2006). In VLES, the grid is

generally too large to resolve all the energy-containing motions, and the simulation is more dependent (compared to LES) on the modeling of the unresolved scales of turbulence (Pope, 2000). As a result, the predictive accuracy of PRNS depends on the capability of the turbulence model to represent the effect of the unresolved motions on the resolved ones. In order to give a proper representation of τ_{ij}^{PRNS} in a complex turbulent flow, a two-equation eddy-viscosity-based turbulence model (e.g., the *k*-ε model) is often required. Accordingly, Eq. (2.22) has the following explicit form

$$\tau_{ij}^{PRNS} = F_R\left(\frac{2}{3}k\delta_{ij} - 2\nu_t\overline{S}_{ij}\right) = \frac{2}{3}F_R k\delta_{ij} - 2\nu_t^{PRNS}\overline{S}_{ij}, \tag{2.23}$$

where the subscale eddy viscosity for PRNS is given by

$$\nu_t^{PRNS} = F_R\nu_t . \tag{2.24}$$

In practice, the term $\frac{2}{3}F_R k\delta_{ij}$ in Eq. (2.23) is absorbed into the filtered pressure term in Eq. (2.5) when solving the transport equation for the filtered momentum.

Several formulations for F_R have been introduced in the literature, and most of these involve a function that depends on the ratio of a physical turbulence length scale to a computational grid size ($\overline{\Delta}$). Speziale (1998a) proposed

$$F_R = \left[1 - \exp\left(-\beta\overline{\Delta}/l_K\right)\right]^n, \tag{2.25}$$

where l_K is the Kolmogorov length scale (whose value can be determined from a RANS model), and β and n are closure constants requiring calibration. In Eq. (2.25), $\overline{\Delta}/l_K$ is a measure of local resolution of the computational grid. When the grid resolution is very coarse relative to the smallest physical scales of turbulent flow motion, as embodied by the Kolmogorov length scale (i.e., $\overline{\Delta}/l_K \to \infty$), $F_R \to$ 1. Similarly, when the grid resolution is fine enough to resolve all the physical scales of motion (i.e., $\overline{\Delta}/l_K \to 0$), $F_R \to 0$. Based on Eq. (2.25), which is a spatially-dependent function for F_R, PRNS behaves like a hybrid simulation approach as the value of F_R varies across the computational domain. Proposed values of the calibration constants are $n = 1$ and β has a value in the order of 10^{-3}. Speziale

(1998b) and Fasel et al. (2002) used $\beta = 0.001$ and $\beta = 0.004$ to compute a flat-plate boundary layer flow, respectively, whereas Fasel et al. (2006) adopted $\beta = 0.008$ to simulate a backward-facing step flow. Fasel et al. (2006) reported that the prediction of flow fields strongly depends on the value of β.

Alternatively, Liu and Shih (2006) suggested

$$F_R \geq \left(\bar{\Delta}/l_{RANS}\right)^{4/3}, \tag{2.26}$$

where l_{RANS} is a characteristic length scale computed from a RANS model. It is important to note that Eq. (2.26) only provides an estimate for the smallest value of F_R that a given computational grid can support. In the approach advocated by Liu and Shih, this lower bound for F_R is applied throughout the entire computational domain. When a fixed value of F_R is used, PRNS becomes solely as RANS, LES or DNS, depends on the value of F_R. Such an approach can lead to a potential difficulty which can be described as follows. When a relative small constant value of F_R is used, conducting a PRNS is essentially equivalent to conducting a LES. In this case, the requirement of LES for a fine-grid resolution in the near-wall region (which contributes to its potentially high computational cost) will be applicable to PRNS as well.

A generalized functional form for F_R based on the turbulence energy spectrum is proposed in this thesis. When the cutoff wave number κ_c lies within the inertial subrange scales of motion for the turbulence (see Figure 2.1), the energy spectrum $E(\kappa) \propto \varepsilon^{2/3}\kappa^{-5/3}$ ($\kappa_i \leq \kappa_c \leq \kappa_K$) where κ_i and κ_K are the wave numbers corresponding to the integral and Kolmogorov scales of turbulence, respectively. Note that Kolmogorov's –5/3 power law is valid for high Reynolds number flows.

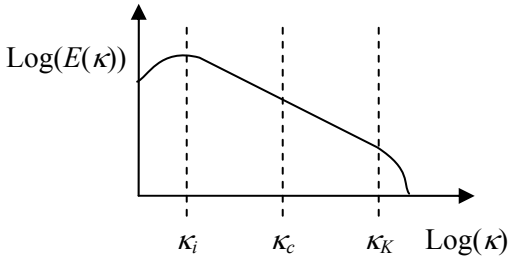

Figure 2.1. Schematic view of the energy spectrum of the turbulent velocity.

In view of this, the proposed functional form for $F_R \equiv F_R\left(\kappa_i, \kappa_c, \kappa_K\right)$ is given by

$$F_R = \frac{\int_{\kappa_c}^{\kappa_K} E(\kappa)\, d\kappa}{\int_{\kappa_i}^{\kappa_K} E(\kappa)\, d\kappa} = \frac{\kappa_K^{-2/3} - \kappa_c^{-2/3}}{\kappa_K^{-2/3} - \kappa_i^{-2/3}}, \tag{2.27}$$

where the definite integrals in the numerator and denominator of Eq. (2.27) represent the areas under the energy spectrum curve between κ_c and κ_K and between κ_i and κ_K, respectively. Therefore, F_R in Eq. (2.27) roughly resembles the ratio of the unresolved turbulence kinetic energy [approximated by $\int_{\kappa_c}^{\kappa_K} E(\kappa)\, d\kappa$] to the total turbulence kinetic energy [approximate by $\int_{\kappa_i}^{\kappa_K} E(\kappa)\, d\kappa$]. Note that in a practical implementation, κ_c is replaced by $\max\left[\kappa_i, \min\left(\kappa_c, \kappa_K\right)\right]$ in order to ensure the condition $F_R = 0$ when $\kappa_c \geq \kappa_K$, and $F_R = 1$ when $\kappa_c \leq \kappa_i$. The wave number is related to the length scale as

$$\left(\kappa_i, \kappa_c, \kappa_K\right) = 2\pi\left(l_i^{-1}, l_c^{-1}, l_K^{-1}\right), \tag{2.28}$$

where l_i, l_c and l_K are the integral, filter cutoff and Kolmogorov length scales, respectively. The characteristic length scale associated with the cutoff wave number is defined as

$$l_c = 2\max\left(\overline{\Delta}, |\vec{u}|\Delta t\right), \tag{2.29}$$

where $\overline{\Delta} = \left(\Delta x \Delta y \Delta z\right)^{1/3}$ is the local grid size, and $\vec{u}$ is the local convection velocity in the cell. The additional factor of 2 accounts for the Nyquist frequency imposed by the finite size of a grid cell (i.e., a grid cell of size $\overline{\Delta}$ cannot resolve a flow structure smaller than $2\overline{\Delta}$). The time step Δt is also included because the time step should be small enough to resolve adequately the advective transport of any grid-resolved flow structure. The size of time step is chosen using the Courant-Friedrichs-Lewy (CFL) condition:

$$\mathrm{CFL} = \frac{|\vec{u}|\Delta t}{\overline{\Delta}} \leq 1. \tag{2.30}$$

Owing to the imposed CFL condition in which $|\vec{u}|\Delta t \le \overline{\Delta}$, the cutoff length scale in Eq. (2.29) becomes:

$$l_c = 2\overline{\Delta} = 2\left(\Delta x \Delta y \Delta z\right)^{1/3}. \tag{2.31}$$

There are several ways to compute the integral and Kolmogorov length scales. One option is to obtain these length scales from an *a priori* steady RANS solution. However, this is not practical since this option requires a separate RANS calculation to be performed. In addition, at every grid point in space the values of l_i and l_K provided by RANS do not evolve with time, which is not suitable for unsteady flow calculations. Alternatively, the integral and Kolmogorov length scales can be estimated as:

$$l_i = C_\kappa k^{3/2}/\varepsilon\,,\; l_K = \left(\nu^3/\varepsilon\right)^{1/4}. \tag{2.32}$$

The quantities k and ε in Eq. (2.32) are obtained from the same turbulence model as used in RANS, except that ensemble-averaged advection velocity $\overline{u}_i$ in Eqs. (2.12) and (2.13) is replaced by the time-filtered advection velocity $\overline{u}_i$ obtained from the filtered (PRNS) momentum equation. Furthermore, the turbulence energy production term P_k $(= 2\nu_t \overline{S}_{ij}\overline{S}_{ij})$ in the PRNS approach is computed using ν_t from Eq. (2.11), rather than ν_t^{PRNS} from Eq. (2.24), in order to be consistent with the original k-ε model. Although the "energized" k and ε predicted by the PRNS approach are different from those obtained with the RANS counterpart, it was found from the channel flow calculations (which will be presented in Chapter 4) that the integral length scales predicted by both PRNS and RANS were very comparable when using the same (original) closure constants defined in Eq. (2.14). If ν_t^{PRNS} was used instead in the determination of the turbulence energy production, the closure constants for the present PRNS will probably require re-calibration. The implementation details are given in the flowchart, depicted in Figure 2.2.

Consider the decomposition of the time-filtered velocity as $\overline{u}_i = \langle \overline{u}_i \rangle + u_i''$, where $\langle \overline{u}_i \rangle$ is the time-averaged value of $\overline{u}_i$, and u_i'' is the departure of $\overline{u}_i$ from $\langle \overline{u}_i \rangle$. It can be shown that $P_k = 2\nu_t \overline{S}_{ij}\overline{S}_{ij}$, computed using $\overline{u}_i$ (as in PRNS), is larger than that computed using $\langle \overline{u}_i \rangle$ (as in RANS). In consequence, PRNS will over-predict k and ε (since P_k appears in both the k and ε equations) in

comparison with the corresponding values obtained from RANS. While the magnitudes of k and ε in PRNS and RANS are different, it was found that the resulting integral length scale, $l_i \propto k^{3/2}/\varepsilon$, has approximately the same order of the magnitude. In consequence, the minor differences in the determination of the length scale obtained from k and ε in either PRNS or RANS, can be absorbed into the closure constant C_κ that appears in the definition of l_i in Eq. (2.32). Speziale (1998a) noted that an estimation of l_K to an accuracy of 10% only required that ε be estimated to an accuracy of 50%. As a consequence, no closure constant is introduced in l_K. It is expected that the slight inaccuracy associated with the determination of l_K has little effect on the F_R value because $E(\kappa_K) \equiv E(2\pi/l_K)$ is very small here.

The only model constant in the present formulation for F_R requiring calibration is C_κ in l_i [cf. Eq. (2.32)]. When the value of C_κ (and consequently l_i) increases, the value of κ_i [defined in Eq. (2.28)] decreases. As a result, the value of F_R decreases because the value of the definite integral in the denominator of Eq. (2.27) increases (owing to the smaller value of κ_i). The optimal value of C_κ will need to be determined over a range of flow conditions. The PRNS-based k-ε turbulence model proposed by Hsieh et al. (2008) used C_κ = 40 to simulate a fully-developed plane channel flow (attached flow) and a fully-developed flow over a wall-mounted matrix of cubes (separated flow). They demonstrated that the performance of PRNS was quite similar to LES. This C_κ value was calibrated against the DNS data of Moser et al. (1999) for a fully-developed plane channel flow at Re_τ = 590 (see Chapter 4 for details). This value for C_κ will be used in the PRNS computations presented in this thesis.

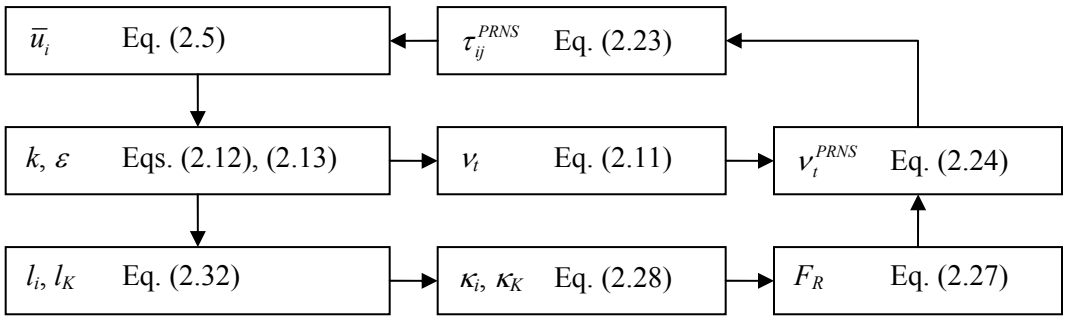

Figure 2.2. Flowchart of PRNS implementation.

2.5 Turbulence Statistics

Turbulence statistics of the flow are obtained by averaging the flow field in time. When a time-averaging operator is applied to a time-dependent filtered (resolved) flow variable $\overline{\phi}$, it can be decomposed as

$$\overline{\phi} = \left\langle \overline{\phi} \right\rangle + \phi'' , \tag{2.33}$$

where $\left\langle \overline{\phi} \right\rangle$ is the time-averaged value of $\overline{\phi}$, and ϕ'' is the fluctuation of $\overline{\phi}$ in which $\left\langle \phi'' \right\rangle = 0$. The angled brackets surrounding a quantity are used to denote the time average of that quantity. Applying the time-averaging operator to Eq. (2.5) yields the time-mean filtered momentum equation:

$$\frac{\partial}{\partial x_j}\left\langle \overline{u}_j \right\rangle \left\langle \overline{u}_i \right\rangle = -\frac{1}{\rho}\frac{\partial \left\langle \overline{p} \right\rangle}{\partial x_i} + \frac{\partial}{\partial x_j}\left(2\nu \left\langle \overline{S}_{ij} \right\rangle - \left\langle \tau_{ij} \right\rangle - \left\langle u_i'' u_j'' \right\rangle \right), \tag{2.34}$$

where

$$\left\langle u_i'' u_j'' \right\rangle \equiv \left\langle \overline{u}_i \overline{u}_j \right\rangle - \left\langle \overline{u}_i \right\rangle \left\langle \overline{u}_j \right\rangle . \tag{2.35}$$

The Reynolds stresses (obtained from time-averaging of the product of various fluctuating velocities) are calculated from the relationship

$$\left\langle \overline{u_i' u_j'} \right\rangle = \left\langle u_i'' u_j'' \right\rangle + \left\langle \tau_{ij} \right\rangle , \tag{2.36}$$

where $\left\langle u_i'' u_j'' \right\rangle$ and $\left\langle \tau_{ij} \right\rangle$ are the resolved and modeled components of Reynolds stresses, respectively. The resolved Reynolds stresses represent the contribution arising from the resolved fluctuating velocity field (which can be computed directly). Note that $\left\langle u_i'' u_j'' \right\rangle = 0$ if a steady RANS calculation is performed, and in this case Eq. (2.36) reduces to $\left\langle \overline{u_i' u_j'} \right\rangle = \overline{u_i' u_j'} = \tau_{ij}^{RANS}$ which is consistent with Eq. (2.8).

Chapter 3

Numerical Method

The transport equations for flow variables were solved numerically using a finite-volume method based on the STREAM code (Lien and Leschziner, 1994a). It uses a collocated storage arrangement for all flow variables. The Semi-Implicit Method for Pressure-Linked Equations (SIMPLE) algorithm (Patankar and Spalding, 1972) was employed to enforce mass conservation and to couple the pressure and velocity fields. In order to prevent checkerboard oscillations from developing in the pressure field when using a collocated approach, a nonlinear interpolation scheme (Rhie and Chow, 1983) was adopted to interpolate the cell face velocities from the adjacent nodal velocities at the cell centers. This chapter presents the discretization schemes utilized in the finite volume method and the boundary conditions used in the test problems investigated in this thesis, with emphasis on those details of the numerical algorithm that influence the outcome of a numerical solution.

3.1 Finite Volume Method

In the finite volume method, the solution domain is divided into a finite number of small control volumes. At the centroid of each control volume, all the flow variables stored there (the collocated storage arrangement) are to be calculated. The transport equations for all flow variables have a similar structure, which can be written in a generic conservation equation for a flow variable ϕ as:

$$\frac{\partial \phi}{\partial t} + \frac{\partial}{\partial x_j}\left(u_j \phi\right) = \frac{\partial}{\partial x_j}\left(\Gamma_\phi \frac{\partial \phi}{\partial x_j}\right) + S_\phi \,, \tag{3.1}$$

where Γ_ϕ and S_ϕ are the diffusion coefficient and source term, respectively.

The finite volume method uses the volume integral form of Eq. (3.1):

$$\int_{CV} \frac{\partial \phi}{\partial t} dV + \int_{CV} \frac{\partial}{\partial x_j}\left(u_j \phi\right) dV = \int_{CV} \frac{\partial}{\partial x_j}\left(\Gamma_\phi \frac{\partial \phi}{\partial x_j}\right) dV + \int_{CV} S_\phi dV \,, \tag{3.2}$$

in which the integration of the transport equation over each control volume (CV) provides an algebraic expression for ϕ at each grid node. For simplicity of explanation, consider a two-dimensional control volume (with a unit depth in the z direction) diagram shown in Figure 3.1, in which a typical control volume has a central node P and four faces denoted by e, w, n and s.

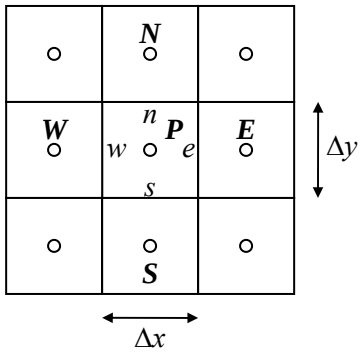

Figure 3.1. A two-dimensional control volume centered at node *P* and its neighboring nodes.

The resulting spatial discretization of Eq. (3.2) at a given node P for a two-dimensional control volume is

$$\frac{\partial \phi}{\partial t} + \frac{1}{\Delta x}\left[\left(u\phi - \Gamma_\phi \frac{\partial \phi}{\partial x}\right)_e - \left(u\phi - \Gamma_\phi \frac{\partial \phi}{\partial x}\right)_w\right] + \frac{1}{\Delta y}\left[\left(v\phi - \Gamma_\phi \frac{\partial \phi}{\partial y}\right)_n - \left(v\phi - \Gamma_\phi \frac{\partial \phi}{\partial y}\right)_s\right] = \overline{S}_\phi \,, \tag{3.3}$$

where $\overline{S}_\phi$ is the average value of the source term S_ϕ over the control volume. The face values of ϕ in Eq. (3.3) are expressed in terms of its adjacent nodal values by interpolation. In what follows, the discretization schemes used for approximation of convective and diffusive fluxes at the east face are illustrated. The same procedure can be applied to the other faces.

For the convective flux, the ϕ_e term is approximated by a second-order accurate central differencing scheme (CDS) for PRNS and LES computations:

$$\phi_e = \frac{\phi_P + \phi_E}{2}. \tag{3.4}$$

The second-order accurate Upstream Monotonic Interpolation for Scalar Transport (UMIST) scheme (Lien and Leschziner, 1994b), which is a total variation diminishing (TVD) scheme, is adopted for URANS calculations. For a flow moving in the positive x-direction where the advecting velocity $u_e > 0$, ϕ_e is approximated as

$$\phi_e = \phi_P + \frac{1}{2}\psi(r)(\phi_E - \phi_P), \tag{3.5}$$

where

$$r = \frac{\phi_P - \phi_W}{\phi_E - \phi_P}, \tag{3.6}$$

and

$$\psi(r) = \max\left[0, \min\left(2r, 0.25 + 0.75r, 0.75 + 0.25r, 2\right)\right]. \tag{3.7}$$

It is known that CDS tends to produce spurious oscillations (or wiggles) when the local cell Peclet number (a measure of the relative strength of advection to diffusion) is large (Versteeg and Malalasekra, 1995), but this deficiency can be removed through a sequence of grid refinement. The TVD schemes are formulated to provide oscillation-free solutions, but they are more numerically dissipative than CDS. This is because a TVD scheme can be rewritten as a combination of CDS with an additional numerical dissipation term (to damp out the potential spurious oscillations). In order to avoid excessive damping of the turbulent fluctuations in the flow simulation, CDS (which is less numerically dissipative than a TVD scheme) is widely used for LES. Similarly, CDS is adopted for PRNS.

The diffusive flux is discretized using CDS:

$$\left(\Gamma_\phi \frac{\partial \phi}{\partial x}\right)_e = \left(\frac{\Gamma_\phi}{\Delta x}\right)_e (\phi_E - \phi_P). \tag{3.8}$$

The transient term is discretized using a fully implicit, second-order accurate three-time-level method described in Ferziger and Peric (2002):

$$\left(\frac{\partial \phi}{\partial t}\right)_{n+1} = \frac{3\phi^{n+1} - 4\phi^{n} + \phi^{n-1}}{2\Delta t}, \tag{3.9}$$

where n+1 denotes the current time level, n and n−1 represent the previous time levels that is one and two time steps previous to the current time level, respectively.

3.2 Boundary Conditions

The specification of boundary conditions has direct influence on the results of a numerical simulation, and what type of boundary condition used depends upon the physical problem.

3.2.1 Wall

The wall (or a solid boundary) is the most common boundary encountered in confined flow problems. The no-slip condition is generally applied for all the velocity components at solid walls. At high Reynolds numbers, it is computational expensive to resolve the viscous small-scale flow motions near the wall due to the stringent requirement for a fine-grid resolution near the wall. In order to reduce computational cost in the near-wall regions, wall functions (or wall models) based on the logarithmic law-of-the-wall are frequently utilized to mimic the effects of the near-wall turbulence. The log-law is given by

$$u^{+} = \frac{1}{\kappa_v} \ln y^{+} + B, \tag{3.10}$$

where

$$u^{+} \equiv \overline{u}/u_{\tau}, \; y^{+} \equiv y u_{\tau}/\nu, \tag{3.11}$$

$u_{\tau} \equiv \sqrt{\tau_w/\rho}$ is the friction velocity, τ_w is the wall shear stress, κ_v = 0.41 is the von Karman constant, and B = 5.5 for a smooth wall. If the k-ε model is used, the log-law relationship for k and ε are expressed as (Pope, 2000):

$$k = C_\mu^{-1/2} u_\tau^2 \,,\ \varepsilon = u_\tau^3 / \kappa_v y \,. \tag{3.12}$$

Wall functions are applied at the first grid node adjacent to the wall. Ideally, this node should lie in the logarithmic layer ($y^+ > 30$) where the log-law is valid. In practice, the first node can be placed at $y^+ > 11.6$ (Versteeg and Malalasekra, 1995), where the value of $y^+ = 11.6$ represents the intersection of the linear sublayer law (i.e., $u^+ = y^+$) and the log-law. The wall shear stress (used as a source term within the discretized wall-parallel momentum equation) at the near-wall node *P* is estimated as

$$\tau_w = \frac{\rho u_\tau \overline{u}_P}{u^+}, \tag{3.13}$$

where $\overline{u}_P$ is the tangential velocity at node *P*, and u^+ is computed using Eq. (3.10). The friction velocity in Eq. (3.13) is calculated using either $u_\tau = C_\mu^{1/4} k_P^{1/2}$ [based on Eq. (3.12)] for URANS and PRNS or $u_\tau = \overline{u}_P / u^+$ for LES.

The volume-averaged production and dissipation rate of turbulence kinetic energy, used as source terms in the transport equation for *k* at node *P*, are prescribed as

$$P_k = \tau_w \frac{\overline{u}_P}{y_P} \,,\ \varepsilon_P = \frac{C_\mu^{4/3} k_P^{3/2}}{\kappa_v y_P}, \tag{3.14}$$

where y_P is the normal distance from node *P* to the wall, and τ_w is obtained from Eq. (3.13). The transport equation for ε at node *P* is not solved. Instead, the value of ε at this node is specified using ε_P in Eq. (3.14).

3.2.2 Periodic Boundary

Consider a flow that passes through an array of cubes mounted in a channel shown in Figure 3.2, where the geometry has a repeated pattern with pitch *Pi* (streamwise periodic length). At a distance sufficiently far downstream of the upwind edge of the array in the streamwise direction, the flow becomes fully developed and periodic. Under these conditions, the calculation can be performed using only one of the identical unit cells to reduce the computational time. The region within the two

dashed lines shown in Figure 3.2 (which identifies a unit cell in the array) is selected as a representative computational domain.

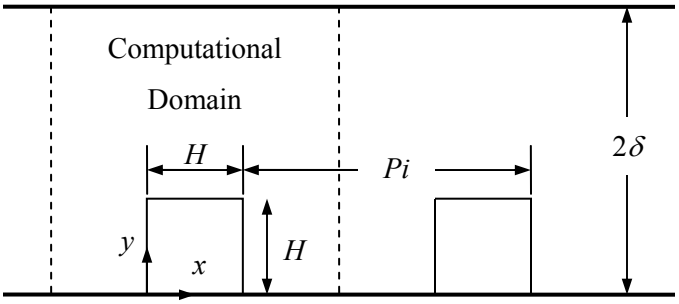

Figure 3.2. Schematic diagram of a channel containing an array of obstacles.

All solution variables in the periodic regime, except for the pressure, are identical at the inlet and outlet of the unit cell. The periodic relationship can be written as:

$$\phi\left(x_{inlet}, y, z\right) = \phi\left(x_{inlet} + Pi, y, z\right), \tag{3.15}$$

where $\phi = \overline{u}_i$ (i = 1, 2, 3), k and ε. Along the streamwise direction, the pressure drop across each unit cell is constant:

$$\overline{p}\left(x_{inlet}, y, z\right) - \overline{p}\left(x_{inlet} + Pi, y, z\right) = \text{a constant}. \tag{3.16}$$

According to Patankar et al. (1977), the pressure can be decomposed into:

$$\overline{p}\left(x, y, z\right) = \tilde{p}\left(x, y, z\right) - \beta x, \tag{3.17}$$

where $\tilde{p}$ is the periodic part of the pressure satisfying Eq. (3.15), and β is the pressure gradient across one unit cell. Substitution of Eq. (3.17) into Eq. (2.5) yields the momentum equation under the periodic condition

$$\frac{\partial \overline{u}_i}{\partial t} + \frac{\partial}{\partial x_j}\overline{u}_j\overline{u}_i = -\frac{1}{\rho}\frac{\partial \tilde{p}}{\partial x_i} + \frac{\partial}{\partial x_j}\left(2\nu\overline{S}_{ij} - \tau_{ij}\right) + \beta\delta_{i1}. \tag{3.18}$$

For a given Reynolds number, there is a corresponding pressure drop. The pressure gradient β is general unknown *a priori* and an arbitrary constant value is used as an initial guess at the first iteration. After the solution converges, the corresponding bulk mean velocity (U_b) at any fixed streamwise x-location can be evaluated as:

$$U_b = \left. \frac{\iint \overline{u}(x,y,z)\,dydz}{\iint dydz} \right|_x . \tag{3.19}$$

Using this value of U_b, the pressure gradient β is adjusted accordingly (for example, if U_b is lower than the experimental value, then β is increased), and the overall solution procedure is repeated until the desired Reynolds number (e.g., $\mathrm{Re}_H = U_b H/\nu$ where H is the height of the cube) is attained.

For a fully-developed plane channel flow with a given friction velocity, $\beta = \rho u_\tau^2/\delta$ (where δ is the channel half-width) is known *a priori*, since the pressure gradient in the channel flow is balanced by the wall shear stresses at the channel walls.

3.2.3 Inlet and Outlet

Flow properties at the inlet are specified by the Dirichlet condition. For (U)RANS approach, only mean profiles for the velocities and turbulence variables need to be prescribed, and these profiles are generally available from experimental data. In contrast, unsteady inlet fluctuations are required for PRNS and LES. The simplest approach to generate unsteady inflow conditions is to superimpose random fluctuations (white noise) on the inlet mean velocity profile. However, Schluter et al. (2004) and Jarrin et al. (2006) pointed out that these random fluctuations have no spatial or temporal correlations and that they dissipate quickly without sustaining turbulence within the solution domain. One simple method to address this problem is to construct a time-correlated fluctuation using white noise, as suggested by Hanna et al. (2002). In their approach, the turbulent fluctuation (u_i') is composed of a correlated component and a random component (r_i):

$$u_i'(t) = u_i'(t-\Delta t)\,R(\Delta t) + r_i(t)\,\sigma_i\sqrt{1-R^2(\Delta t)}\,, \tag{3.20}$$

where

$$R(\Delta t) = \exp(-\Delta t / T_L). \tag{3.21}$$

Here, r_i is a Gaussian random number that has zero mean and unit variance, and σ_i is the target standard deviation of u_i'. The autocorrelation function $R(\Delta t)$ is related to the computational time step Δt, where $R(\Delta t) \to 1$ as $\Delta t \to 0$, and $R(\Delta t) \to 0$ as $\Delta t \to \infty$. In this thesis, the integral time scale (T_L) of a developing boundary layer flow is estimated using a mixing length scale and the inlet mean velocity:

$$T_L = \frac{\kappa_v y}{U_{in}(y)}, \tag{3.22}$$

where y is the normal distance from the ground.

If the outlet is placed sufficiently downstream of any perturbations to the flow (e.g., obstacles), the flow at the outlet can be considered to be fully developed, in which case the Neumann condition can be applied to the flow variables. Here, the gradients of flow variables at the outlet plane are set to zero in the flow (streamwise) direction:

$$\frac{\partial \overline{u}}{\partial x} = \frac{\partial \overline{v}}{\partial x} = \frac{\partial \overline{w}}{\partial x} = \frac{\partial k}{\partial x} = \frac{\partial \varepsilon}{\partial x} = 0. \tag{3.23}$$

Chapter 4

Plane Channel Flow

A fully-developed plane channel flow, which is the simplest wall-bounded flow (in terms of geometry), has been studied extensively. In spite of its geometric simplicity, accurate prediction of turbulent channel flow remains a great challenge. The near-wall region of the channel contains flow structures (streaks) that are responsible for a major portion of the turbulence energy production (Robinson, 1991), and these structures must be resolved in order to obtain accurate numerical results. It was estimated that the number of grid nodes required to resolve the viscous near-wall turbulent motions is proportional to $\mathrm{Re}_L^{1.8}$ for LES (Chapman, 1979) and to $\mathrm{Re}_L^{2.25}$ for DNS (Ferziger and Peric, 2002), where Re_L is the Reynolds number based on the integral scales of the flow.

In order to alleviate the demanding near-wall grid resolution requirement for DNS and near-wall resolved LES, numerous simulation approaches, such as LES with wall models (Cabot and Moin, 1999; Benarafa et al., 2006) and hybrid RANS/LES, have been used to simulate turbulent channel flows. In the zonal hybrid approaches, different specifications of the modeling interface location (Davidson and Peng, 2003; Tucker and Davidson, 2004) and utilization of various turbulence models in the RANS/LES zones (Hamba, 2003; Temmerman et al., 2005), have been investigated. In the non-zonal hybrid approaches, DES (Nikitin et al., 2000; Piomelli et al., 2003) and PRNS (Batten et al., 2004; Hsieh et al., 2008) have been proposed.

Fully-developed turbulent channel flow is an ideal test case to use for validation of numerical simulation approaches because streamwise and spanwise periodic conditions can be applied in the numerical computation. This eliminates the need to specify appropriate inflow, outflow and lateral boundary conditions for the problem. The numerical performance of PRNS with the proposed functional form for F_R will be compared to that of URANS and LES for plane channel flow. In

addition, the quality of these simulations will be evaluated against results obtained from a DNS database for a fully-developed channel flow.

4.1 Problem Description

The DNS data of Moser et al. (1999) for a fully-developed turbulent plane channel flow at $\mathrm{Re}_\tau \equiv \delta u_\tau / \nu = 590$ (δ is the channel half width) was taken as the benchmark test case. This data was generated using 384 × 257 × 384 nodes in a computational domain with a physical extent of $L_x \times L_y \times L_z = 2\pi\delta \times 2\delta \times \pi\delta$ in the streamwise (x), wall-normal (y) and spanwise (z) directions, respectively. The mesh was uniform in the x- and z-directions and stretched in the y-direction with grid nodes concentrated near the wall. The grid resolution in terms of wall units was (Δx^+, Δy^+, Δz^+) ≈ (9.6, 0.05 → 7.2, 4.8). Figure 4.1 shows the mean velocity profile predicted by DNS agrees with the law-of-the-wall very well.

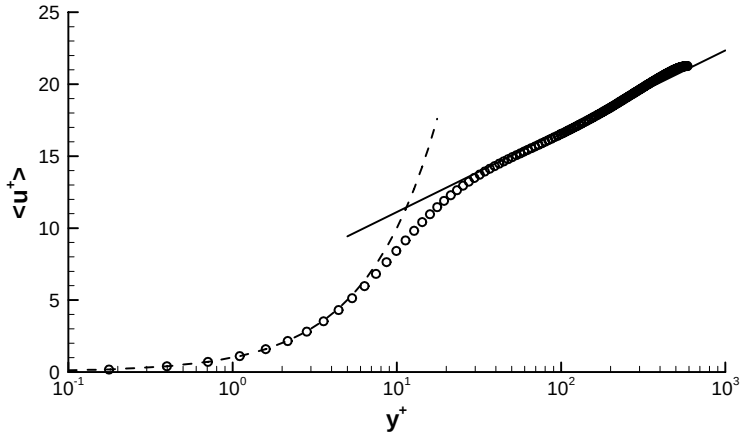

Figure 4.1. Mean velocity profile for a plane channel flow at Re_τ = 590. (○) DNS data of Moser et al. (1999); (– –) $\langle u^+ \rangle = y^+$; (—) $\langle u^+ \rangle = \ln(y^+)/0.41 + 5.5$.

4.2 Computational Aspects

Computations from URANS, PRNS and LES were performed using a uniform mesh for a computational domain having the same physical size as that used for the DNS study. Periodic boundary conditions were applied in both the streamwise and spanwise directions. Wall functions were utilized at the channel walls. Statistics of the flow were obtained by averaging over a horizontal plane parallel to the channel wall and in time.

The dependence of the flow solutions on grid resolution was investigated using two different grids of $N_x \times N_y \times N_z = 32 \times 32 \times 32$ (coarse grid) and $48 \times 48 \times 48$ (fine grid) in the numerical simulations. The grid resolution for the fine grid was $(\Delta x^+, \Delta y^+, \Delta z^+) \approx (80, 25, 40)$, where the first near-wall node was located at $y^+ \approx 12.5$ (which satisfied the requirement of $y^+ > 11.6$ for implementation of wall functions). A temporal resolution of $\Delta t u_\tau / \delta = 0.002$ and 0.001 was used for the coarse and fine grids, respectively. The time step sizes chosen satisfied CFL ≤ 1 [cf. Eq. (2.30)] throughout the computational domain for the given grid sizes. Results for the coarse and fine grids were time-averaged over 25000 and 50000 time steps (after the flow reached a statistically steady state), respectively, to ensure that time-averaged quantities satisfied statistical convergence.

Figure 4.2 shows an example of the prediction of streamwise mean velocity and root-mean-square (rms) velocity ($u'_{rms} \equiv \sqrt{\langle \overline{u'u'} \rangle}$) obtained with the coarse and fine grids. The agreement between the coarse- and fine-grid solutions for URANS is very good. However, the PRNS and LES solutions are sensitive to the grid resolutions, particularly for the predictions of rms velocity.

Note that the role of grid refinement on URANS, PRNS and LES is different. As URANS, PRNS and LES have the same form of filtered Navier-Stokes equations, the main difference that distinguishes these computations is the turbulence model used to describe the turbulent stress tensor. The turbulent stress tensor is modeled here using the eddy viscosity concept. The eddy viscosity for URANS (i.e., $\nu_t = C_\mu k^2 / \varepsilon$) does not associate with the grid spacing. The objective of grid refinement in URANS is to increase the numerical accuracy of the solution, and with a sufficiently fine grid it is possible to obtain grid independent solution in this case. In contrast, the eddy viscosities used for turbulence closure in PRNS and LES depend explicitly on the grid spacing. Here, grid refinement reduces the effect of the modeled eddy viscosities in the sense that the finer the grid resolution, the more turbulence is resolved. As a result, grid refinement for PRNS and LES increases the fidelity of solutions representing the turbulence physics. It is noted that the grid spacing directly influences the eddy viscosity for LES [i.e., $\nu_t^{SGS} = \left(C_s \overline{\Delta}\right)^2 \sqrt{2 \overline{S}_{ij} \overline{S}_{ij}}$], but indirectly affects the eddy viscosity for PRNS (i.e., $\nu_t^{PRNS} = F_R \nu_t$) through F_R. In the latter case, the dependence of F_R on grid spacing manifests itself through the cutoff length scale l_c ($= 2\overline{\Delta}$) [cf. Eqs. (2.27), (2.28) and (2.31)]. This is confirmed in Figure 4.2 where LES solutions are seen to be more sensitive to the grid resolution than PRNS. In the next section, only the results generated with the fine grid are presented.

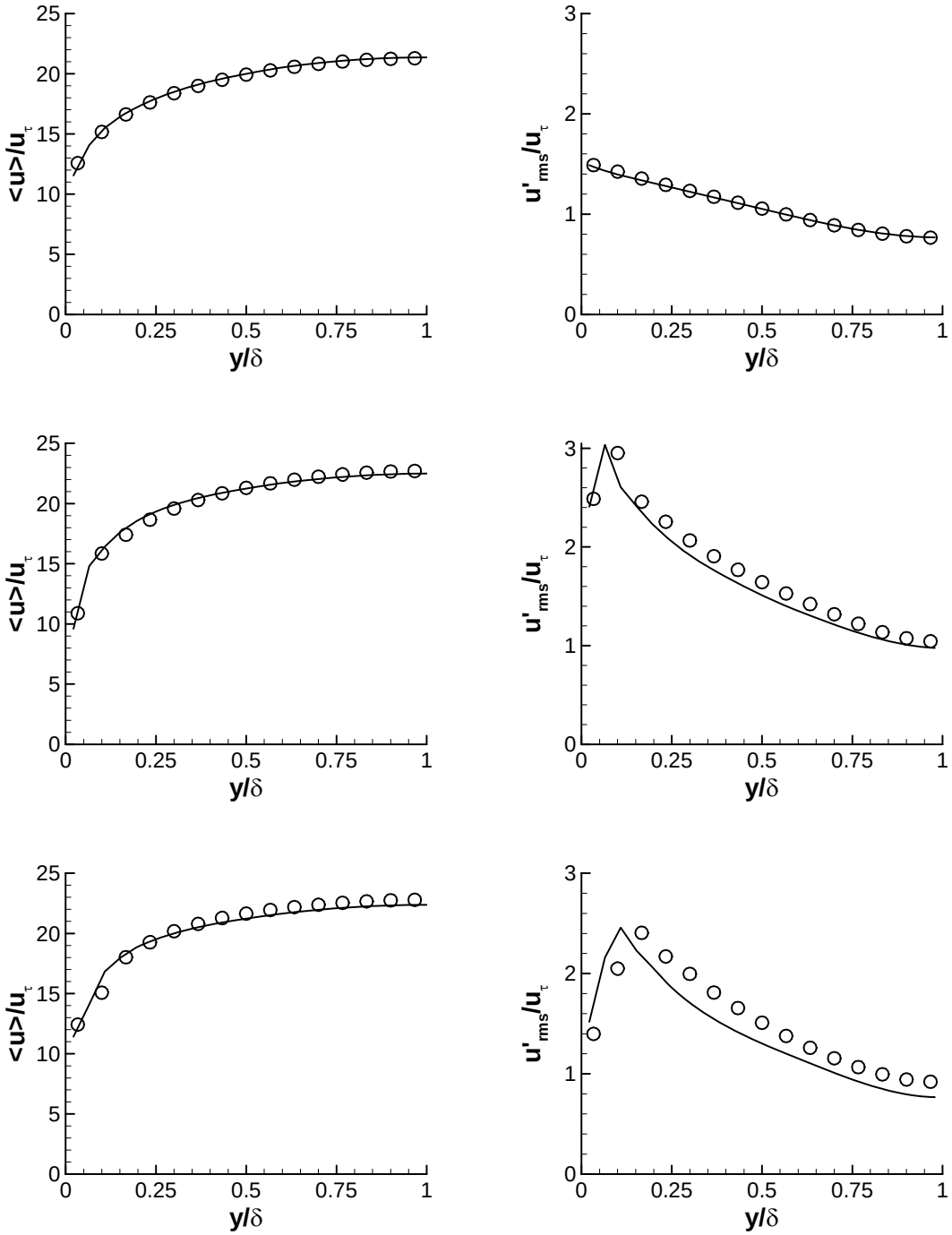

Figure 4.2. Grid sensitivity analysis: profiles of the streamwise mean and root-mean-square velocities obtained using URANS (top), PRNS (middle) and LES (bottom). (○) coarse grid (32 × 32 × 32); (—) fine grid (48 × 48 × 48).

4.3 Results and Discussion

4.3.1 Analytical Result

Fully-developed turbulent channel flow is statistically homogeneous in the streamwise and spanwise directions for all flow variables, except for the pressure:

$$\frac{\partial\langle\overline{\phi}\rangle}{\partial x}=\frac{\partial\langle\overline{\phi}\rangle}{\partial z}=0\,. \tag{4.1}$$

Applying the condition of Eq. (4.1) to the continuity equation gives:

$$\frac{\partial\langle\overline{u}_j\rangle}{\partial x_j}=0\;\Rightarrow\;\frac{\partial\langle\overline{v}\rangle}{\partial y}=0\,. \tag{4.2}$$

Integrating Eq. (4.2) from the lower channel wall at $y = 0$ to some normal distance y above the wall, and applying the impermeability condition at wall where $\overline{v}=0$, gives $\langle\overline{v}\rangle=0$ everywhere within the solution domain.

Applying the condition of Eq. (4.1) and $\langle\overline{v}\rangle=0$ to Eq. (2.34) for the mean streamwise momentum equation yields:

$$0=-\frac{1}{\rho}\frac{\partial\langle\overline{p}\rangle}{\partial x}+\frac{\partial}{\partial y}\left(\nu\frac{\partial\langle\overline{u}\rangle}{\partial y}-\langle\tau_{12}\rangle-\langle u''v''\rangle\right). \tag{4.3}$$

Integrating Eq. (4.3) from $y = 0$ to y, and using the following boundary conditions at wall,

$$\nu\frac{\partial\langle\overline{u}\rangle}{\partial y}\bigg|_{y=0}=\frac{\tau_w}{\rho},\;\langle\tau_{12}\rangle\big|_{y=0}=0\,,\;\langle u''v''\rangle\big|_{y=0}=0\,, \tag{4.4}$$

yields

$$\frac{y}{\rho}\frac{\partial\langle\overline{p}\rangle}{\partial x}=\nu\frac{\partial\langle\overline{u}\rangle}{\partial y}-\langle\tau_{12}\rangle-\langle u''v''\rangle-\frac{\tau_w}{\rho}\,. \tag{4.5}$$

Applying the symmetry boundary condition at $y = \delta$ (i.e., at the center plane of the channel) to Eq. (4.5) gives the mean pressure gradient along the streamwise direction:

$$\frac{\partial \langle \overline{p} \rangle}{\partial x} = -\frac{\tau_w}{\delta}. \tag{4.6}$$

Eq. (4.6) shows that the mean pressure gradient in the channel flow is balanced by the wall shear stresses at the channel walls. Substituting Eq. (4.6) into Eq. (4.5) and using the relationship $\tau_w \equiv \rho u_\tau^2$ yields:

$$u_\tau^2 \left(1 - \frac{y}{\delta}\right) = \nu \frac{\partial \langle \overline{u} \rangle}{\partial y} - \langle \tau_{12} \rangle - \langle u'' v'' \rangle. \tag{4.7}$$

The modeled turbulent shear stress can be expressed using the eddy viscosity concept:

$$-\langle \tau_{12} \rangle = \left\langle \nu_T \frac{\partial \overline{u}}{\partial y} \right\rangle \approx \langle \nu_T \rangle \frac{\partial \langle \overline{u} \rangle}{\partial y}, \tag{4.8}$$

where $\nu_T = \nu_t$, ν_t^{SGS} or ν_t^{PRNS} depending on the simulation approach used. Substituting Eq. (4.8) into Eq. (4.7) and rearranging gives

$$\frac{\partial \langle \overline{u} \rangle}{\partial y} \approx \frac{u_\tau^2 \left(1 - y/\delta\right) - \langle -u'' v'' \rangle}{\nu + \langle \nu_T \rangle}. \tag{4.9}$$

Eq. (4.9) shows that the mean velocity gradient for a fully-developed plane channel flow is related to the resolved turbulent shear stress and the eddy viscosity.

4.3.2 Mean Streamwise Velocity

Figure 4.3 shows the mean streamwise velocity profiles, expressed in wall units in terms of u^+ and y^+ defined in Eq. (3.11). In general, the URANS predictions of the mean streamwise velocity are in good agreement with the DNS data. However, the PRNS and LES results exhibit a velocity shift, which starts at the second node from the wall. It should be noted that this shift in the mean velocity profile

has been observed in various flow simulation approaches, including LES with wall models (e.g., Cabot and Moin, 1999; Benarafa et al., 2006), zonal hybrid RANS/LES (e.g., Tucker and Davidson, 2004; Temmerman et al., 2005; Larsson et al., 2007) and DES (e.g., Nikitin et al., 2000; Piomelli et al., 2003). Larsson et al. (2007) concluded that the velocity shift is a robust feature of hybrid RANS/LES, and that this feature is relatively insensitive to the modeling interface locations or the specific turbulence models used. The primary cause of this velocity shift is the generation of an artificial buffer layer that develops at a location between the near-wall and outer regions of the flow, where the simulation experiences a transition from a region where the turbulence is largely modeled to one where it is largely resolved. A remedy to circumvent this problem is to introduce forcing (added as a source term to the momentum equation) to increase the resolved turbulence in the vicinity of interface. The forcing can be obtained from turbulent fluctuations synthesized using stochastic models (Batten et al., 2004; Davidson and Billson, 2006) or extracted from a reference DNS or LES database of a fully-developed channel flow (Davidson and Dahlstrom, 2005; Larsson et al., 2007). These studies showed that forcing increased the resolved shear stress in the LES region near the interface, with the result that the velocity shift was effectively reduced.

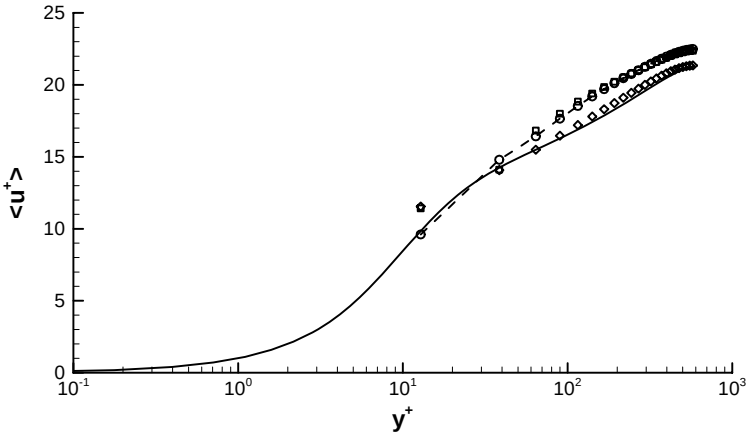

Figure 4.3. Mean velocity profiles. (—) DNS data of Moser et al. (1999); (◊) URANS; (○) PRNS; (□) LES.

Eq. (4.9) suggests that the velocity gradient is related to the resolved shear stress and the eddy viscosity. The velocity gradient for URANS depends mainly on the eddy viscosity since $\langle u''v'' \rangle \approx 0$, and the good conformance of mean velocity profile predicted by URANS indicates that the eddy viscosity for URANS was accurately predicted. Figure 4.4 displays profiles of the eddy viscosity (normalized by the molecular viscosity). Since the eddy viscosity is related to the modeled

turbulence, the magnitude of the eddy viscosity for URANS is the greatest among the three simulations because turbulence in URANS is mostly modeled. In contrast, the SGS eddy viscosity for LES has the smallest value because only the small scales of turbulence (which are not resolved in the simulation) are modeled here. The maximum value of SGS eddy viscosity occurs at the first near-wall node, and it gradually decreases away from the wall. Because the length scale of the energy-containing eddies decreases towards the wall, the grid resolution at the first node is too coarse to resolve most of the dynamically important small scales here. In consequence, this results in a large value of the SGS eddy viscosity here because the effects of the small scales of motion are modeled using wall functions. Away from the wall at $y/\delta > 0.25$, the value of SGS eddy viscosity becomes very small, implying that the turbulence is mostly resolved. The subscale eddy viscosity for PRNS has a value between that for URANS and LES. This suggests that PRNS depends much less on the modeling of the turbulence than URANS, but also resolves a smaller portion of the turbulence than LES.

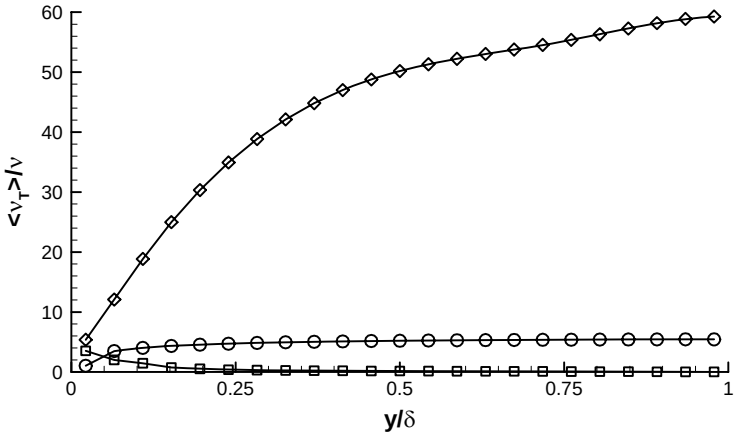

Figure 4.4. Mean eddy viscosity profiles. (◊) URANS; (○) PRNS; (□) LES.

The velocity gradient for PRNS and LES, as determined by the first few nodes from the wall shown in Figure 4.3, is too large in comparison with the DNS solution. Owing to the coarse grid resolution used in the near-wall region (in the sense that the grid size is large compared to the dynamically important small eddies here), the resolved turbulent shear stress at the first few nodes above the wall in PRNS and LES is under-predicted (cf. Figure 4.5), yielding a steeper velocity gradient at these nodes because the value of numerator on the right-hand-side of Eq. (4.9) is over-predicted. In the core region of the plane channel (at $y/\delta > 0.25$) where the turbulence is mostly resolved, the velocity profiles of PRNS and LES in this region have approximately the same slope as the DNS result (cf.

Figure 4.3), except that the values of the $\langle u^+ \rangle$-intercept [i.e., B in Eq. (3.10)] as predicted by PRNS and LES are larger than that obtained with DNS due to the velocity shift.

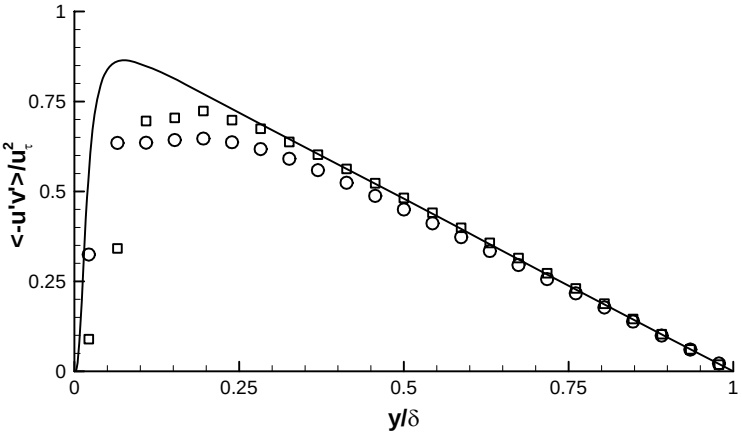

Figure 4.5. Reynolds shear stress profiles. (—) DNS data of Moser et al. (1999); (○) PRNS; (□) LES.

4.3.3 Root-Mean-Square Velocities

Predictions of the root-mean-square (rms) velocity ($u'_{i,rms} \equiv \sqrt{\langle \overline{u'_i u'_i} \rangle}$, with no implied summation on the repeated index i) profiles provided by URANS, PRNS and LES, are compared with the DNS results in Figure 4.6. While DNS shows strong anisotropic rms velocities (with $u'_{rms} > w'_{rms} > v'_{rms}$), the predictions provided by URANS give isotropic rms velocities (i.e., $u'_{i,rms} = \sqrt{2k/3}$) owing to the use of the linear Boussinesq stress-strain relationship [cf. Eq. (2.8)] in which $\overline{S}_{11} = \overline{S}_{22} = \overline{S}_{33} = 0$ for the fully-developed channel flow. LES provides improved predictions of the near-wall anisotropic rms velocities compared to URANS, and the shape of the rms velocities predicted by LES generally agrees well with DNS for $y/\delta > 0.25$. However, LES over-estimates u'_{rms} and under-estimates v'_{rms} and w'_{rms}, particularly in the region $y/\delta < 0.25$ where the largest discrepancies in comparison to the DNS data occur. In addition, the location and magnitude of the peak u'_{rms} is incorrect. These problems (known to occur for LES with wall models) have also been reported by Cabot and Moin (1999) and Benarafa et al. (2006). PRNS provides predictions of v'_{rms} and w'_{rms} that conform reasonably well to the DNS results. As in the case of LES, PRNS over-estimates u'_{rms} and provides an incorrect location for the peak of u'_{rms}.

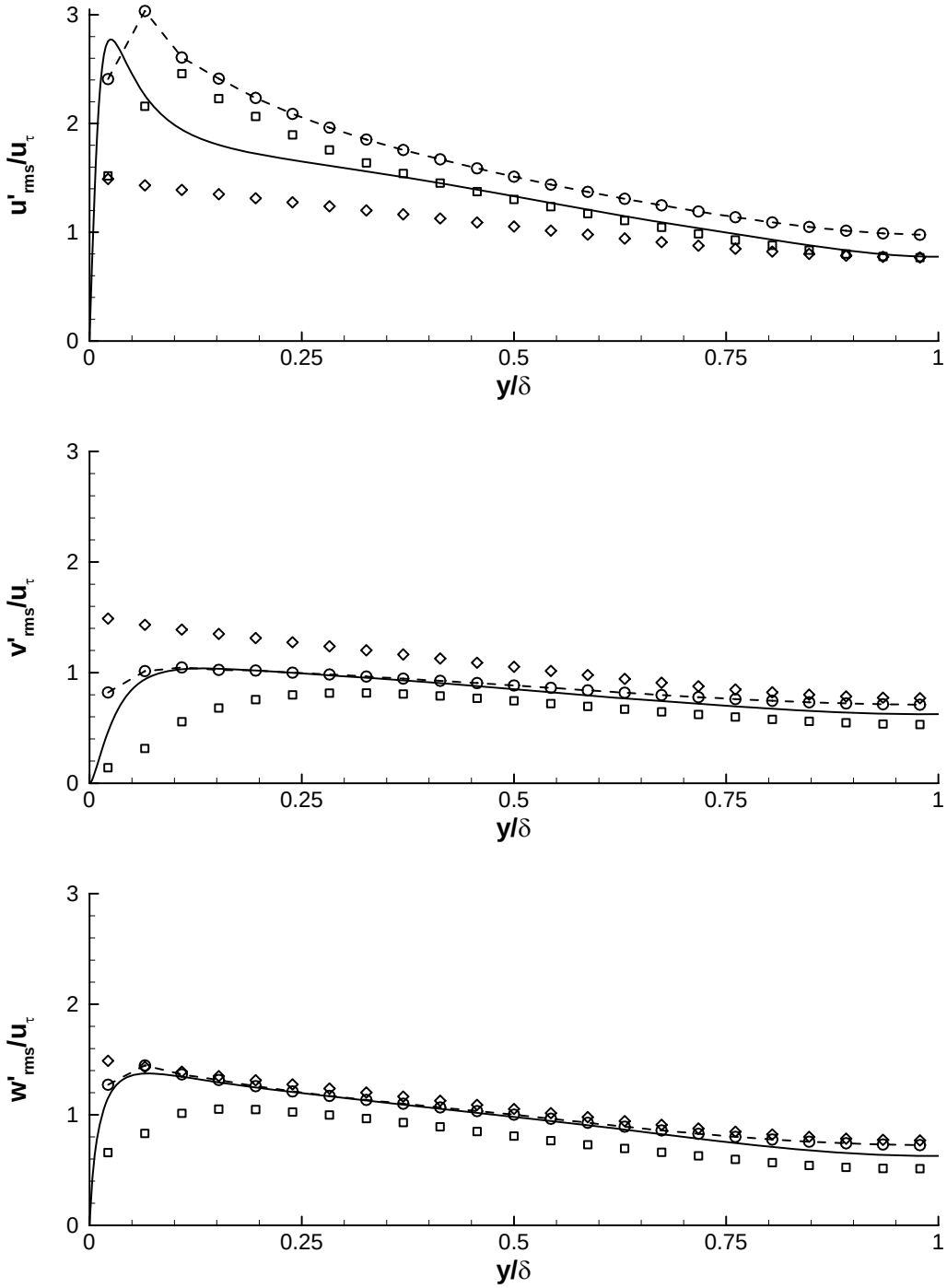

Figure 4.6. Root-mean-square velocity profiles. (—) DNS data of Moser et al. (1999); (◊) URANS; (○) PRNS; (□) LES.

Figure 4.6 shows that the location of the maximum u'_{rms} occurs at $y^+ \approx 14$ (or $y/\delta \approx 0.024$) in the DNS results. Similarly, the peak turbulence energy production occurs at $y^+ \approx 11$ based on the DNS data. This shows that vigorous turbulent activity mainly occurs within the physical buffer layer ($5 < y^+ < 30$). Because the near-wall eddies are responsible for a major portion of the turbulence energy production, these small scales of motion must be well resolved in order to provide accurate results. Using a computational grid that is too coarse to resolve these eddies generally results in poor predictions of the rms velocities. In addition, any simulation that uses wall functions is unable to capture the correct location of the peak u'_{rms} which occurs within the buffer layer, since the first near-wall node used in the wall functions approach is placed (ideally) at $y^+ > 30$ outside the buffer layer.

4.3.4 Resolution Control Function

The distribution of F_R is shown in Figure 4.7. It is seen that the value of F_R varies across the channel, decreasing gradually away from the wall. A smaller value of F_R implies that a greater fraction of the scales of turbulence is resolved. It can be seen from Figure 4.5 that a significant portion of the turbulent shear stress in PRNS is resolved in the core region of the plane channel.

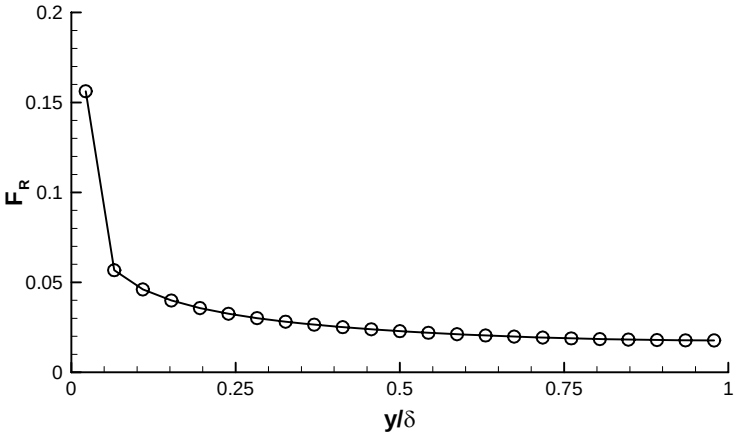

Figure 4.7. Resolution control function profile.

If the first grid node from the wall lies within the log-law layer, an analytical value of F_R at this node can be estimated using the log-law relationship for k and ε described in Eq. (3.12). The length scales required for the calculation of F_R in Eq. (2.27) can be obtained from Eqs. (2.31) and (2.32), which give the following results:

$$\left(l_i, l_c, l_\kappa\right) = \left[C_\kappa\, k^{3/2}/\varepsilon,\, 2\left(\Delta x \Delta y \Delta z\right)^{1/3},\, \left(\nu^3/\varepsilon\right)^{1/4}\right], \tag{4.10}$$

Substituting Eq. (3.12) into Eq. (4.10) yields

$$\left(l_i, l_c, l_\kappa\right) = \left[C_\kappa \kappa_v C_\mu^{-3/4} y_P,\, 2\left(\Delta x \Delta y \Delta z\right)^{1/3},\, \kappa_v^{1/4} y_P^{1/4}\, \mathrm{Re}_\tau^{-3/4}\, \delta^{3/4}\right], \tag{4.11}$$

where $y_P = 0.5\Delta y$ is the normal distance of the wall from the first near-wall node. The grid spacing in the three coordinate directions is determined as

$$\left(\Delta x, \Delta y, \Delta z\right) = \left(L_x/N_x, L_y/N_y, L_z/N_z\right), \tag{4.12}$$

where $(L_x, L_y, L_z) = (2\pi\delta,\, 2\delta,\, \pi\delta)$ and $(N_x, N_y, N_z) = (48, 48, 48)$ were described in Sections 4.1 and 4.2, respectively. With the values of $\kappa_v = 0.41$, $C_\kappa = 40$ and $\mathrm{Re}_\tau = 590$, $F_R \approx 0.16$ is obtained from Eq. (2.27), using the values for the various wave numbers, length scales, and grid spacings calculated from Eqs. (2.28), (4.11) and (4.12). This analytical value of F_R is consistent with the computed value at the first node from the wall shown in Figure 4.7. Similarly, a lower bound value of C_κ can be obtained by setting $l_c = l_i$ in Eq. (4.11) [which yields $F_R = 1$ in Eq. (2.27)]. This leads to

$$C_\kappa^{\min} = \frac{4\left(\Delta x \Delta y \Delta z\right)^{1/3} C_\mu^{3/4}}{\kappa_v \Delta y} \approx 2.67\,. \tag{4.13}$$

However, this value for $C_\kappa^{\min}$ yielded a subscale eddy viscosity (i.e., $\nu_t^{PRNS} = F_R \nu_t$) that was too large and hence too dissipative, resulting in the damping of all the turbulent velocity fluctuations in the channel flow at $\mathrm{Re}_\tau = 590$. It was found from the preliminary calculations that when the value of C_κ was increased to approximately 40, the excessive damping of the large-scale turbulent fluctuations in the flow did not occur and PRNS behaved like LES in this case.

It was mentioned in Section 2.4 that the quantities k and ε in PRNS are obtained from the same turbulence model as used in RANS, except that the time-filtered advection velocity $\overline{u}_i$ calculated from the filtered PRNS momentum equation is used in the k-ε model. It was further stated that in order to be consistent with the original k-ε model, the turbulence energy production term P_k

($= 2\nu_t \overline{S}_{ij}\overline{S}_{ij}$) in the PRNS approach should be computed using ν_t, rather than ν_t^{PRNS} ($= F_R \nu_t$). Figure 4.7 shows that the value of F_R is quite small. If ν_t^{PRNS} is used in the P_k term rather than ν_t, the use of the conventional closure constants for the k-ε model may no longer be appropriate, owing to the substantial reduction of P_k value arising from the small value of F_R [viz., $P_k = 2\left(F_R \nu_t\right)\overline{S}_{ij}\overline{S}_{ij}$]. Figure 4.8 displays the integral length scales of turbulence predicted by both PRNS (with C_κ = 40) and URANS using the k-ε turbulence model with its original closure constants. It is seen that the ratio of integral turbulence length scales of PRNS to URANS is of order unity. This suggests that the use of the original closure constants in the PRNS-based k-ε model is appropriate.

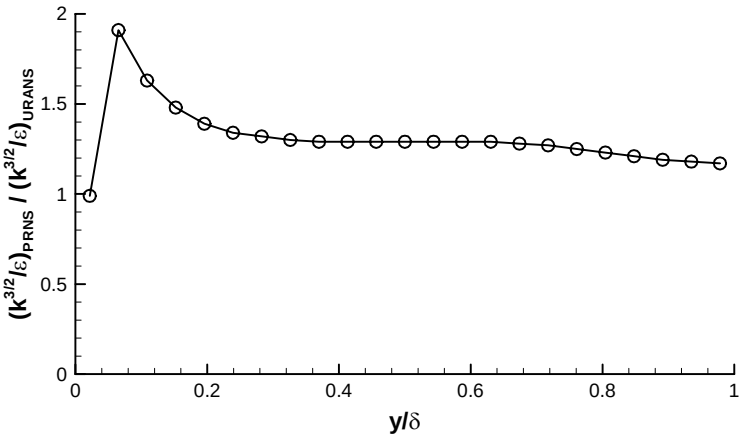

Figure 4.8. Ratio of integral length scale between PRNS and URANS.

4.4 Closure

The dependence of the flow solutions on grid resolution was investigated. It was found that a grid independent solution could be obtained using URANS, whereas the PRNS and LES solutions were sensitive to the grid resolution.

The URANS predictions for the streamwise mean velocity agreed well with the DNS data, whereas the PRNS and LES predictions exhibited a velocity shift. However, the PRNS and LES predictions were able to capture the near-wall anisotropy in terms of the rms velocities. In contrast, the URANS predictions gave wrong (isotropic) rms velocities. The performance of PRNS was similar to LES in terms of the predictions of the streamwise mean and rms velocities. Finally, PRNS gave the best overall conformance with the v'_{rms} and w'_{rms} profiles.

Chapter 5

Fully-Developed Flow over a Matrix of Cubes

Flow over bluff bodies is encountered in many engineering applications. A typical example is atmospheric flow over clusters of buildings. In this situation, a configuration consisting of a matrix of cubes (resembling a group of idealized buildings with simple geometry) is widely used to study the physical processes that occur around the buildings. Flow over a matrix of cubes is characterized by various flow phenomena, including impingement, separation and reattachment. The complex nature of this flow is dominated by unsteady large-scale turbulent structures. The interaction of the flow with the cubes makes the flow structures in this application distinctively different from the attached flow in a plane channel.

Fully-developed flow over a matrix of cubes immersed in a plane channel flow, for which periodic boundary conditions can be applied in both the streamwise and spanwise directions, is a useful test case for the validation of numerical simulation for complex flows. The experiment conducted by Meinders and Hanjalic (1999), which was used as one of the benchmark problems in the 6^{th} to 8^{th} European Research Community on Flow, Turbulence and Combustion (ERCOFTAC) workshops on turbulence modeling (Hanjalic and Obi, 1997; Craft, 1998; Hellsten and Rautaheimo, 1999), will be used as the reference test case in this chapter in order to assess the predictive performance of PRNS.

5.1 Problem Description

The wind-tunnel experiment of Meinders and Hanjalic (1999) involved the measurement of the flow in an extensive array of 250 cubes (25 rows of 10 cubes) placed in a plane channel. Velocity measurements were made around the 18^{th} row in the array of cubes from the inlet, near the centerline of the plane channel. The flow at this location was fully developed (viz., at this location, the

longitudinal modulations in the flow statistics from one cube canyon to the next have reached streamwise equilibrium). Figure 5.1 shows the geometry of the cubical array. The heights of a cube and the channel were H and $3.4H$, respectively. The separation between cubes (face-to-face) in both the streamwise and spanwise directions was $3H$. The Reynolds number, based on the cube height and the mean bulk velocity (U_b) in the plane channel, was 3854. The experimental uncertainty was estimated to be within 5% for the mean velocities and 10% for the Reynolds stresses.

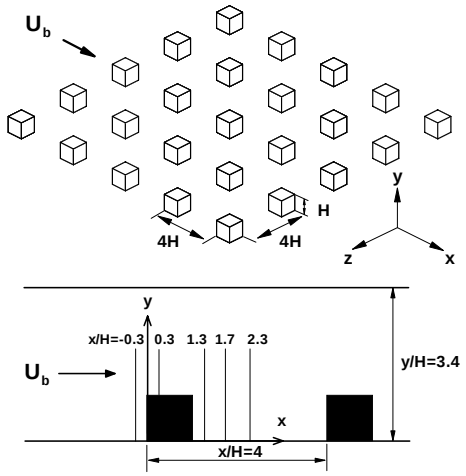

Figure 5.1. The geometry of an array of cubes and a side view of a sub-channel unit cell showing the locations of the velocity measurements.

5.2 Computational Aspects

Because of spatial periodicity in the flow within the matrix of cubes, the flow within a sub-channel unit cell (shown in Figure 5.1) only needs to be calculated (as this flow is representative of the flow in every other unit cell). The unit cell had dimensions of $4H \times 3.4H \times 4H$ in the streamwise (x), wall-normal (y) and spanwise (z) directions, respectively. Periodic boundary conditions were applied in both the streamwise and spanwise directions, and wall functions were used at the channel walls and cube faces.

Two different grids of $39 \times 39 \times 39$ nodes (coarse grid) and $49 \times 49 \times 49$ nodes (fine grid) were used in the numerical simulations to investigate the sensitivity of the flow solution to the grid resolution. The computational domain for the fine grid is shown in Figure 5.2. A temporal resolution of $\Delta t U_b/H \approx 0.032$ and 0.025 was used for the coarse and fine grids, respectively. The time step sizes were chosen

to ensure that CFL ≤ 1 [cf. Eq. (2.30)] over the entire computational domain for the given grid sizes. After the flow reached a statistically steady state, results for the coarse and fine grids were time-averaged over 40000 and 50000 time steps, respectively, to ensure that time-averaged quantities satisfied statistical convergence.

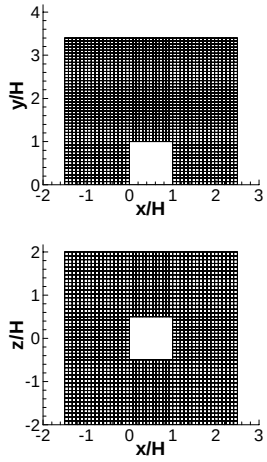

Figure 5.2. A two-dimensional *x*-*y* view at *z* = 0 (top) and *x*-*z* view at *y* = 0 (bottom) of the computational mesh of 49 × 49 × 49 nodes for a sub-channel unit cell.

Figure 5.3 shows an example of the prediction of the vertical profiles of streamwise mean velocity and Reynolds normal stress in the $z/H = 0$ plane obtained with the coarse and fine grids at the streamwise location $x/H = 0.3$. There is little difference in the predicted results between the coarse- and fine-grid URANS solutions, suggesting that grid independent solution has been achieved in the URANS predictions with the fine grid. In contrast, the PRNS and LES solutions are more sensitive to the grid resolution. When the grid is refined, the PRNS and LES predictions of the mean streamwise velocity near the upper channel wall (at $y/H = 3.4$) and the cube rooftop (at $y/H = 1$) are improved. The coarse- and fine-grid PRNS solutions over-predict the streamwise Reynolds normal stress in the core region ($y/H > 1$). Nevertheless, the fine-grid PRNS solution gives a better agreement with the experimental data. Similarly, the peak value of the streamwise Reynolds normal stress in the LES solution at $y/H \approx 1$ is better predicted when the fine grid is used.

In the next section, only the results generated from the fine grid are presented. Note that the current fine grid size of 49^3 (= 117,649) nodes is very comparable to the grid sizes used in the LES study of Cheng et al. (2003) and in the DES study of Schmidt and Thiele (2002). The latter two studies used 48^3 and roughly 120,000 nodes, respectively.

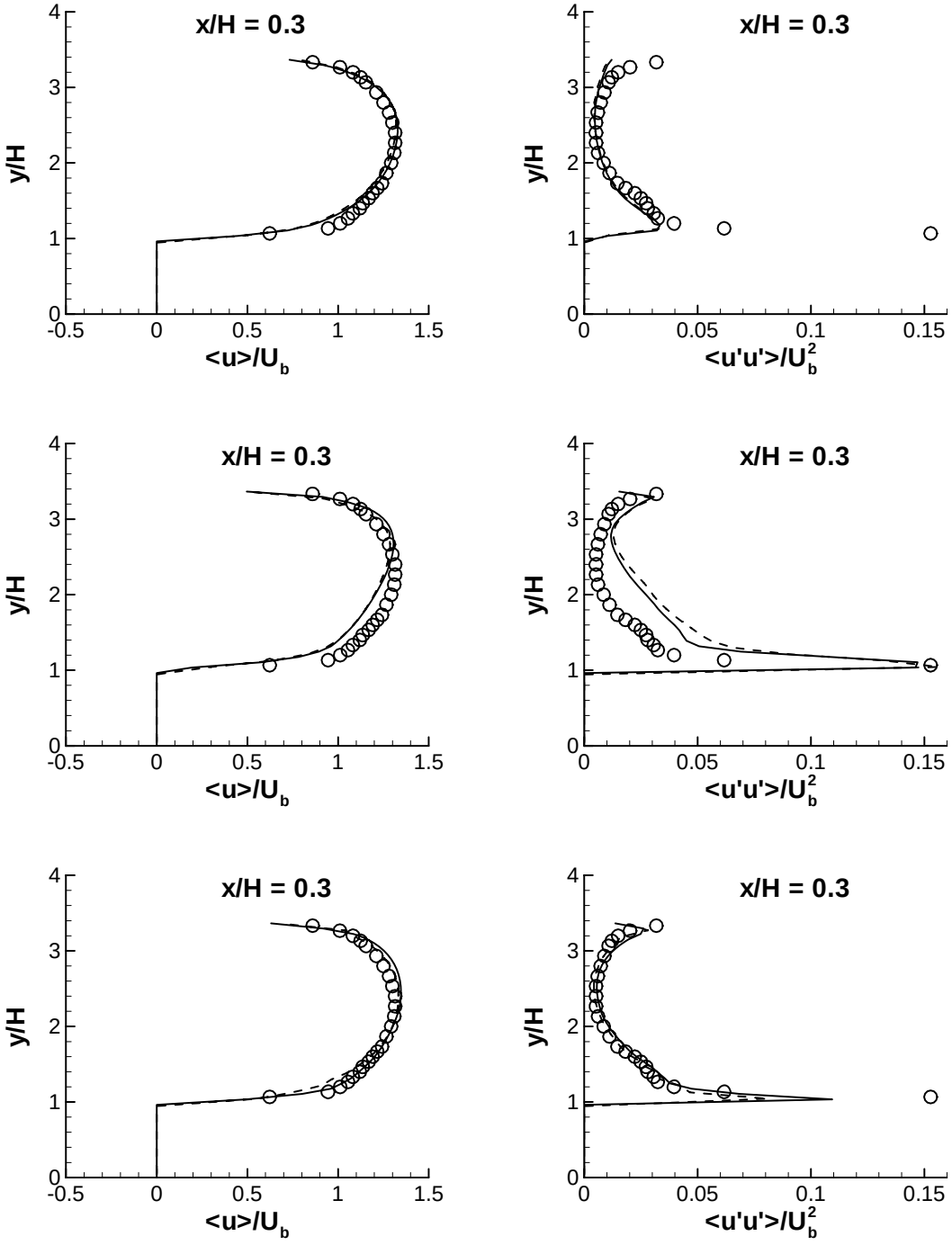

Figure 5.3. Grid sensitivity analysis: profiles of the streamwise mean velocity and Reynolds normal stress in the vertical *x*-*y* plane at *z*/*H* = 0 obtained at the streamwise location *x*/*H* = 0.3 using URANS (top), PRNS (middle) and LES (bottom). (○) Experimental data of Meinders and Hanjalic (1999); (– –) coarse grid (39 × 39 × 39); (—) fine grid (49 × 49 × 49).

5.3 Results and Discussion

Predicted results for the mean streamwise velocity and Reynolds normal stresses from the simulations were compared with the experimental data at four selected locations (namely, at $x/H = -0.3$, 0.3, 1.3 and 1.7) displayed in Figure 5.1.

5.3.1 Mean Velocity

The mean velocity vector fields in the vertical x-y plane at $z/H = 0$ and the horizontal x-z plane at $y/H = 0.5$, predicted using URANS, PRNS and LES, are shown in Figure 5.4 and Figure 5.5, respectively. It can be seen from these two figures that all the approaches exhibit similar flow structures. Figure 5.4 shows that the flow in the core region above the cube ($y/H > 1$) is mostly undisturbed, except close to the cube where the flow separates at the sharp leading top edge of the cube. Two main vortex structures are identified in the proximity of the cube: a downward vortex near the windward face of the cube, and an upward arch vortex in the wake of the cube.

According to the experimental observations, the flow in the cube canyon is characterized by this two-cell vortex structure separated by the flow reattachment at the channel floor, which occurred at $x/H \approx 2.5$ (or at $1.5H$ downstream from the leeward face of the cube). These two vortices are visible in the simulations and are seen to separate from each other at $x/H \approx 2.5$ in the PRNS and LES solutions. These predicted flow features are consistent with the experimental findings. In contrast, the separation of these two vortices occurs at $x/H \approx -1.3$ (or at $1.7H$ downstream from the leeward face of the cube) in the URANS solution. This indicates that URANS over-estimates the extent of the separation region behind the cube, yielding a slower rate of momentum recovery following the flow reattachment. Consequently, URANS under-predicts the mean streamwise velocity just upstream of the windward face of the cube, e.g., at location $x/H = -0.3$ for $y/H < 1$ [cf. Figure 5.6(a)].

In their LES study, Niceno et al. (2002) observed stagnation points (caused by the flow impingement) at $y/H \approx 0.8$ and $y/H \approx 0.25$ on the windward and leeward faces of the cube, respectively. Similar locations for stagnation points were found in the current study, except for URANS whose predictions do not exhibit a stagnation point on the leeward face of the cube. It can be seen in Figure 5.4 that the flow predicted by URANS exhibits only upward velocities along the leeward face of the cube, which

contrasts sharply with the PRNS and LES results where the flow is seen to exhibit downward velocities below the stagnation point at $y/H \approx 0.3$.

Figure 5.5 demonstrates that the mean flow is symmetrical along the centerline at $z/H = 0$, and that the flow separates at the sharp leading side edges of the cube. A pair of counter-rotating vortices in the wake region is evident. The center of these vortices for URANS is located at $x/H \approx 1.4$, in contrast with those for PRNS and LES where the center of the vortices are seen to be located at $x/H \approx 1.7$. Similar positions of the vortex cores were found in the study of Cheng et al. (2003), where the center of the vortices in their RANS and LES predictions were located at $x/H \approx 1.4$ and 1.6, respectively. The corresponding center of the vortices in the experiment was located at $x/H \approx 1.6$.

Figure 5.6(a) shows the mean streamwise velocity predictions in the vertical x-y plane at $z/H = 0$. While the mean velocity profiles obtained using the three approaches are generally similar, it is found that LES gives the best conformance with the experimental data. URANS agrees with the experimental measurements reasonably well for $y/H > 1$ where the flow is attached, but shows visible discrepancies in the recirculation zone ($y/H < 1$) within the cube canyon, where the flow exhibits reversals at the streamwise locations $x/H = -0.3$, 1.3 and 1.7. In particular, URANS significantly under-predicts the mean streamwise velocity at $x/H = -0.3$ near the windward face of the cube due to the over-prediction of the recirculation bubble in the wake region. The PRNS results provide slightly better predictions of the reverse flow within the recirculation zone than the LES results (e.g., see locations $x/H = -0.3$ and 1.3). However, PRNS under-predicts the mean velocity in the region $1 < y/H < 2.5$. Similar under-predictions of the velocity in this region were also found in the LES results reported by Niceno and Hanjalic (1999), where they used an unstructured grid with 418,760 cells.

Figure 5.6(b) displays the horizontal profiles of the mean streamwise velocity in the x-z plane at $y/H = 0.5$. Both PRNS and LES capture the correct shape of the mean streamwise velocity, but PRNS agrees slightly better with the experimental data than LES. In contrast, predictions from URANS provide erroneous predictions of the mean velocity in the spanwise corridor region between two cubes for $z/H > 0.5$. The predicted velocity in URANS increases monotonically in the region $0.5 < z/H < 2$, which is contradictory to the measured velocity where it is seen to increase for $0.5 < z/H < 1$ and then decrease for $1 < z/H < 2$. In addition, URANS significantly under-predicts the streamwise velocity for $0.5 < z/H < 1.5$. The under-prediction of the velocity here is associated with the under-prediction of the velocity just upstream of the windward face of the cube, resulting in a slower fluid passage around the

cube. Consequently, the velocity away from the cube must increase in order to maintain mass conservation, hence resulting in an over-prediction of the mean velocity in the region $1.5 < z/H < 2$.

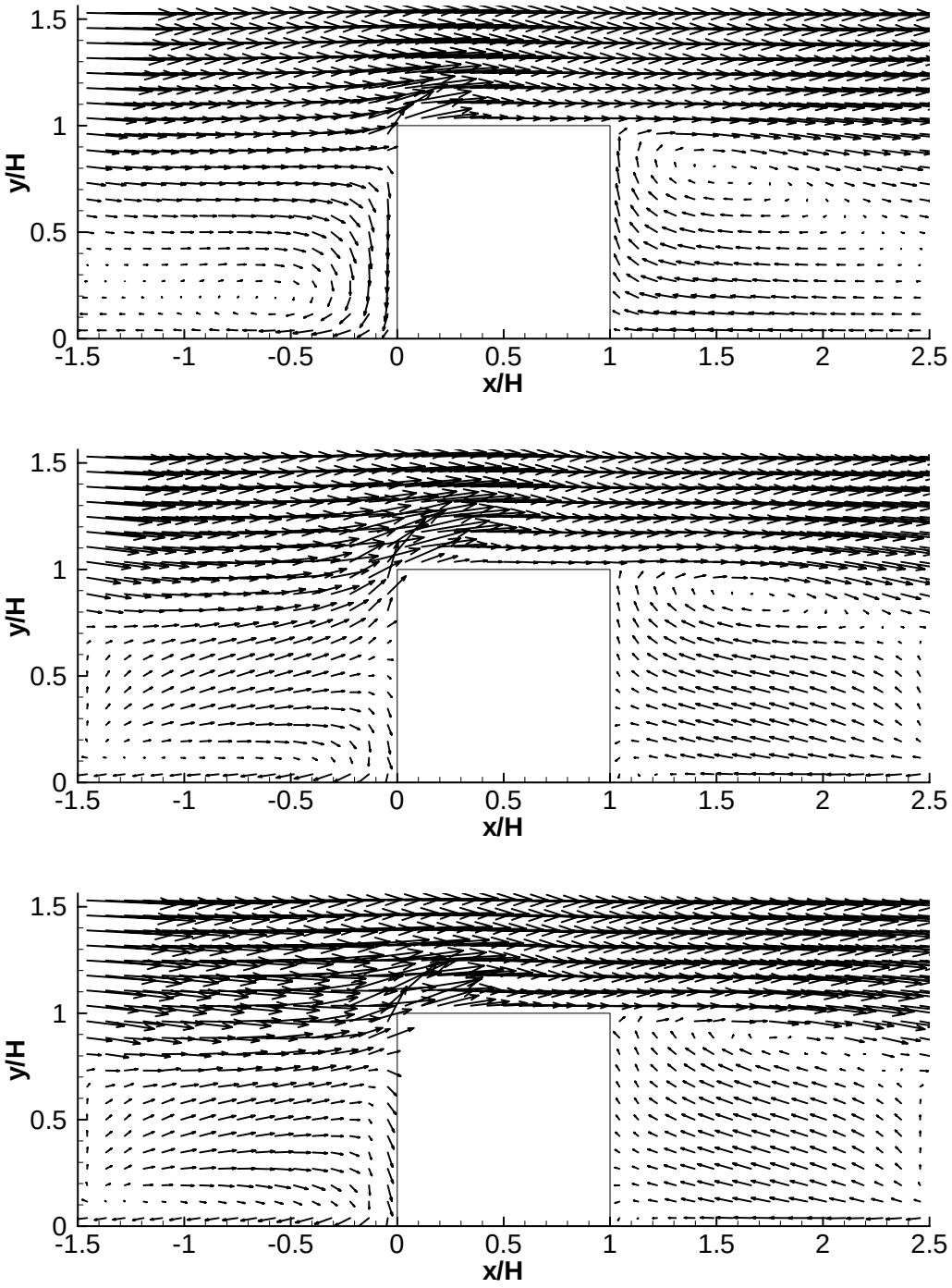

Figure 5.4. Mean velocity vector field in the vertical *x*-*y* plane at $z/H = 0$ obtained using URANS (top), PRNS (middle) and LES (bottom).

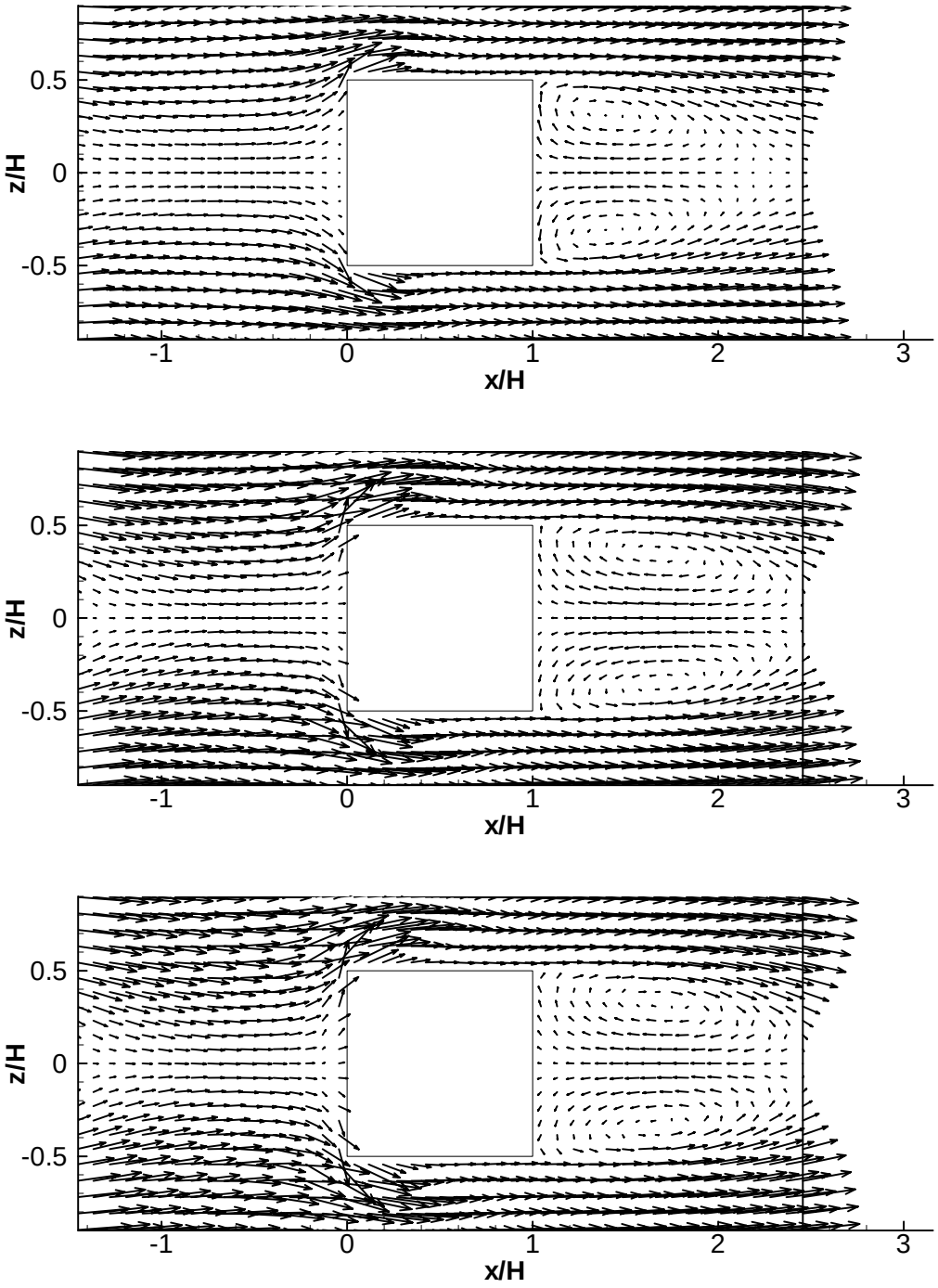

Figure 5.5. Mean velocity vector field in the horizontal *x*-*z* plane at *y*/*H* = 0.5 obtained using URANS (top), PRNS (middle) and LES (bottom).

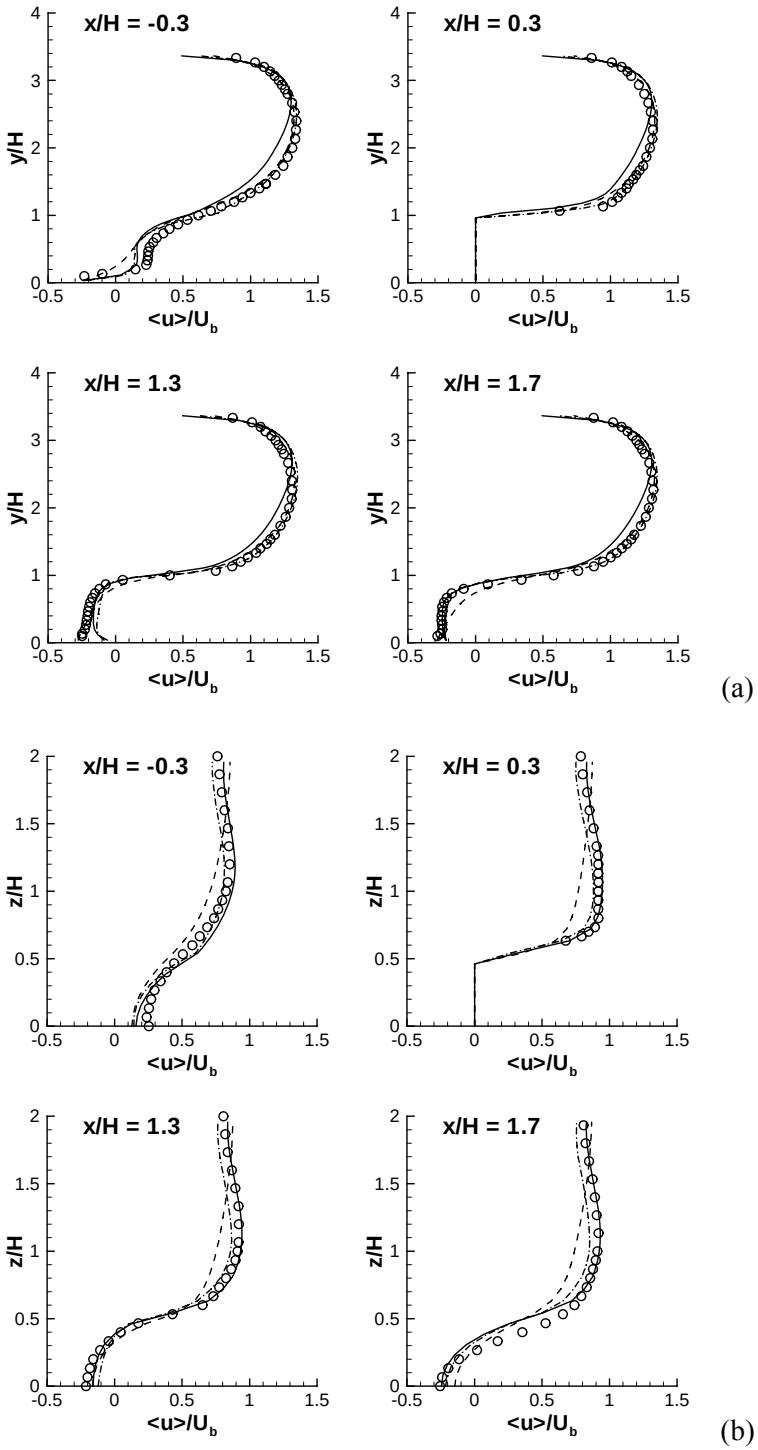

Figure 5.6. Profiles of the mean streamwise velocity in (a) the vertical *x*-*y* plane at *z*/*H* = 0 and (b) the horizontal *x*-*z* plane at *y*/*H* = 0.5. (○) Experimental data of Meinders and Hanjalic (1999); (– –) URANS; (—) PRNS; (– · –) LES.

5.3.2 Reynolds Stresses

A comparison of the measured and predicted streamwise Reynolds normal stresses $\overline{u'u'}$ is presented in Figure 5.7. It is observed that the peak value of $\overline{u'u'}$ at each x-location occurs at $y/H \approx 1$ in the vertical x-y plane at $z/H = 0$ and at $z/H \approx 0.5$ in the horizontal x-z plane at $y/H = 0.5$. These peaks in $\overline{u'u'}$ correspond to the development of the thin shear layers along the rooftop and side walls of the cube, respectively. These shear layers originate from the sharp leading edges of the cube, and result in strong velocity gradients that contribute to a significant production (generation) of $\overline{u'u'}$. Moreover, it is seen from Figures 5.4 and 5.5 that there are thin separation zones on the rooftop and side walls of the cube at $0 < x/H < 0.5$. Figure 5.7 reveals that the maximum value of $\overline{u'u'}$ ($\approx 0.15U_b^2$) is found at $x/H = 0.3$ (i.e., within the thin separation zone), where a large velocity gradient $\partial\overline{u}/\partial x$ is expected to occur due to the separation of the shear layer and its subsequent reattachment.

Figure 5.7(a) shows that the value of $\overline{u'u'}$ gradually decreases for $1 < y/H < 2.5$ as the impact of the cube on the flow starts to diminish, and increases again for $2.5 < y/H < 3.4$ because of the increasing velocity gradient $\partial\overline{u}/\partial y$ towards the upper channel wall as confirmed in Figure 5.6(a). Figure 5.7(b) shows that the value of $\overline{u'u'}$ slowly decreases for $0.5 < z/H < 1$, owing to the decreasing velocity gradient $\partial\overline{u}/\partial z$ in this region as seen in Figure 5.6(b).

In terms of the shape and magnitude of the $\overline{u'u'}$ profiles, the discrepancy between the URANS results and the experimental data is generally large, particularly within the recirculation zones for $y/H < 1$ [cf. Figure 5.7(a)] and for $z/H < 0.5$ [cf. Figure 5.7(b)]. Furthermore, URANS significantly under-estimates the peak value of $\overline{u'u'}$ by more than 50% at the streamwise locations $x/H = 0.3$, 1.3 and 1.7. This under-prediction of $\overline{u'u'}$ in URANS arises from the utilization of the linear Boussinesq stress-strain relationship [cf. Eq. (2.8)], which cannot properly account for the effects of anisotropy in the Reynolds stresses. In contrast, the LES results are in fairly good agreement with the experimental measurements in the $z/H = 0$ plane, but these predictions moderately under-predict the magnitude of $\overline{u'u'}$ in the $y/H = 0.5$ plane. The PRNS results give predictions for $\overline{u'u'}$ that are similar to those provided by the LES results, but PRNS is observed to over-estimate the magnitude of $\overline{u'u'}$ for $y/H > 1$ [cf. Figure 5.7(a)] and for $z/H > 0.5$ [cf. Figure 5.7(b)]. The over-prediction of $\overline{u'u'}$ in these regions

was also reported in the DES study of Schmidt and Thiele (2002), but their predictions of the values for $\overline{u'u'}$ were generally larger than the current PRNS predictions by at least a factor of two.

Profiles of the spanwise Reynolds normal stress $\overline{w'w'}$ are exhibited in Figure 5.8. It is seen from Figure 5.8(a) that the peak value of $\overline{w'w'}$ at each x-location occurs at $y/H \approx 1$ in the $z/H = 0$ plane, which is related to the thin intense shear layer developed along the rooftop of the cube. Large values of $\overline{w'w'}$ are also observed in the range $0.2 < y/H < 0.8$ at $x/H = -0.3$, which are associated with the flow impingement on the windward face of the cube. The URANS and LES results compare well with the measured data for $y/H > 1$, whereas PRNS over-predicts the magnitude of $\overline{w'w'}$ in this region. The shapes of the $\overline{w'w'}$ profiles for $y/H < 1$ are poorly represented by URANS, but are captured fairly well by PRNS and LES. However, both PRNS and LES considerably under-estimate the magnitude of $\overline{w'w'}$ for $y/H < 1$. The large discrepancy in the predictions of the values of $\overline{w'w'}$ at locations $x/H = -0.3$ and 1.7 was also reported by Mathey et al. (1999) and Cheng et al. (2003), where their numerical studies included LES with the standard Smagorinsky model and a dynamic SGS stress model. Both studies showed that LES with different SGS models gave very similar results, suggesting that SGS models are not the cause of the under-prediction of $\overline{w'w'}$ observed here. It is noted that Mathey et al. (1999) and Cheng et al. (2003) used a grid size of 100^3 and 48^3 nodes, respectively, clustered towards the channel walls and cube faces. It is suspected that the large discrepancy might be due to insufficient grid resolution.

Figure 5.8(b) shows that the URANS predictions for $\overline{w'w'}$ are generally poor in the x-z plane at $y/H = 0.5$. The predicted $\overline{w'w'}$ obtained from URANS decreases monotonically for $z/H > 0.5$, which is inconsistent to the measured $\overline{w'w'}$ where it is seen to increase for $z/H > 1$. In contrast, a good conformance of PRNS and LES solutions with the experimental results is obtained for $z/H > 0.5$. Nevertheless, PRNS shows slightly better performance than LES here. Moreover, the profile of $\overline{w'w'}$ at $x/H = -0.3$ for $z/H < 0.5$ was accurately captured by PRNS. However, it is seen that at location $x/H = 1.7$, both PRNS and LES significantly under-predict the magnitude of $\overline{w'w'}$ for $z/H < 0.5$. The poor prediction of $\overline{w'w'}$ here was also found in other related studies (e.g., Schmidt and Thiele, 2002; Cheng et al., 2003). This is possibly related to the insufficient grid resolution used in this region.

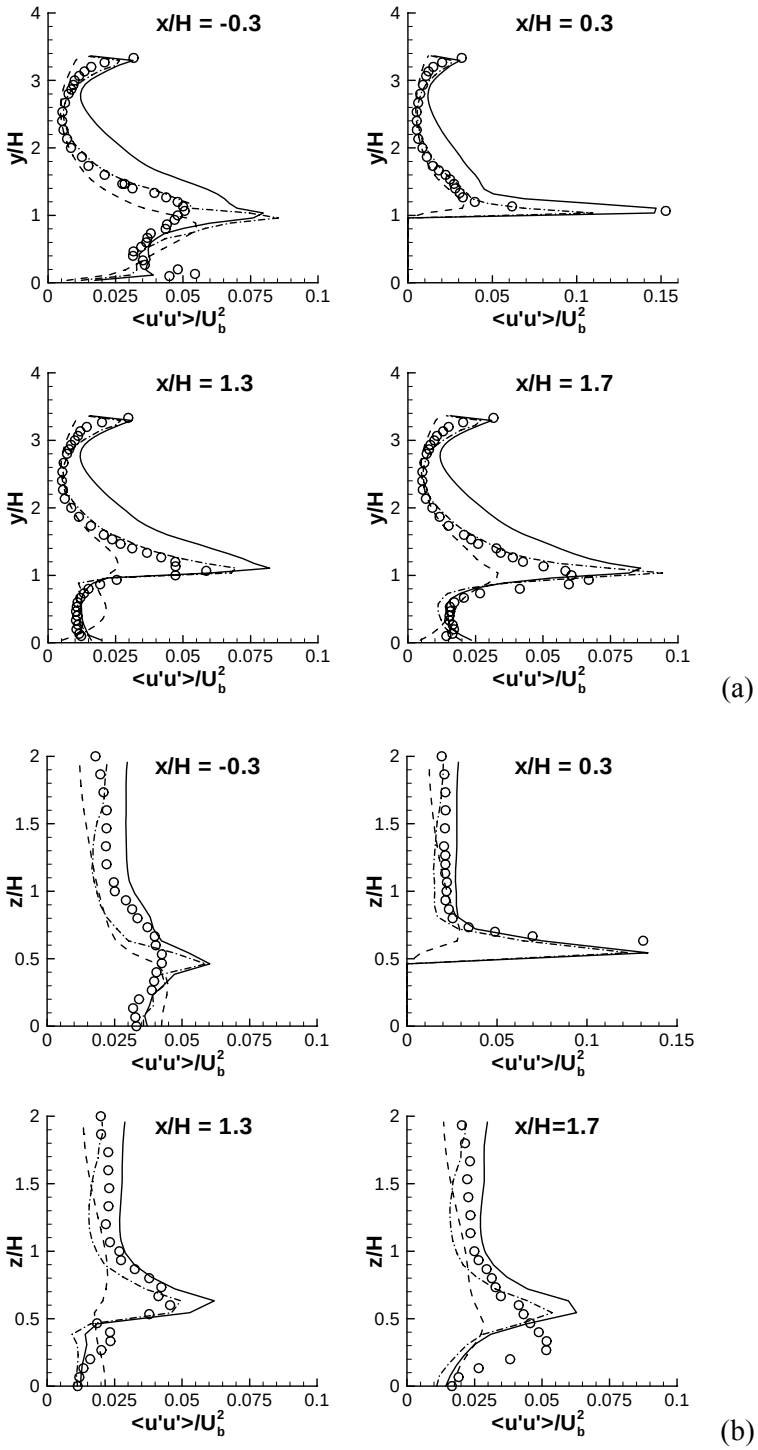

Figure 5.7. Profiles of streamwise Reynolds normal stress in (a) the vertical *x*-*y* plane at *z*/*H* = 0 and (b) the horizontal *x*-*z* plane at *y*/*H* = 0.5. (○) Experimental data of Meinders and Hanjalic (1999); (– –) URANS; (—) PRNS; (– · –) LES.

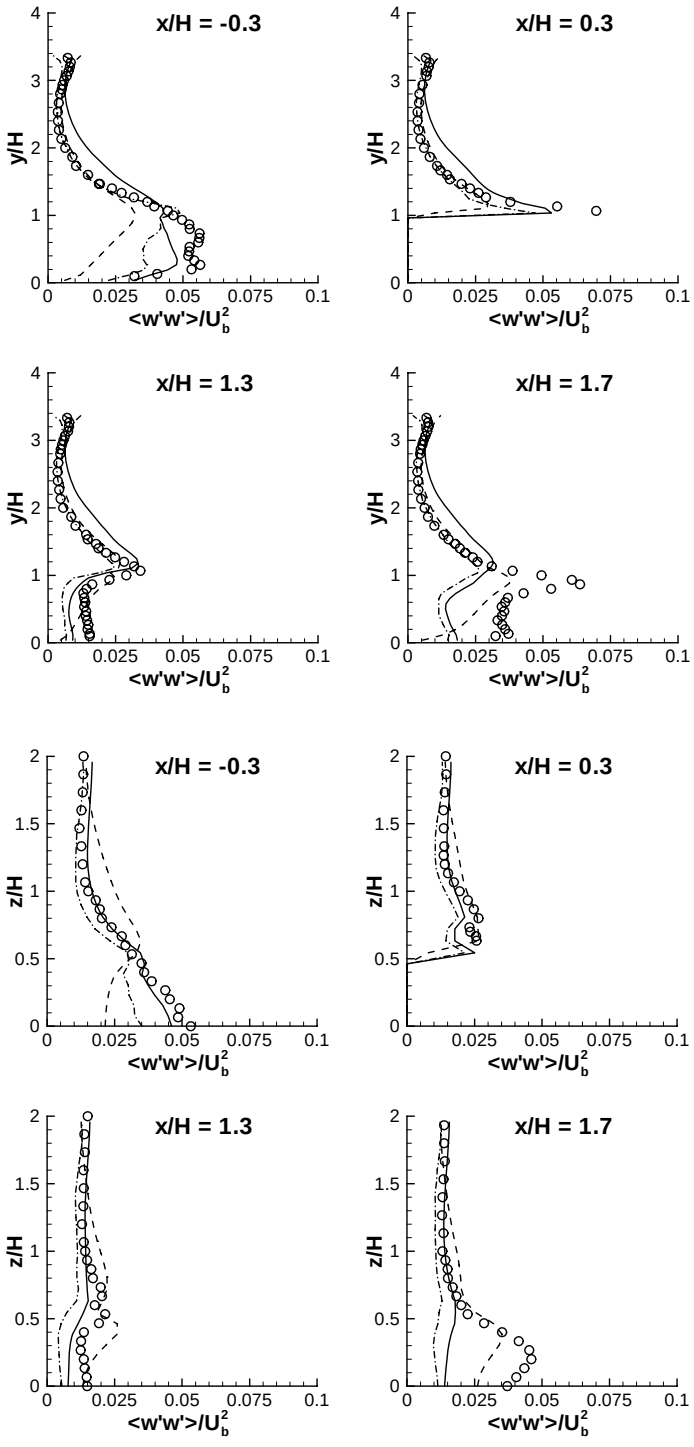

Figure 5.8. Profiles of spanwise Reynolds normal stress in (a) the vertical *x*-*y* plane at *z*/*H* = 0 and (b) the horizontal *x*-*z* plane at *y*/*H* = 0.5. (○) Experimental data of Meinders and Hanjalic (1999); (– –) URANS; (—) PRNS; (– · –) LES.

5.3.3 Resolution Control Function

Recall that the formulation of F_R [cf. Eq. (2.27)] in PRNS involves a closure constant C_κ [cf. Eq. (2.32)], where the value of $C_\kappa = 40$ was calibrated against some DNS data for a fully-developed channel flow as presented in Chapter 4. Based on the good agreement of PRNS predictions (in terms of the mean velocities and Reynolds stresses) with the measurements for a fully-developed flow over a matrix of cubes as shown in this chapter, this suggests that $C_\kappa = 40$ remains valid in a complex turbulent flow dominated by unsteady large-scale turbulent structures.

Figure 5.9 displays the distributions of F_R in the proximity of the cube in a vertical x-y plane at $z/H = 0$ and in a horizontal x-z plane at $y/H = 0.5$. The value of F_R varies across these planes, with higher value observed towards the walls, implying that more modeling is required here for the given grid resolution. It is seen that the contours of F_R are symmetrical along the centerline at $z/H = 0$ in the $y/H = 0.5$ plane, which is expected when the averaging time used to obtain flow statistics is long enough to provide statistically converged results.

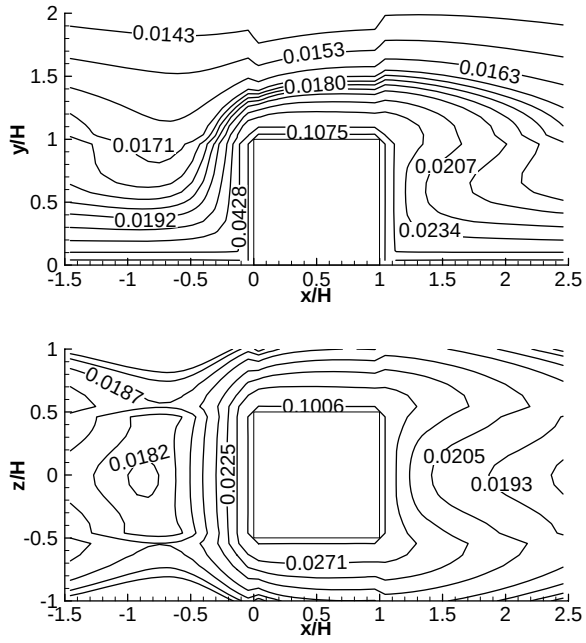

Figure 5.9. Contours of resolution control function in the x-y plane at $z/H = 0$ (top) and in the x-z plane at $y/H = 0.5$ (bottom).

5.4 Closure

Structures in the mean flow, such as an arch vortex and recirculation bubbles in the wake region of the cube, were captured by URANS, PRNS and LES reasonably well. However, the shape and size of the vortices in the vicinity of the cube predicted by URANS were different than those predicted by PRNS and LES. The URANS results generally gave a poor conformance with the experimental data, particularly within the recirculation zone on the lee side of the cube. In contrast, PRNS and LES provided good predictions for the mean velocities and Reynolds normal stresses, both in terms of the shapes of the profiles and of their magnitudes. In general, PRNS showed similar but slightly better performance than LES.

Chapter 6

Developing Flow over a Matrix of Obstacles

In comparison to the wall-bounded fully-developed flows studied earlier, simulation of developing flows raises more difficulties because they are highly sensitive to the imposed boundary conditions. In particular, specification of realistic unsteady inflow boundary conditions poses an additional challenge for PRNS and LES. Most of numerical studies for a developing flow over a group of obstacles were performed using RANS (e.g., Lien and Yee, 2004; Hsieh et al., 2007a) due to its relatively low computational cost. In addition, inflow conditions for mean flow properties in RANS were usually available from experimental measurements. In contrast, only a very limited number of LES studies of a developing flow through an obstacle array were conducted (e.g., Hanna et al., 2002; Shi et al., 2008), mainly because of the high computational cost and the difficulty to prescribe inflow conditions with a proper representation of turbulent fluctuations.

The numerical performance of PRNS for developing flow over a matrix of cubes will be compared to that of URANS and LES. For PRNS and LES calculations, unsteady inlet turbulent fluctuations will be prescribed using the simple method described in Section 3.2.3.

6.1 Problem Description

The test case considered here is the wind-tunnel experiment of Brown et al. (2001), which was conducted at the U.S. Environmental Protection Agency's (EPA) fluid modeling facility. The experiment consisted of the measurement of the flow through an extensive array of 77 cubes (7 rows of 11 cubes) placed in an open-return type wind tunnel. Figure 6.1 shows a schematic of the cubical array. The wind tunnel had a test section of 18.3 m length, 3.7 m width and 2.1 m height, and the ceiling of the test section was adjustable in height to allow for a non-accelerating free stream flow. A

neutral boundary layer with a depth of 1.8 m was created upstream of the cubical array. The height of a cube was H (= 0.15 m), and the separation between cubes (face-to-face) in both the streamwise and spanwise directions was H. The Reynolds number, based on the cube height and a reference velocity U_r (= 3 m/s) of the upstream flow at $y = H$, was 30000. The profiles of the mean velocities and the turbulence kinetic energy were measured in the vertical center plane of the array, extending from 3.3H upstream of the windward face of the first row of cubes to 7.5H downstream of the leeward face of the last row of cubes and to 3H above the ground.

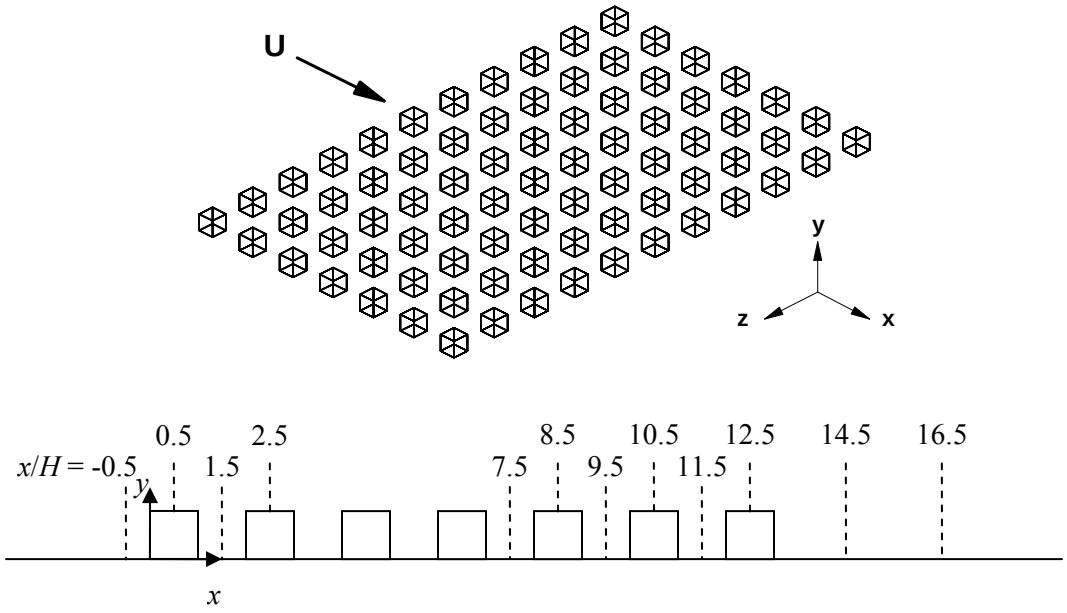

Figure 6.1. The geometry of an array of cubes and a side view showing the selected locations of the velocity measurements.

6.2 Computational Aspects

Figure 6.1 shows that the geometry of the array possesses a two-fold symmetry in the spanwise direction. In consequence, for the numerical simulation of the flow field, only one column of cubes was included in the computational domain. The extent of computational domain in the streamwise (x), wall-normal (y), and spanwise (z) directions was $-5 \le x/H \le 28$, $0 \le y/H \le 8$, and $-1 \le z/H \le 1$, respectively. The same domain size was used in the related RANS studies of Lien and Yee (2004) and Santiago et al. (2007). Lien and Yee (2004) also conducted simulations using a domain height of 10H and 12H, and reported that these domain heights had a negligible effect on the solution.

Computations from URANS, PRNS and LES were performed on a mesh of 135 × 40 × 31 nodes (in the x, y and z-directions) in a computational domain shown in Figure 6.2. The grid lines were preferentially concentrated near the solid surfaces (ground and cube faces) to better capture the expected sharp gradients of the flow properties here, and the spacing between grid lines was stretched with increasing distance from the solid surfaces. A temporal resolution of $\Delta t U_r/H = 0.05$ was used, and the time step size chosen satisfied CFL ≤ 1 [cf. Eq. (2.30)] over the entire computational domain for the given grid size.

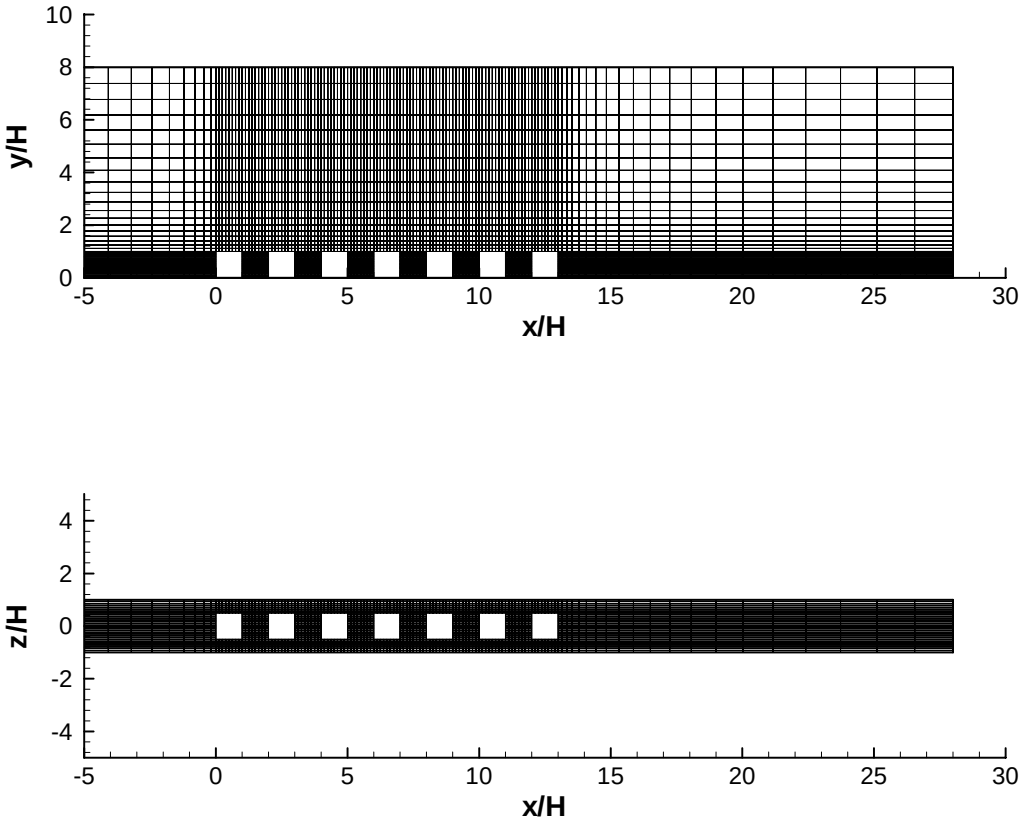

Figure 6.2. A two-dimensional *x*-*y* view at *z* = 0 (top) and *x*-*z* view at *y* = 0 (bottom) of the computational mesh of 135 × 40 × 31 nodes.

The time history of the three velocity components was monitored at the locations (x/H, y/H, z/H) = (8.5, 1.5, 0) and (9.5, 0.5, 0) to check if the flow approached a statistically steady state. The computations were first run from initial conditions for 5000 time steps, where it was found that the

flow reached a statistically steady state approximately after first 2000 time steps. The computations were subsequently run for another 10000 time steps to collect the statistics of the flow. Vertical profiles of the mean streamwise velocity and the turbulence kinetic energy (at the selected locations shown in Figure 6.1), obtained from time-averaging over the first half and the entire 10000 time steps, were compared to each other. It was found that the difference in the time-averaged results obtained over 5000 and 10000 time steps was small, suggesting that time-averaged flow quantities over 10000 time steps satisfied statistical convergence.

Periodic boundary conditions were applied in the spanwise direction, and wall functions were used at the ground and cube faces. At the upper boundary, free-slip conditions were imposed:

$$\frac{\partial \overline{u}}{\partial y} = 0\,,\ \overline{v} = 0\,,\ \overline{w} = 0\,,\ \frac{\partial k}{\partial y} = 0\,,\ \frac{\partial \varepsilon}{\partial y} = 0\,. \tag{6.1}$$

At the outlet, the flow was assumed to reach a fully-developed state:

$$\frac{\partial \overline{u}}{\partial x} = \frac{\partial \overline{v}}{\partial x} = \frac{\partial \overline{w}}{\partial x} = \frac{\partial k}{\partial x} = \frac{\partial \varepsilon}{\partial x} = 0\,. \tag{6.2}$$

At the inlet, the measured profiles of mean streamwise velocity and turbulence kinetic energy were used. The dissipation rate was not measured, and was estimated assuming that $\varepsilon_{in} = C_\mu^{3/4} k_{in}^{3/2} \big/ \left(\kappa_v y\right)$, where k_{in} is the turbulence kinetic energy at the inlet and κ_v (= 0.41) is the von Karman constant. The mean streamwise velocity at the inlet was approximated using the power-law profile:

$$\overline{u} = U_{in}\left(y\right) = U_r \left(y/H\right)^{0.13}\,. \tag{6.3}$$

In addition to the mean velocity profiles, unsteady inlet turbulent fluctuations are required for PRNS and LES calculations. Three different fluctuations, superimposed on the mean inlet velocity profiles, were investigated; namely, no fluctuations, random fluctuations (or, white noise), and time-correlated fluctuations described in Eq. (3.20):

$$u_i'\left(t\right) = u_i'\left(t - \Delta t\right) R\left(\Delta t\right) + r_i\left(t\right)\sigma_i \sqrt{1 - R^2\left(\Delta t\right)}\,. \tag{6.4}$$

Random fluctuations were prescribed using $u_i'(t) = r_i(t)\sigma_i$, obtained by setting the autocorrelation function $R(\Delta t) = 0$ in Eq. (6.4). For time-correlated fluctuations, $R(\Delta t) = \exp(-\Delta t/T_L)$ was used in Eq. (6.4), in which the integral time scale was calculated using $T_L = \kappa_v y/U_{in}(y)$ [cf. Eqs. (3.21) and (3.22)]. For both the random and time-correlated fluctuations, the value of the target standard deviation of u_i' (i.e., $\sigma_i = u_{i,rms}'$) was assumed as $\sigma_i = 0.6U_r$. This means that simple isotropic rms velocities (i.e., $u_{rms}' = v_{rms}' = w_{rms}' = 0.6U_r$) were assumed at the inlet.

It was found from the preliminary LES calculations (with the time-correlated fluctuations) that when $\sigma_i = 0.6U_r$, the predicted vertical profiles (in terms of the shape and magnitude) of the turbulence kinetic energy were in a reasonable good conformance with the experimental data for $1 \le y/H \le 3$ (cf. Figure 6.3, and Figures 6.10 to 6.12). If a lower value of σ_i (e.g., $\sigma_i = 0.3U_r$) was used, the predicted turbulence kinetic energy profiles had a similar shape, but lower magnitude (for $y/H > 1$), than those obtained using $\sigma_i = 0.6U_r$. In the region $y/H < 1$, where the influence of the cube on the flow within the street canyon is large, the magnitude of σ_i has negligible effect on the turbulence kinetic energy profiles. This can be seen in Figure 6.3, where the difference in the turbulence kinetic energy profiles obtained without fluctuations (i.e., $\sigma_i = 0$) and with random or time-correlated fluctuations (where $\sigma_i = 0.6U_r$) at the location $x/H = 7.5$ for $y/H < 1$ (below the top of the urban canopy), is very small.

The effect of the inlet fluctuations on the PRNS or LES solutions was clearly discernible in the LES simulations. Figure 6.3 shows an example of the predicted vertical profiles of mean streamwise velocity and turbulence kinetic energy at streamwise locations $x/H = 7.5$ (within a street canyon) and $x/H = 8.5$ (above the rooftop of a cube) [cf. Figure 6.1]. Figure 6.3 shows that the inlet fluctuations have little impact on the mean streamwise velocity profiles (since these inlet fluctuations with zero mean do not change the total mass flux), but have a great influence on the prediction of the turbulence kinetic energy above the obstacle array (viz., for $y/H > 1$). Shi et al. (2008) also reported similar observations in their LES study of flow over a group of buildings, where they compared the profiles of the mean streamwise and rms velocities obtained without fluctuations and with time-correlated inlet fluctuations.

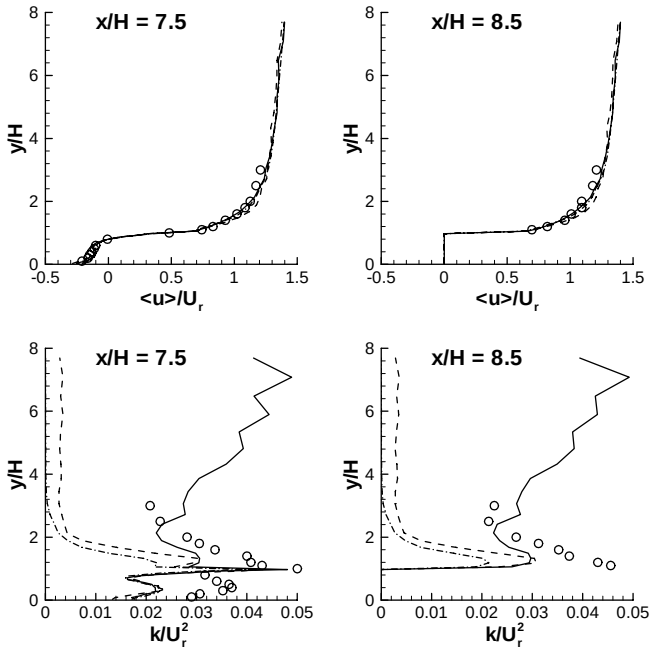

Figure 6.3. Inflow boundary condition sensitivity analysis: vertical profiles of the mean streamwise velocity and the turbulence kinetic energy obtained using LES. (○) Experimental data of Brown et al. (2001); (– · –) no fluctuations; (– –) random fluctuations; (—) time-correlated fluctuations.

The profiles of the turbulence kinetic energy obtained without fluctuations and with random fluctuations are very similar. Since random fluctuations have no spatial or temporal correlations, they dissipate quickly without sustaining turbulence within the solution domain (Schluter et al., 2004; Jarrin et al., 2006). This is clearly seen in Figure 6.3, where the magnitudes of the turbulence kinetic energy profiles obtained with random fluctuations drop rapidly above the obstacle array for $y/H > 1$. In contrast, the turbulence kinetic energy profiles obtained with time-correlated fluctuations show considerably improvement for $1 \le y/H \le 3$. However, the magnitudes of these profiles increase monotonically for $y/H > 2$, which is non-physical. This is likely due to the autocorrelation function $R(\Delta t) = \exp(-\Delta t/T_L)$ used in Eq. (6.4), where the value of $R(\Delta t)$ increases monotonically in the vertical direction as shown in Figure 6.4. A possible improvement to the predicted turbulence kinetic energy profiles is to set $R(\Delta t)$ to some constant (say, 0.5), or modify the integral time scale in $R(\Delta t)$ as $T_L = C_L \kappa_v y / U_{in}(y)$, where C_L is some number (closure constant) less than one (e.g., 0.5), in order to reduce the large correlations in time seen in Figure 6.4. This may alleviate the non-physical increase of turbulence kinetic energy with increasing distance for $y/H > 2$ as seen in Figure 6.3, although

further investigation is still required. While inlet fluctuations are important for PRNS and LES, it should be emphasized that it is not the objective of this thesis to generate realistic inlet fluctuations (which itself is a challenging subject of research that is still under investigation by many researchers). Therefore, the simple time-correlated fluctuations, constructed using Eq. (6.4), are used to generate the results for PRNS and LES in the next section.

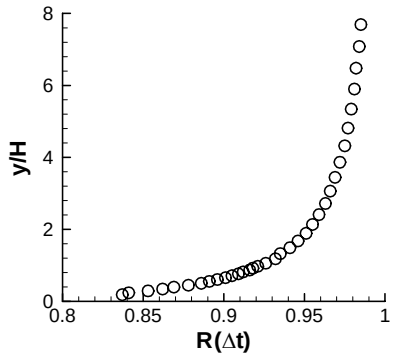

Figure 6.4. Vertical profile of the autocorrelation function for time-correlated fluctuations.

6.3 Results and Discussion

Predicted results for the mean streamwise velocity and the turbulence kinetic energy in the vertical x-y plane at $z/H = 0$ were compared with the experimental data at twelve selected streamwise locations displayed in Figure 6.1. These locations extend from the impact region upstream of the array, through the array interior, to the exit region downstream of the array.

6.3.1 Mean Velocity

The mean velocity vector fields predicted using URANS, PRNS and LES are shown in Figures 6.5 and 6.6. These two figures show that all the simulations produce similar flow patterns: a single vortex is formed between two consecutive cubes within each canyon, a recirculation bubble is present on the windward face of the first cube and at the exit region downstream of the array, and the rooftop recirculation is only apparent on the first cube. In addition, the mean flow within the street canyon seems to reach streamwise equilibrium by the third or fourth canyon. These predicted flow structures are qualitatively consistent with the experimental observations.

The measured stagnation point on the windward face of the first cube at $x/H = 0$ was located at $y/H \approx 0.7$, which is correctly captured by PRNS and LES as seen in Figure 6.5. However, URANS predicts

the stagnation point at $y/H \approx 0.6$. Figure 6.6 shows that the center of vortex within each canyon for PRNS and LES is located at $y/H \approx 0.75$ towards the leeward face of the upstream cube, which is consistent with the experimental findings. In contrast, the vortex center predicted by URANS is located towards the windward face of the downstream cube. The measured reattachment length of the recirculation zone behind the leeward face of the last cube was found to be $x/H \approx 1.5$. Figure 6.6 shows that PRNS and LES predict a reattachment length of $x/H \approx 1.5$ (where it is seen that the reattachment point at the floor occurs at $x/H \approx 14.5$, which corresponds to a distance of $1.5H$ downstream from the leeward face of the last cube at $x/H = 13$), which is in excellent agreement with the measurements. In contrast, URANS predicts a reattachment length of $x/H \approx 2.5$, which over-estimates the experimental value by about $1.0H$. Note that a reattachment length of $x/H \approx 2.5$ was also reported by Lien and Yee (2004), where their RANS calculations employed the standard and the Kato-Launder (Kato and Launder, 1993) k-ε models.

Vertical profiles of the measured and predicted mean streamwise velocity are presented in Figures 6.7 to 6.9. Figure 6.7 shows that the measured velocity profile in the impingement region upstream of the array at $x/H = -0.5$ is reproduced well by the three simulation approaches. All the predicted velocity profiles over the rooftop of the first and second cubes (i.e., at $x/H = 0.5$ and 2.5) and at the center of the first street canyon (at $x/H = 1.5$) are in good agreement with the experimental data, except that URANS slightly under-predicts the mean streamwise velocity above the obstacle array for $1 < y/H < 2$.

The velocity profiles shown in Figure 6.8 and top of Figure 6.9 correspond to the fully-developed flow within the array. It is observed that the vertical profiles of the mean streamwise velocity at $x/H = 7.5$, 9.5 and 11.5 (i.e., within the fourth, fifth and sixth street canyons) are almost identical to each other. Similarly, the profiles of the mean streamwise velocity at $x/H = 8.5$, 10.5 and 12.5 (i.e., above the rooftop of the fifth, sixth and seventh cubes) are almost the same. This suggests that the mean flow reaches streamwise equilibrium at about the fourth row of the cubes. The agreement between all the simulation results and the measurements is very good, except that URANS over-predicts the mean streamwise velocity in the recirculation zones ($y/H < 1$) within the street canyons at $x/H = 7.5$, 9.5 and 11.5. Figure 6.9 also shows that URANS under-predicts the mean streamwise velocity in the recirculation zone in the exit region downstream of the array at $x/H = 14.5$ and 16.5. In contrast, it is seen that PRNS and LES correctly predict the velocity profiles in this region.

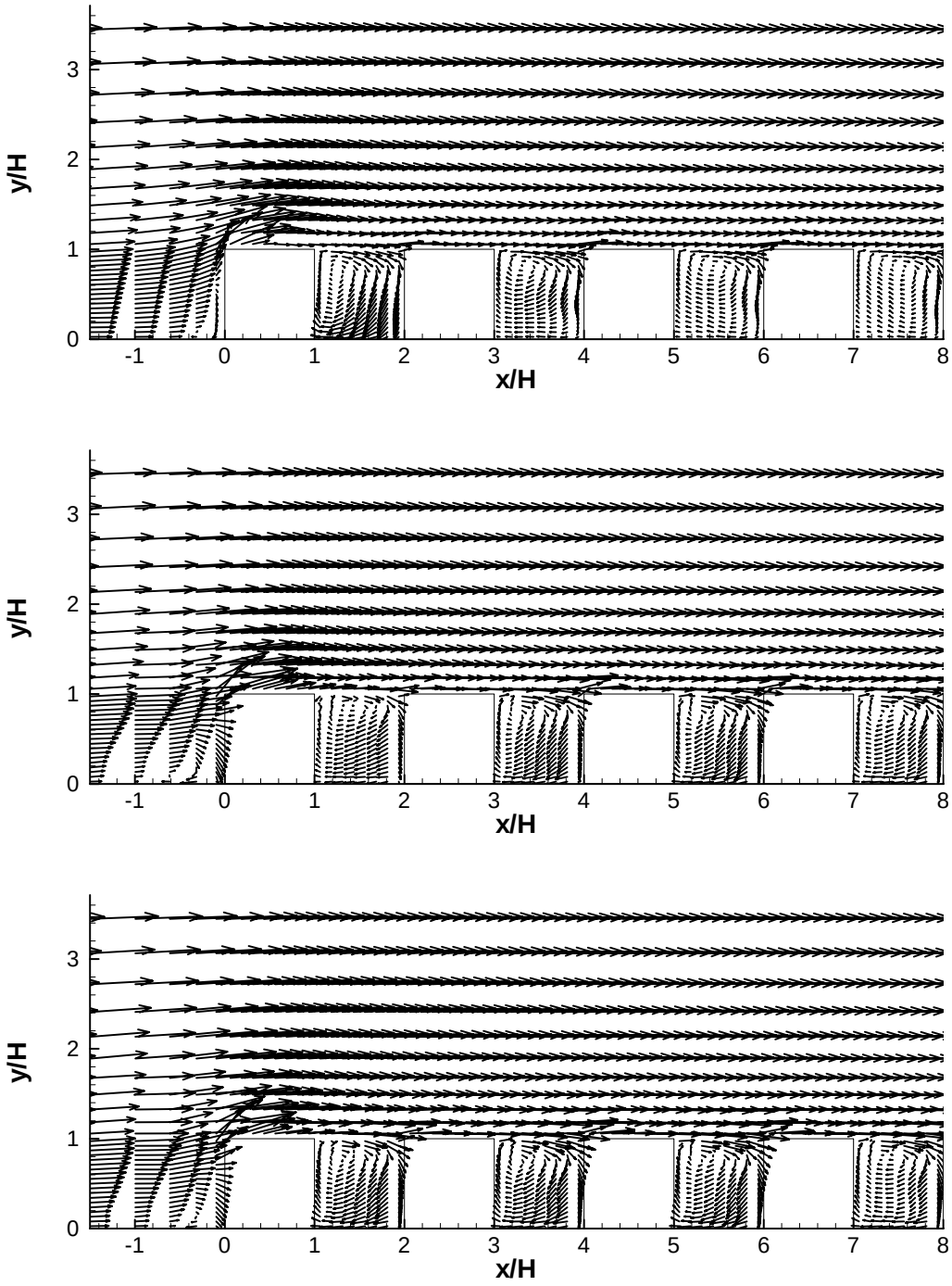

Figure 6.5. Mean velocity vector field in the impingement region upstream of and through the first four rows of cubes obtained using URANS (top), PRNS (middle) and LES (bottom).

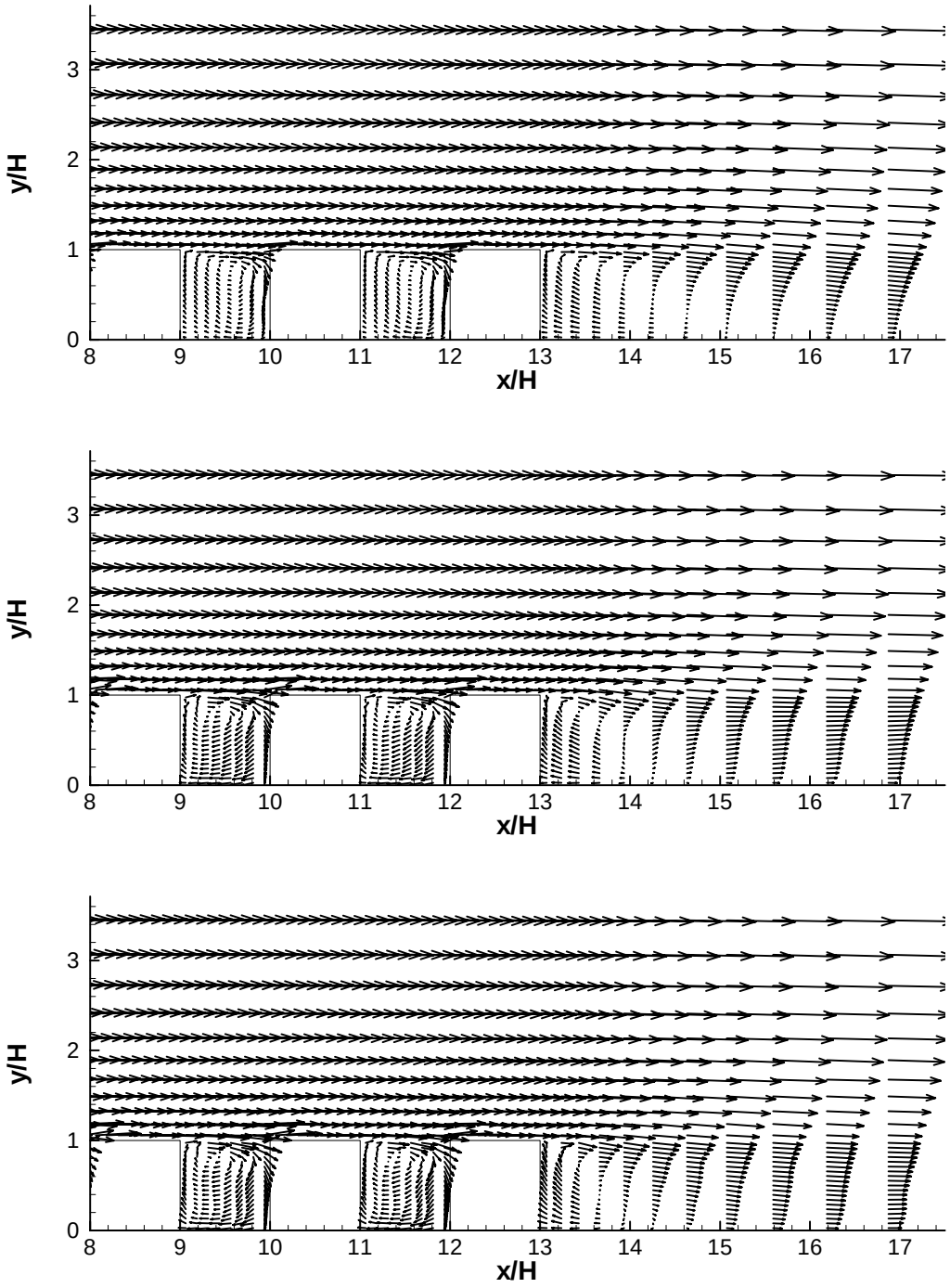

Figure 6.6. Mean velocity vector in the last three rows of cubes and in the exit region of the cube array obtained using URANS (top), PRNS (middle) and LES (bottom).

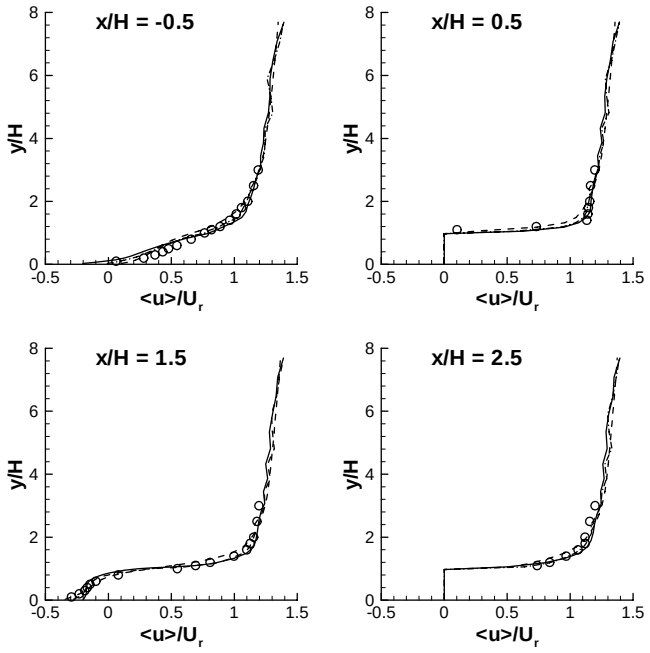

Figure 6.7. Vertical profiles of the mean streamwise velocity at four *x*-locations (*x*/*H* = –0.5, 0.5, 1.5 and 2.5). (○) Experimental data of Brown et al. (2001); (– –) URANS; (—) PRNS; (– · –) LES.

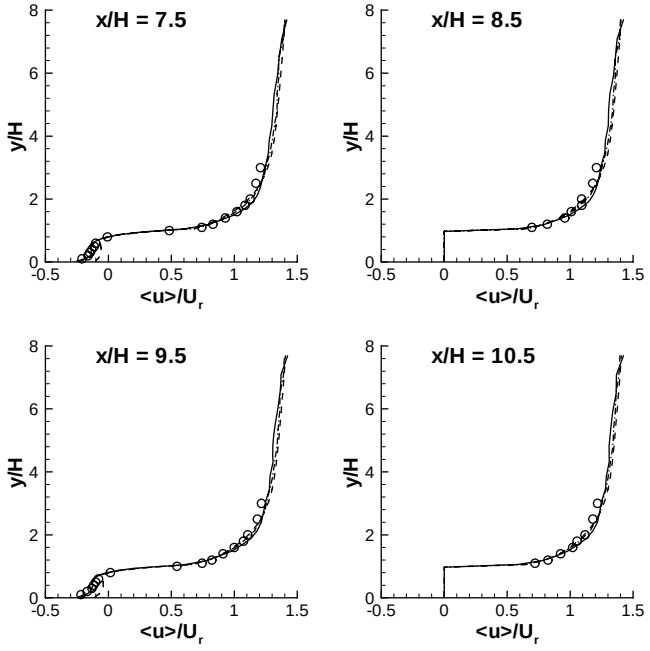

Figure 6.8. Vertical profiles of the mean streamwise velocity at four *x*-locations (*x*/*H* = 7.5, 8.5, 9.5 and 10.5). (○) Experimental data of Brown et al. (2001); (– –) URANS; (—) PRNS; (– · –) LES.

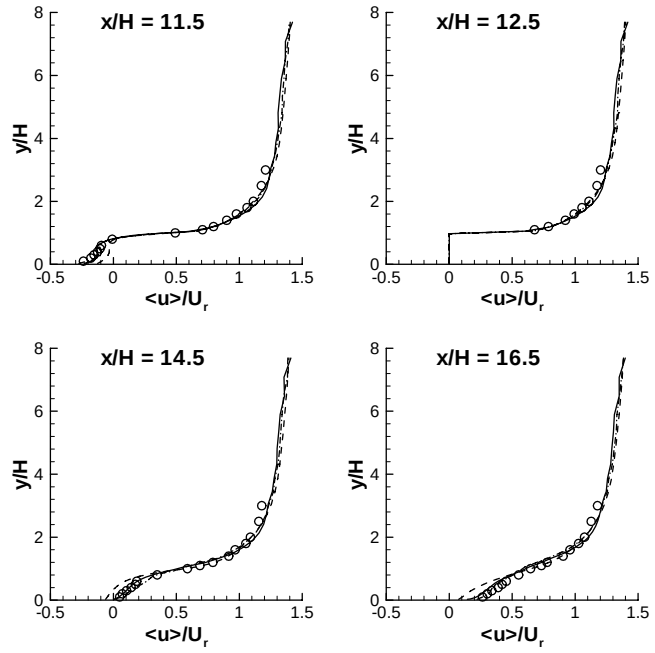

Figure 6.9. Vertical profiles of the mean streamwise velocity at four *x*-locations (*x*/*H* = 11.5, 12.5, 14.5 and 16.5). (○) Experimental data of Brown et al. (2001); (– –) URANS; (—) PRNS; (– · –) LES.

6.3.2 Turbulence Kinetic Energy

Vertical profiles of the turbulence kinetic energy (k) are displayed in Figures 6.10 to 6.12. It can be seen in these figures that the peak value of k at each x-location (except at $x/H = -0.5$ in the impact zone upstream of the array) occurs at or near the top of the obstacle array ($y/H \approx 1$). These peaks in k originate from the rooftops of the cubes where a thin intense shear layer develops, where the strong vertical velocity gradient (i.e., $\partial\overline{u}/\partial y$) within the shear layer contributes to a substantial production of k. The maximum value of k ($\approx 0.2U_r^2$) among these x-locations is found over the rooftop of the first cube at $x/H = 0.5$ (cf. Figure 6.10), resulting from the advection of strong k generated at the sharp top leading edge of the first cube when the flow impinges on the windward face of the cube. Figures 6.11 and 6.12 show that the measured profiles of k at $x/H = 7.5$, 9.5 and 11.5 are almost identical to each other. Similarly, the measured profiles of k at $x/H = 8.5$, 10.5 and 12.5 are almost the same.

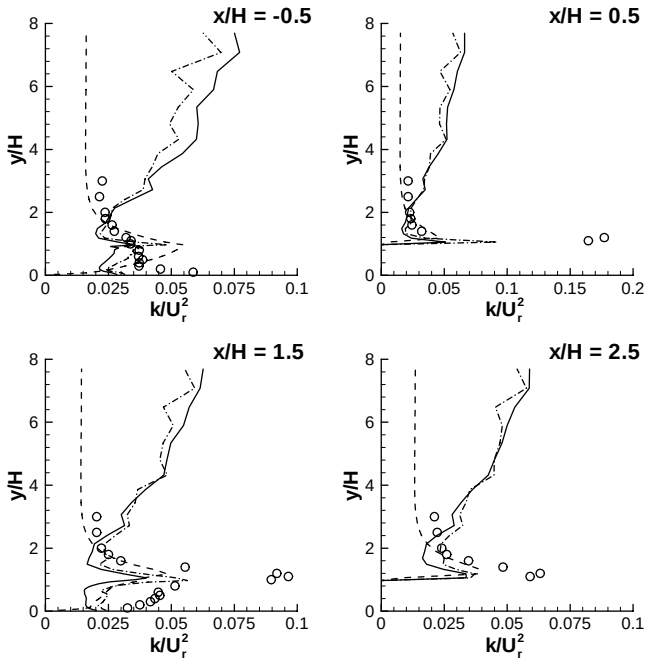

Figure 6.10. Vertical profiles of the turbulence kinetic energy at four *x*-locations (*x*/*H* = –0.5, 0.5, 1.5 and 2.5). (○) Experimental data of Brown et al. (2001); (– –) URANS; (—) PRNS; (– · –) LES.

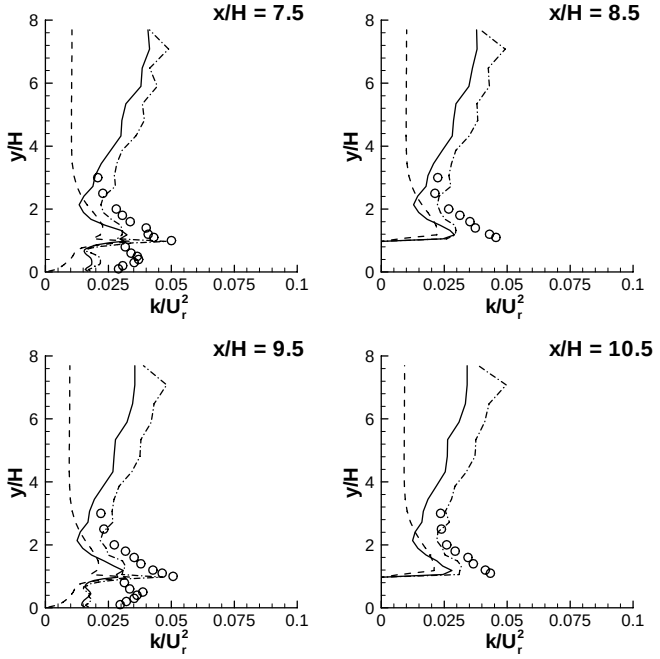

Figure 6.11. Vertical profiles of the turbulence kinetic energy at four *x*-locations (*x*/*H* = 7.5, 8.5, 9.5 and 10.5). (○) Experimental data of Brown et al. (2001); (– –) URANS; (—) PRNS; (– · –) LES.

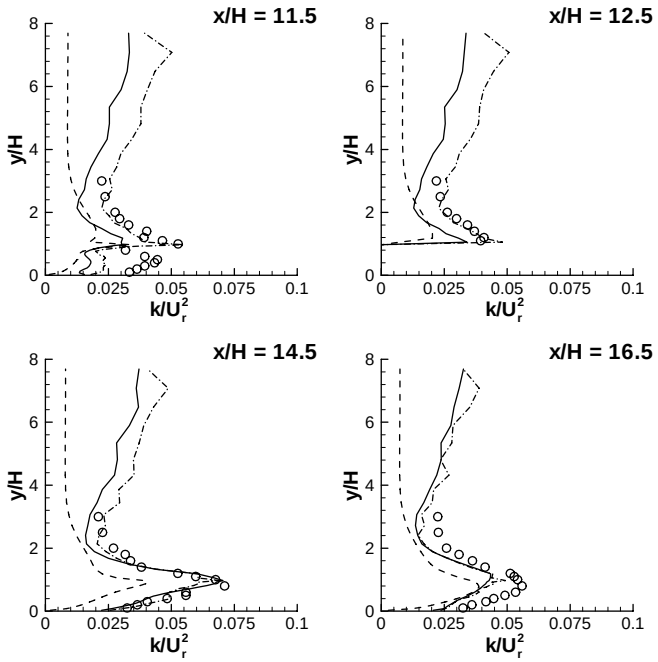

Figure 6.12. Vertical profiles of the turbulence kinetic energy at four *x*-locations (*x*/*H* = 11.5, 12.5, 14.5 and 16.5). (○) Experimental data of Brown et al. (2001); (– –) URANS; (—) PRNS; (– · –) LES.

The location of the peaks in k at $y/H \approx 1$ and the shape of the k profiles above the obstacle array for $1 < y/H < 3$ are generally reproduced well by all three simulations. In the region $y/H < 1$, the shape of the k profiles predicted by URANS in the impact zone (at $x/H = -0.5$) and within the street canyons (at x/H = 7.5, 9.5 and 11.5) do not agree well with the measurements. URANS fails to predict the decrease in the k profiles for $0 < y/H < 0.5$ at $x/H = -0.5$ (cf. Figure 6.10) and for $0.5 < y/H < 1$ at x/H = 7.5, 9.5 and 11.5 (cf. Figures 6.11 and 6.12). In contrast, both PRNS and LES capture the right trends of the k profiles here. In general, the shape of the k profiles obtained from PRNS and LES are very similar to each other and are in a better conformance with the experimental data than the URANS solution.

In terms of the magnitude of the k profiles, URANS under-predicts the peak values of k at $y/H \approx 1$, although the location of these peaks is well captured. In the region $y/H > 1$, URANS generally under-estimates the levels of k by approximately 30% to 40% (cf. Figures 6.11 and 6.12), except at locations near the impingement zone (at $x/H = -0.5$ and 0.5) and in the flow adjustment zone (at x/H = 1.5 and 2.5) [cf. Figure 6.10] where the agreement of the k levels with the measurements is satisfactory.

Furthermore, it is observed that URANS predicts excessive level of k for $0.5 < y/H < 1.5$ at $x/H = -0.5$. The over-prediction of URANS here is due to the use of the standard k-ε model, where the standard k-ε model is known to predict an excessive production of k near the stagnation point of flows impinging on walls (Lien and Yee, 2004). Note that the measured stagnation point on the windward face of the first cube at $x/H = 0$ was located at $y/H \approx 0.7$. The discrepancies between the URANS results and the experimental data are large for $y/H < 1$, particularly at $x/H = 7.5$, 9.5 and 11.5 where URANS significantly under-predicts the values of k by about 65% (cf. Figures 6.11 and 6.12). The deficiency of URANS is associated with the weaknesses of the linear Boussinesq stress-strain relationship, where the use of an isotropic eddy viscosity to characterize the Reynolds stresses cannot be expected to properly account for the effects of anisotropy in the Reynolds normal stresses.

PRNS and LES solutions, are generally comparable with the URANS predictions in the impact and flow adjustment zones of the array for $y/H < 2$ (cf. Figure 6.10), but are better than the URANS results in the fully-developed and exit regions of the array for $y/H < 3$ (cf. Figures 6.11 and 6.12). In general, LES predictions give the best quantitative agreement of the k levels with the measurements. However, Figures 6.11 and 6.12 show that PRNS and LES also under-predict the values of k by about 50% within the street canyons (at $x/H = 7.5$, 9.5 and 11.5) for $y/H < 1$, which might be due to an insufficient grid resolution used in these regions. In the LES study of similar cube arrays by Hanna et al. (2002), they also reported that the simulated turbulent intensities are generally less than the measured values by about 40% in the fully-developed region within the array.

6.3.3 Reynolds Normal Stresses

Figures 6.13 to 6.16 display the representative results of the Reynolds normal stresses near the impingement region upstream of the array (at $x/H = -0.5$ and 0.5), in the flow adjustment region (at $x/H = 1.5$ and 2.5), in the fully-developed region (at $x/H = 7.5$ and 8.5) within the array, and in the exit region downstream of the array (at $x/H = 14.5$ and 16.5). It is evident from these figures that the measured Reynolds normal stresses are strongly anisotropic, with $\overline{u'u'} > \overline{w'w'} > \overline{v'v'}$.

Figure 6.13 shows that the peak value of the Reynolds normal stresses at $x/H = -0.5$ occurs near the ground at $y/H \approx 0$. However, URANS wrongly predicts the location of these peaks at $y/H \approx 1$. In addition, URANS substantially over-predicts the values of $\overline{u'u'}$ and $\overline{v'v'}$ for $0.5 < y/H < 1$ and $0.5 < y/H < 2$, respectively, which yields the excessive level of k for $0.5 < y/H < 1.5$ at $x/H = -0.5$ as seen in

Figure 6.10. In contrast, the Reynolds normal stresses profiles predicted by PRNS and LES are in a better agreement with the experimental data, although PRNS and LES significantly under-predict the magnitude of $\overline{w'w'}$ for $y/H < 2$. The magnitude of the Reynolds normal stresses predicted by the three simulations at $x/H = 0.5$ are comparable to the measurements for $1 < y/H < 3$, but all the simulations considerably under-predict the peak values of these normal stresses at $y/H \approx 1$.

From Figure 6.14, it is seen that the location of the peaks in the Reynolds normal stresses at $y/H \approx 1$ is correctly captured by the three simulations at $x/H = 1.5$ and 2.5. However, the discrepancy between the predicted and measured peak values of these normal stresses is generally large, with the exception that the peak values of $\overline{u'u'}$ predicted by PRNS and LES and the peak values of $\overline{v'v'}$ predicted by URANS are in good agreement with the corresponding measured peak values. It is seen that PRNS and LES are able to reproduce the anisotropic behavior of the Reynolds normal stresses (where $\overline{u'u'} > \overline{w'w'} > \overline{v'v'}$), whereas URANS is unable to properly reproduce this anisotropy due to the use of the Boussinesq (linear) eddy viscosity approximation for the Reynolds stresses.

The shape and magnitude of the Reynolds normal stress profiles at $x/H = 7.5$ and 8.5 shown in Figure 6.15 are generally better reproduced by PRNS and LES than by URANS. The Reynolds normal stress profiles predicted by PRNS and LES are visibly anisotropic, but the normal stresses profiles predicted by URANS appear to be nearly isotropic. At $x/H = 7.5$ and 8.5, URANS under-estimates the peak values of $\overline{u'u'}$ by more than 60%, whereas the peak values predicted by PRNS and LES are within 20% of the measurements. In addition, the shapes of the Reynolds normal stresses for $y/H < 1$ at $x/H = 7.5$ are better estimated by PRNS and LES, although PRNS and LES under-predict the magnitude of these stresses by about 50%.

Figure 6.16 shows that the shapes of the Reynolds normal stresses profiles in the exit region downstream of the array at $x/H = 14.5$ and 16.5 are well captured by all three simulations. PRNS and LES solutions generally show better quantitative agreement of the Reynolds normal stress levels (particularly for $\overline{u'u'}$) with the experimental data than the URANS results, except at $x/H = 16.5$ where PRNS and LES significantly under-estimate the measured value of $\overline{w'w'}$ by 50%.

Overall, the consistently better performance of PRNS and LES relative to URANS is clearly seen in the predictions of the anisotropy in the Reynolds normal stresses (cf. Figures 6.13 to 6.16). In this regard, the predictive performance of PRNS is similar to that of LES.

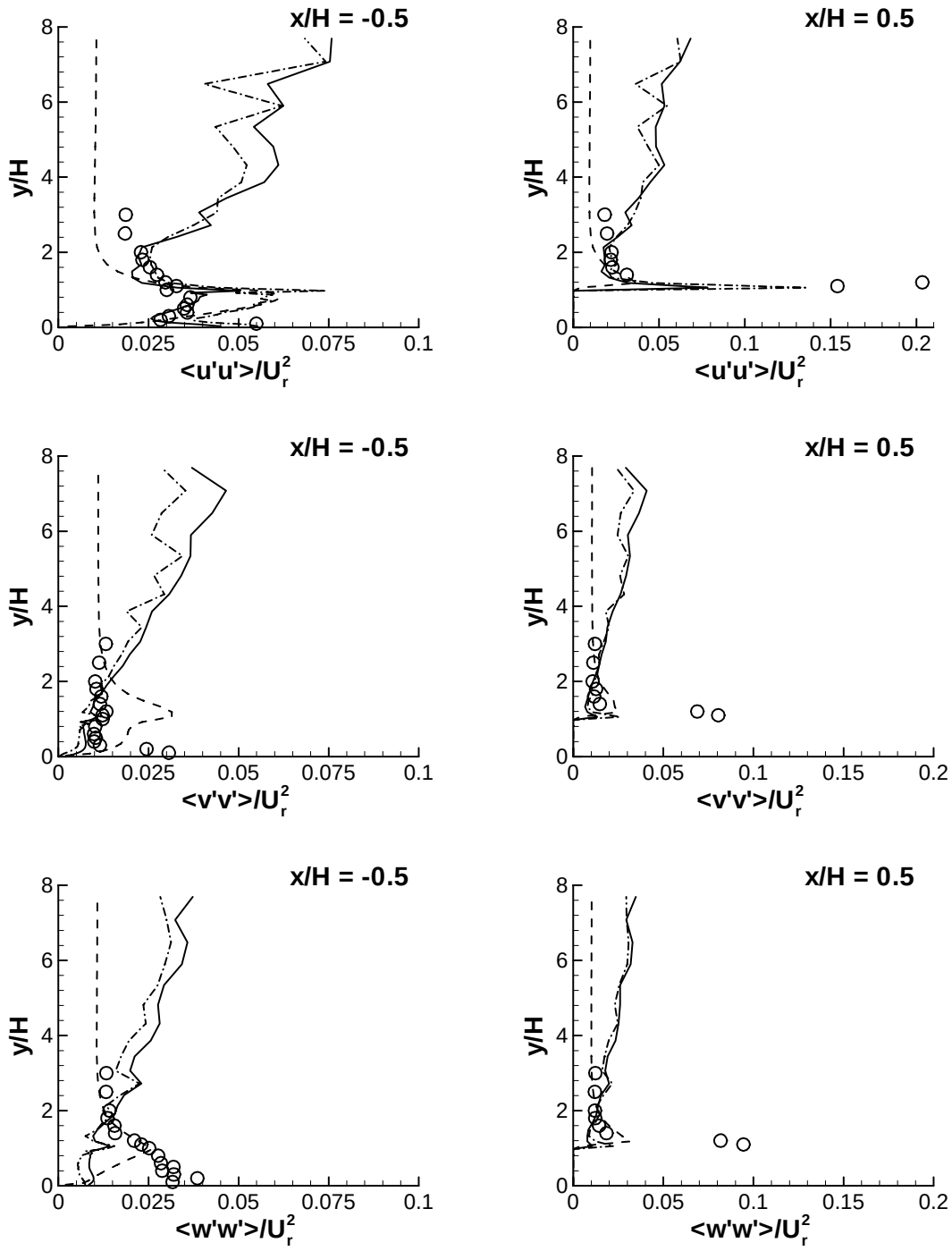

Figure 6.13. Vertical profiles of the Reynolds normal stresses near the impingement region at locations x/H = –0.5 and 0.5. (○) Experimental data of Brown et al. (2001); (– –) URANS; (—) PRNS; (– · –) LES.

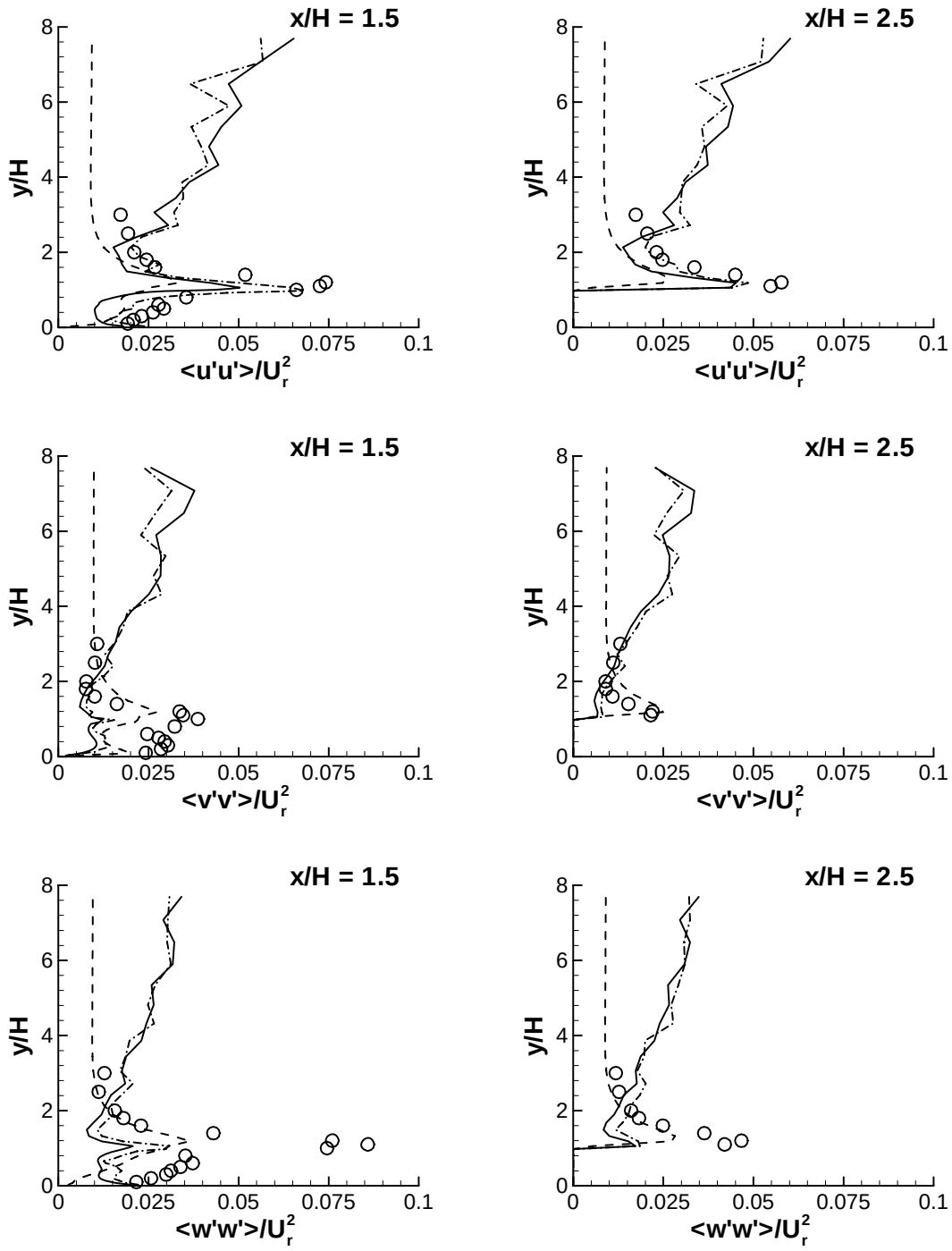

Figure 6.14. Vertical profiles of the Reynolds normal stresses in the flow adjustment region within the array at locations x/H = 1.5 and 2.5. (○) Experimental data of Brown et al. (2001); (– –) URANS; (—) PRNS; (– · –) LES.

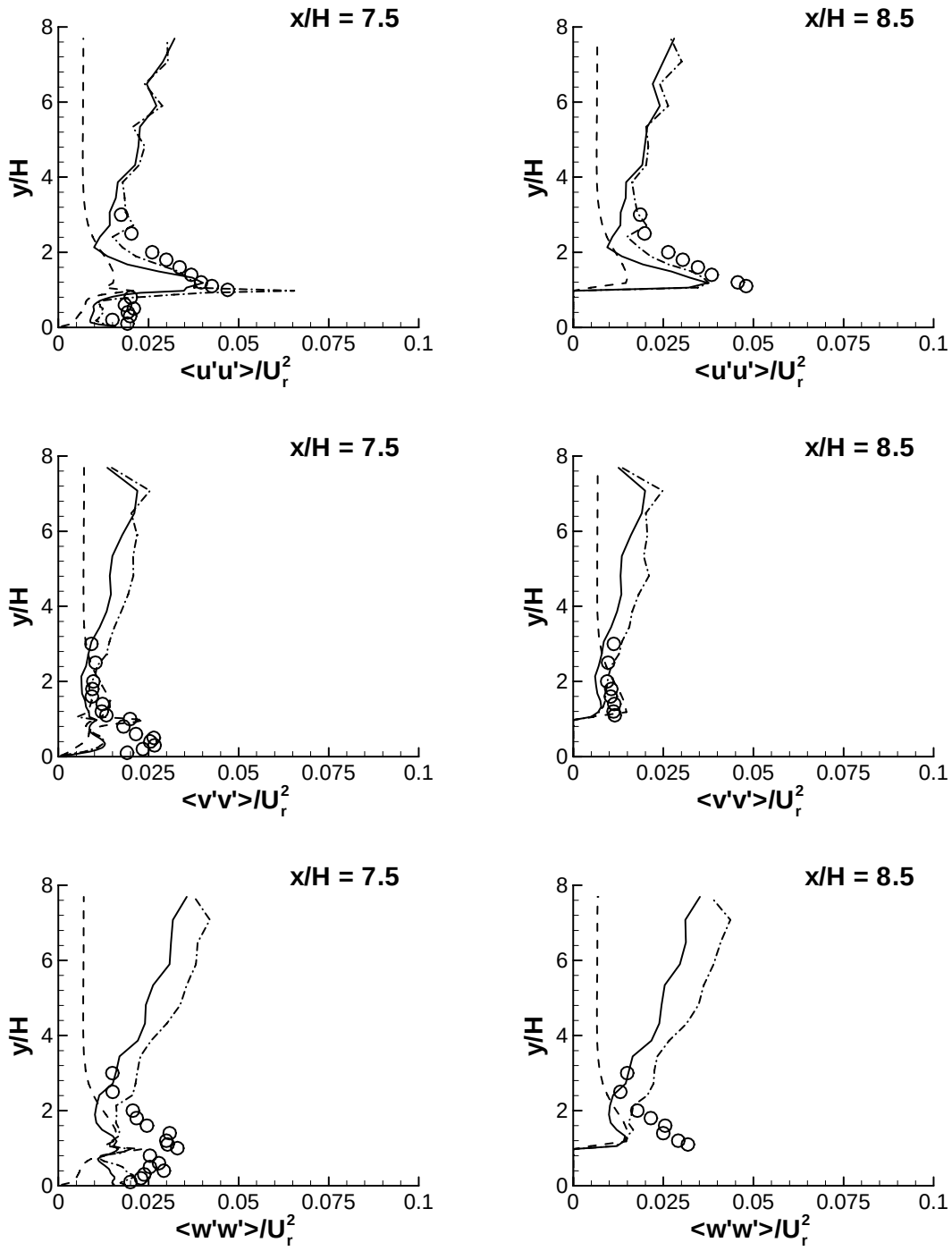

Figure 6.15. Vertical profiles of the Reynolds normal stresses in the fully-developed region within the array at locations x/H = 7.5 and 8.5. (○) Experimental data of Brown et al. (2001); (– –) URANS; (—) PRNS; (– · –) LES.

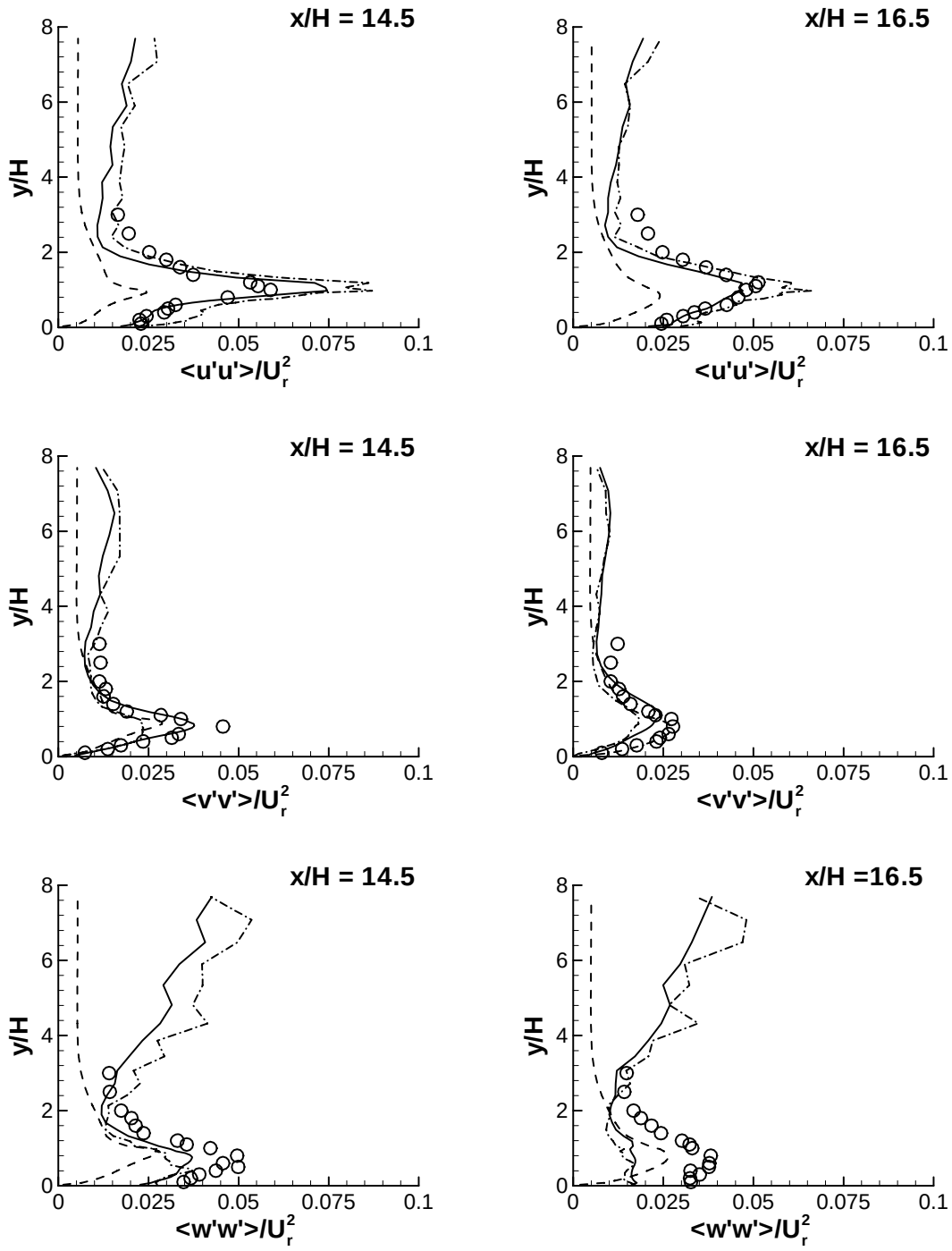

Figure 6.16. Vertical profiles of the Reynolds normal stresses in the exit region downstream of the array at locations x/H = 14.5 and 16.5. (○) Experimental data of Brown et al. (2001); (– –) URANS; (—) PRNS; (– · –) LES.

6.3.4 Resolution Control Function

The reasonably good conformance of PRNS solutions with the experimental measurements in terms of the mean flow and turbulent quantities indicates that the value of the closure constant $C_\kappa = 40$ [cf. Eq. (2.32)], used in the formulation of F_R [cf. Eq. (2.27)] in PRNS, is also applicable to a developing flow over a matrix of cubes.

Figure 6.17 shows the distributions of F_R in the proximity of the obstacle array in a vertical x-y plane at $z/H = 0$ and in a horizontal x-z plane at $y/H = 0.5$. The value of F_R varies across these planes, with higher value observed towards the cube faces. It is seen that the value of F_R in the vicinity of one cube is almost the same as the value of F_R in the vicinity of the neighboring cubes, with the exception of the value of F_R in the impact region upstream of the array and in the exit region downstream of the array. In addition, it is seen that the contours of F_R are symmetrical along the centerline at $z/H = 0$ in the $y/H = 0.5$ plane.

6.4 Closure

The effect of the inlet fluctuations on the flow solutions for PRNS and LES was investigated. It was found that the inlet fluctuations have little impact on the mean streamwise velocity profiles, but have a great influence on the prediction of the turbulence kinetic energy above the obstacle array.

The mean flow structures, such as a vortex within each street canyon, as well as the recirculation bubble on the windward face of the first cube and in the exit region of the cube array, were reproduced fairly well by URANS, PRNS and LES. The stagnation point on the windward face of the first cube, the center of the vortex, and the reattachment length downstream of the cube array, predicted by PRNS and LES were in good agreement with the experimental observations, whereas URANS predictions exhibited some discrepancies. In terms of the shape and magnitude of the profiles of the turbulence kinetic energy and the Reynolds normal stresses, both PRNS and LES results generally showed a better agreement with the experimental data than the URANS solutions. In particular, PRNS and LES outperform URANS in reproducing the anisotropic behavior of the Reynolds normal stresses. The predictive performance of PRNS, qualitatively and quantitatively, is similar to that of LES overall.

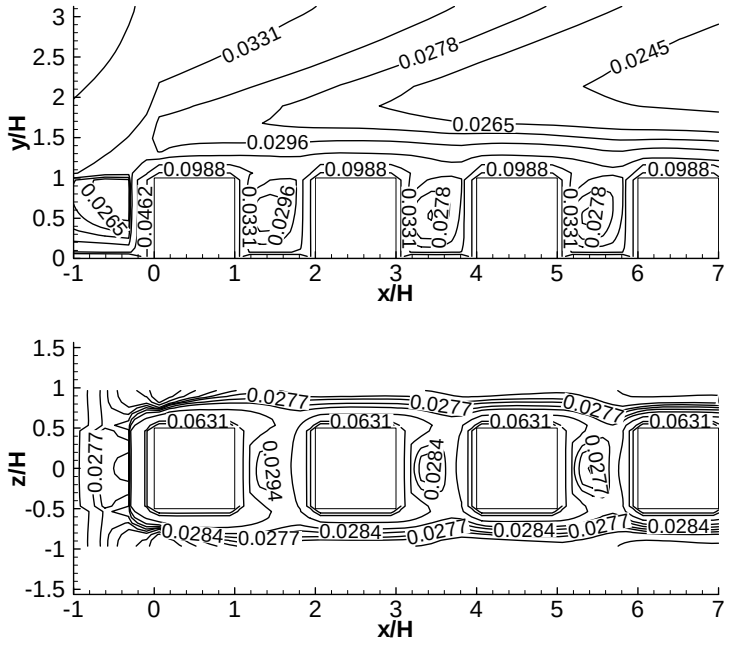

(a)

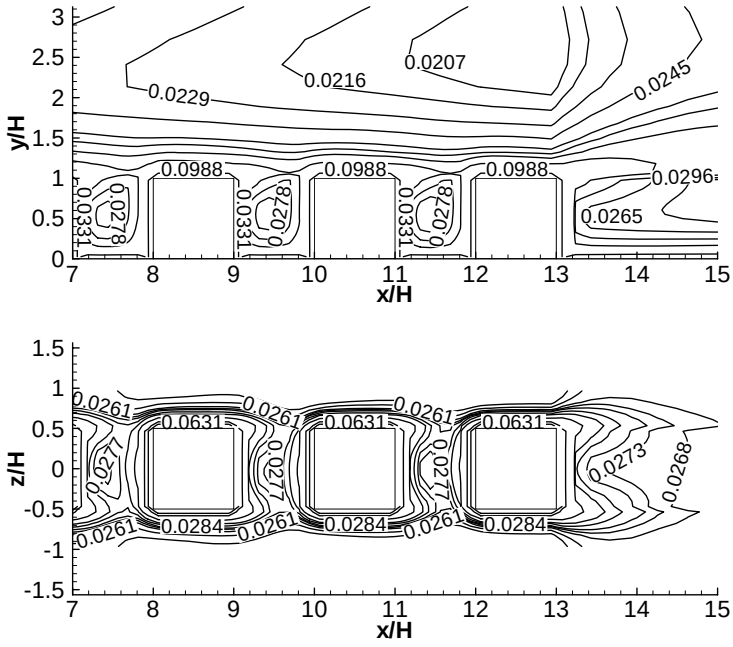

(b)

Figure 6.17. Contours of resolution control function in the *x*-*y* plane at *z*/*H* = 0 (top) and in the *x*-*z* plane at *y*/*H* = 0.5 (bottom). (a) for first 4 cubes; (b) for last 3 cubes.

Chapter 7

Conclusions and Directions for Future Work

7.1 Achievements

PRNS, a variant of non-zonal hybrid numerical simulation approaches, was studied in this thesis. The numerical performance of PRNS, with a newly proposed functional form for F_R used in the standard k-ε model framework, was evaluated against URANS (with the standard k-ε model) and LES (with the Smagorinsky model) for three different turbulent flows. In all three modeling approaches, wall functions were used at the solid surfaces in the test problems investigated.

The proposed formulation of F_R contains a closure constant C_κ. The value of $C_\kappa = 40$ used in all the PRNS computations (based on the standard k-ε model framework) presented in this thesis, was calibrated based on a fully-developed plane channel flow. The good agreement of PRNS predictions with the experimental measurements of fully-developed and developing flows over a matrix of cubes further suggests that $C_\kappa = 40$ remains valid in complex turbulent flows dominated by unsteady large-scale turbulent structures.

For the simulation of a plane channel flow, the mean streamwise velocity predicted by URANS agreed well with the DNS data, whereas the PRNS and LES solutions showed a velocity shift (a common problem seen in many hybrid RANS/LES approaches and in LES used with wall models). This velocity shift was due to the fact that PRNS and LES (both applied with wall functions) experienced a transition from a region where the turbulence was largely modeled to one where it was largely resolved. However, the PRNS and LES predictions were able to capture the near-wall anisotropic behavior of the rms velocities (where the PRNS results gave the best overall conformance

with the v'_{rms} and w'_{rms} profiles), whereas the URANS results incorrectly exhibited isotropic rms velocities.

For a fully-developed flow over an array of cubes, the mean flow structures such as separation and recirculation bubbles, were reproduced reasonably well by URANS, PRNS and LES. In general, the URANS results did not agree well with the experimental data, particularly for the predictions of the Reynolds stresses within the recirculation zone in the lee of the cube. In contrast, PRNS and LES provided good predictions for the mean velocities and Reynolds stresses, and between them PRNS showed similar but slightly better performance than LES.

For the simulation of a developing flow over a matrix of cubes, structures in the mean flow, such as a single vortex within each canyon and a recirculation bubble in the exit region downstream of the cube array, were captured fairly well by URANS, PRNS and LES. The predicted mean streamwise velocity profiles from all three simulations were in good conformance with the experimental measurements, except that the URANS results in the recirculation zones within the street canyons and in the exit region were less satisfactory. PRNS and LES generally gave better predictions for the turbulence kinetic energy and the Reynolds normal stresses than that of URANS, both in terms of the shapes of the profiles and their magnitudes. The superior performance of PRNS and LES over URANS was evidently seen in the predictions of the anisotropy in the Reynolds normal stresses. Overall, the predictive performance of PRNS was similar to that of LES.

For each test case, computations from URANS, PRNS and LES were performed using the same mesh and time step sizes. It was found that the computational cost (in terms of the computing time to run the simulation) of PRNS and LES (with the near-wall turbulence modeled by wall functions) was approximately the same, but was about 10 times greater than that of URANS over a mesh of about 48×48×48 nodes. This shows that the predictive accuracy of PRNS and LES over URANS comes with the price of high computational cost. Although the present (high-Reynolds-number) PRNS and "wall-modeled" LES showed comparable computational efficiency, it is expected that the computational cost of the present PRNS model is significantly less than that of "wall-resolved" LES (which requires a fine grid resolution along with a small time step size to resolve the small-scale turbulence near the wall), in particular when the dynamic procedure proposed by Germano et al. (1991) is employed.

Results for all three test cases indicate that the predictive performance of PRNS (with the proposed functional form for F_R), qualitatively and quantitatively, is comparable to that of (wall-modeled) LES, but better than that of URANS. These encouraging results demonstrate the capability and accuracy of PRNS to predict complex turbulent flows.

7.2 Future Work

The near-wall turbulence in the PRNS computations was modeled using wall functions in this study. It is suggested to examine the effect of including near-wall treatments in the present PRNS approach, by using a low-Reynolds-number k-ε model [e.g., Launder & Sharma (1974) and Lien & Leschziner (1993)] as a base model. This base model would account for the interaction between turbulence and molecular viscosity in the near-wall regions where viscous effects are important. It would be interesting to compare the performance of the low-Reynolds-number k-ε PRNS model with that of the standard (high-Reynolds-number) k-ε model with wall functions, particularly for engineering problems in which heat transfer effects are important.

The predictive accuracy of PRNS depends on the capability of the RANS turbulence model that is used to represent the effect of the unresolved motions on the resolved ones. Another interesting line for further investigation of PRNS is to test more advanced turbulence RANS models (e.g., non-linear k-ε models and Reynolds-stress transport models) as base models in PRNS. Finally, it should be mentioned here the value of the closure constant C_κ in the proposed formulation of F_R is by no means optimal, and further calibration of this model constant for a wider range of flow conditions with different characteristics, such as buoyancy, rotation, compressibility, chemical reaction, is still required.

Bibliography

Baik, J.-J., Kim, J.-J. (1999), "A numerical study of flow and pollutant dispersion characteristics in urban street canyons", Journal of Applied Meteorology, Vol. 38, pp. 1576-1589.

Batten, P., Goldberg, U., Chakravarthy, S. (2004), "Interfacing statistical turbulence closures with large-eddy simulation", AIAA Journal, Vol. 42, pp. 485-492.

Benarafa, Y., Cioni, O., Ducros, F., Sagaut, P. (2006), "RANS/LES coupling for unsteady turbulent flow simulation at high Reynolds number on coarse meshes", Computer Methods in Applied Mechanics and Engineering, Vol. 195, pp. 2939-2960.

Boussinesq, J. (1877), "Essai sur la theories des eaux courantes", Memoires presentes par divers savants a l'Academic des Sciences de l'Institut National de France, Vol. 23, pp. 46-50.

Brown, M.J., Lawson, R.E., DeCroix, D.S., Lee, R.L. (2001), "Comparison of centerline velocity measurements obtained around 2D and 3D building arrays in a wind tunnel", Report LA-UR-01-4138, Los Alamos National Laboratory, Los Alamos, NM, 7 pp.

Cabot, W., Moin, P. (1999), "Approximate wall boundary conditions in the large-eddy simulation of high Reynolds number flow", Flow, Turbulence and Combustion, Vol. 63, pp. 269-291.

Chapman, D.R. (1979), "Computational aerodynamics development and outlook", AIAA Journal, Vol. 17, pp. 1293-1313.

Cheng, Y., Lien, F.S., Yee, E., Sinclair, R. (2003), "A comparison of large-eddy simulations with a standard k-ε Reynolds-averaged Navier-Stokes model for the prediction of a fully developed turbulent flow over a matrix of cubes", Journal of Wind Engineering and Industrial Aerodynamics, Vol. 91, pp. 1301-1328.

Craft, T.J. (Ed.) (1998), "Proceedings of the 7th ERCOFTAC/IAHR/COST workshop on refined turbulence modeling", Manchester, UK.

Davidson, L., Billson, M. (2006), "Hybrid LES-RANS using synthesized turbulent fluctuations for forcing in the interface region", International Journal of Heat and Fluid Flow, Vol. 27, pp. 1028-1042.

Davidson, L., Dahlstrom, S. (2005), "Hybrid LES-RANS: an approach to make LES applicable at high Reynolds number", International Journal of Computational Fluid Dynamics, Vol. 19, pp. 415-427.

Davidson, L., Peng, S.H. (2003), "Hybrid LES-RANS modeling: a one-equation SGS model combined with a k-ω model for predicting recirculating flows", International Journal for Numerical Methods in Fluids, Vol. 43, pp. 1003-1018.

Deardorff, J.W. (1970), "A numerical study of three-dimensional turbulent channel flow at large Reynolds numbers", Journal of Fluid Mechanics, Vol. 41, pp. 453-480.

Fasel, H.F., Seidel, J., Wernz, S. (2002), "A methodology for simulations of complex turbulent flows", Journal of Fluids Engineering, Vol. 124, pp. 933-942.

Fasel, H.F., von Terzi, D.A., Sandberg, R.D. (2006), "A methodology for simulating compressible turbulent flows", Journal of Applied Mechanics, Vol. 73, pp. 405-412.

Ferziger, J.H., Peric, M. (2002), "Computational methods for fluid dynamics", Springer-Verlag.

Germano, M., Piomelli, U., Moin, P. (1991), "A dynamic subgrid-scale eddy viscosity model", Physics of Fluids A, Vol. 3, pp. 1760-1765.

Hamba, F. (2003), “A hybrid RANS/LES simulation of turbulent channel flow”, Theoretical and Computational Fluid Dynamics, Vol. 16, pp. 387-403.

Hanjalic, K., Obi, S. (Eds.) (1997), “Proceedings of the 6th ERCOFTAC/IAHR/COST workshop on refined flow modeling”, Delft, The Netherlands.

Hanna, S.R., Tehranian, S., Carissimo, B., Macdonald, R.W., Lohner R. (2002), “Comparisons of model simulations with observations of mean flow and turbulence within simple obstacle arrays”, Atmospheric Environment, Vol. 36, pp. 5067-5079.

Hellsten, A., Rautaheimo, P. (Eds.) (1999), “Proceedings of the 8th ERCOFTAC/IAHR/COST workshop on refined turbulence modeling”, Helsinki, Finland.

Hsieh, K.-J., Lien, F.-S., Yee, E. (2007a), “Numerical modeling of scalar dispersion in an urban canopy”, Journal of Wind Engineering and Industrial Aerodynamics, Vol. 95, pp. 1611-1636.

Hsieh, K.-J., Lien, F.-S., Yee, E. (2007b), “Partially resolved numerical simulation for complex wall-bounded turbulent flows”, Proceedings of the 15th Annual Conference of the CFD Society of Canada, Toronto, Canada.

Hsieh, K.-J., Lien, F.-S., Yee, E. (2008), “Towards a unified turbulence simulation approach for wall-bounded flows”, submitted to Flow, Turbulence and Combustion.

Hunter, L.J., Johnson, G.T., and Watson, I.D. (1992), “An investigation of three-dimensional characteristics of flow regimes within the urban canyon”, Atmospheric Environment, Vol. 26B, pp. 425-432.

Jarrin, N., Benhamadouche, S., Laurence, D., Prosser R. (2006), “A synthetic-eddy-method for generating inflow conditions for large-eddy simulations”, International Journal of Heat and Fluid Flow, Vol. 27, pp. 585-593.

Kato, M., Launder, B. E. (1993), “The modeling of turbulent flow around stationary and vibrating square cylinders”, Proceedings of the 9th Symposium on Turbulent Shear Flows, Kyoto, Japan.

Kim, J.-J., Baik, J.-J. (1999), “A numerical study of thermal effects on flow and pollutant dispersion in urban street canyons”, Journal of Applied Meteorology, Vol. 38, pp. 1249-1261.

Kim, J.-J., Baik, J.-J. (2004), “A numerical study of the effects of ambient wind direction on flow and dispersion in urban street canyons using the RNG k-ε model”, Atmospheric Environment, Vol. 38, pp. 3039-3048.

Larsson, J., Lien, F.S., Yee, E. (2007), “The artificial buffer layer and the effect of forcing in hybrid LES/RANS”, International Journal of Heat and Fluid Flow, Vol. 28, pp. 1443-1459.

Launder, B.E., Sharma, B.I. (1974), "Application of the energy-dissipation model of turbulence to the calculation of flow near a spinning disc", Letters in Heat and Mass Transfer, Vol. 1, pp. 131-138.

Launder, B.E., Spalding, D.B. (1974), “The numerical computation of turbulent flows”, Computer Methods in Applied Mechanics and Engineering, Vol. 3, pp. 269-289.

Lien, F.S., Leschziner, M.A. (1993), “Computational modelling of 3D turbulent flow in S-diffuser and transition ducts”, Engineering Turbulence Modelling and Measurements 2, Elsevier, pp. 217-228.

Lien, F.S., Leschziner, M.A. (1994a), “A general non-orthogonal collocated finite volume algorithm for turbulent flow at all speeds incorporating second-moment closure, Part 1: numerical implementation”, Computer Methods in Applied Mechanics and Engineering, Vol. 114, pp. 123-148.

Lien, F.S., Leschziner, M.A. (1994b), “Upstream monotonic interpolation for scalar transport with application in complex turbulent flows”, International Journal for Numerical Methods in Fluids, Vol. 19, pp. 527-548.

Lien, F.-S., Yee, E. (2004), “Numerical modelling of the turbulent flow developing within and over a 3-D building array, Part I: a high-resolution Reynolds-averaged Navier-Stokes approach”, Boundary-Layer Meteorology, Vol. 112, pp. 427-466.

Lien, F.-S., Yee, E., Ji, H., Hsieh, K.-J. (2008), “Partially resolved numerical simulation and RANS modeling of flow and passive scalar transport in an urban environment”, Journal of Wind Engineering and Industrial Aerodynamics, Vol. 96, pp. 1832-1842.

Liu, C.-H., Barth, M.C. (2002), “Large-eddy simulation of flow and scalar transport in a modeled street canyon’, Journal of Applied Meteorology, Vol. 41, pp. 660-673.

Liu, C.-H., Barth, M.C., Leung, D.Y.C. (2004), “Large-eddy simulation of flow and pollutant transport in street canyons of different building-height-to-street-width ratios”, Journal of Applied Meteorology, Vol. 43, pp. 1410-1424.

Liu, N.-S., Shih, T.-H. (2006), “Turbulence modeling for very large-eddy simulation”, AIAA Journal, Vol. 44, pp. 687-697.

Mathey, F., Frohlich, J., Rodi, W. (1999), "Large-eddy simulation of the flow over a matrix of surface-mounted cubes", Lecture Notes in Physics, Springer, Vol. 529, pp. 153-163.

Meinders, E.R., Hanjalic, K. (1999), “Vortex structure and heat transfer in turbulent flow over a wall-mounted matrix of cubes”, International Journal of Heat and Fluid Flow, Vol. 20, pp. 255-267.

Moser, R.D., Kim, J., Mansour, N.N. (1999), “Direct numerical simulation of turbulent channel flow up to $Re_\tau = 590$”, Physics of Fluids, Vol. 11, pp. 943-945.

Niceno, B., Dronkers, A.D.T., Hanjalic, K. (2002), “Turbulent heat transfer from a multi-layered wall-mounted cube matrix: a large-eddy simulation”, International Journal of Heat and Fluid Flow, Vol. 23, pp. 173-185.

Niceno, B., Hanjalic, K. (1999), “Flow in a matrix of surface-mounted cubes – Test Case 6.2: description of numerical methodology”, Proceedings of the 8th ERCOFTAC/IAHR/COST Workshop on Refined Turbulence Modeling, Helsinki, Finland.

Nikitin, N.V., Nicoud, F., Wasistho, B., Squires, K.D., Spalart, P.R. (2000), “An approach to wall modeling in large-eddy simulations”, Physics of Fluids, Vol. 12, pp. 1629-1632.

Patankar, S.V., Liu, C.H., Sparrow, E.M. (1977), “Fully developed flow and heat transfer in ducts having streamwise-periodic variations of cross-sectional area”, Journal of Heat Transfer, Vol. 99, pp. 180-186.

Patankar, S.V., Spalding, D.B. (1972), “A calculation procedure for heat, mass and momentum transfer in three-dimensional parabolic flows”, International Journal of Heat and Mass Transfer, Vol. 15, pp. 1787-1806.

Piomelli, U., Balaras, E., Pasinato, H., Squires, K.D., Spalart, P.R. (2003), “The inner-outer layer interface in large-eddy simulations with wall-layer models”, International Journal of Heat and Fluid Flow, Vol. 24, pp. 538-550.

Pope, S.B. (2000), “Turbulent flows”, Cambridge University Press.

Rhie, C.M., Chow, W.L. (1983), “Numerical study of the turbulent flow past an airfoil with trailing edge separation”, AIAA Journal, Vol. 21, pp. 1525-1532.

Robinson, S.K. (1991), “Coherent motions in the turbulent boundary layer”, Annual Review of Fluid Mechanics, Vol. 23, pp. 601-639.

Rodi, W. (1997), “Comparison of LES and RANS calculations of the flow around bluff bodies”, Journal of Wind Engineering and Industrial Aerodynamics, Vol. 69-71, pp. 55-75.

Sagaut, P. (2006), “Large eddy simulation for incompressible flows”, Springer-Verlag.

Santiago, J.L., Martilli, A., Martin, F. (2007), “CFD simulation of airflow over a regular array of cubes. Part I: Three-dimensional simulation of the flow and validation with wind-tunnel measurements”, Boundary-Layer Meteorology, Vol. 122, pp. 609-634.

Schluter, J.U., Pitsch, H., Moin, P. (2004), “Large eddy simulation inflow conditions for coupling with Reynolds-averaged flow solvers”, AIAA Journal, Vol. 42, pp. 478-484.

Schmidt, S., Thiele, F. (2002), “Comparison of numerical methods applied to the flow over wall-mounted cubes”, International Journal of Heat and Fluid Flow, Vol. 23, pp. 330-339.

Shi, R.F., Cui, G.X., Wang, Z.S., Xu, C.X., Zhang, Z.S. (2008), “Large eddy simulation of wind field and plume dispersion in building array”, Atmospheric Environment, Vol. 42, pp. 1083-1097.

Sini, J.-F., Anquetin, S., Mestayer, P.G. (1996), "Pollutant dispersion and thermal effects in urban street canyons", Atmospheric Environment, Vol. 30, pp. 2659-2677.

Smagorinsky, J. (1963), "General circulation experiments with the primitive equations", Monthly Weather Review, Vol. 91, pp. 99-165.

Spalart, P.R., Allmaras, S.R. (1994), "A one-equation turbulence model for aerodynamic flows", La Recherche Aerospatiale, Vol. 1, pp. 5-21.

Spalart, P.R., Jou, W.H., Strelets, M., Allmaras, S.R. (1997), "Comments on the feasibility of LES for wings and on a hybrid RANS/LES approach", Advances in DNS/LES, Greyden Press.

Speziale, C.G. (1998a), "Turbulent modeling for time-dependent RANS and VLES: a review", AIAA Journal, Vol. 36, pp. 173-184.

Speziale, C.G. (1998b), "A combined large-eddy simulation and time-dependent RANS capability for high-speed compressible flows", Journal of Scientific Computing, Vol. 13, pp. 253-274.

Squires, K.D., Forsythe, J.R., Morton, S.A., Strang, W.Z., Wurtzler, K.E., Tomaro, R.F., Grismer, M.J., Spalart, P.R. (2002), "Progress on detached-eddy simulation of massively separated flows", AIAA paper 2002-1021.

Strelets, M. (2001), "Detached-eddy simulation of massively separated flows", AIAA paper 2001-0879.

Temmerman, L., Hadziabdic, M., Leschziner, M.A., Hanjalic, K. (2005), "A hybrid two-layer URANS-LES approach for large-eddy simulation at high Reynolds numbers", International Journal of Heat and Fluid Flow, Vol. 26, pp. 173-190.

Townsend, A.A. (1980), "The structure of turbulent shear flows", Cambridge University Press.

Tucker, P.G., Davidson, L. (2004), "Zonal *k-l* based large-eddy simulations", Computers and Fluids, Vol. 33, pp. 267-287.

Versteeg, H.K., Malalasekera, W. (1995), “An introduction to computational fluid dynamics: the finite volume method”, Prentice Hall.

Walton, A., Cheng, A.Y.S. (2002), “Large-eddy simulation of pollution dispersion in an urban street canyon – Part II: idealised canyon simulation”, Atmospheric Environment, Vol. 36, pp. 3615-3627.

Xie, Z., Castro, I.P. (2006), “LES and RANS for turbulent flow over arrays of wall-mounted obstacles”, Flow, Turbulence and Combustion, Vol. 76, pp. 291-312.